THE UNIVERSITY *of* EDINBURGH

Classification of sea ice types for the East part of Greenland waters using SENTINEL 1 data

Ioannis Gkanatsios

Master of Science by Research

School of Geoscience

University of Edinburgh

September 2017

Statement of originality

I declare that this thesis has been composed solely by myself and that it has not been submitted, in whole or in part, in any previous application for a degree. Except where states otherwise by reference or acknowledgment, the work presented is entirely my own.

Acknowledgments

I want to thank my supervisors and Astrosat for the support.

Abstract

Ships navigate in Greenland waters all year round. Cruises to Greenland due to tourism and educational purposes have increased the last decade. Hence, it is essential for ships that navigate through Sea Ice in winter to use reliable and accurate information on sea ice conditions. An accurate classification of Sea Ice types is an ongoing problem. Many classification algorithms depend only on the SAR image intensity for discriminating the sea ice types. Different Sea Ice types exhibit similar backscatter signature which makes the algorithm unable to correctly classify them.

In this study, two dual-polarization SENTINEL-1 images with a spatial resolution of 40 x 40m acquired over the East part of Greenland in February and May of 2016. Support Vector Machine (SVM) classifier was used to perform the classification. In order to improve the discrimination of ice types, texture analysis was performed using Grey Level Co-occurrence Matrix (GLCM) algorithm. Ten GLCM texture features were calculated. The analysis revealed that the most informative texture features for the sea ice classification are Energy, mean, dissimilarity for HV polarization and Angular Second Moment, variance and energy for HH polarization.

The classification results for the SAR images acquired during winter and spring period were compared against the sea ice charts produced by DMI. A good agreement between the classification results and validation data is shown. The results show that the overall classification accuracy for both SAR images amount to 91%. The most hazardous for ships navigation sea ice types (old ice and deformed first year ice) have been successfully discriminated.

Table of Contents

List of figures

List of tables

1 Introduction

1.1 Overview

Sea ice monitoring in North regions (Greenland, Arctic, Baltic Sea, etc.) has been of interest for many years. Many groups, including scientists, explorers, oil and gas companies and tourists travel to the Polar Regions regularly for training, educational and leisure purposes. The growing interest of tourists and their desire for exotic destinations has led to a higher level of activity in remote areas. When planning a journey to remote places, navigational information as well as knowledge about the area of operation (ice formation and weather conditions) must be taken into consideration.

The major goal of sea ice information is to optimize and safeguard ship operations as well as to select the safest sailing routes and reduce the risk involved (Alexandrov et.al 2007). This implies the need for detailed sea ice data (ice thickness and sea ice types) specifically for small ships and fishing vessels on locations with the most hazardous sea ice phenomena (Alexandrov et.al 2007). In general, sea ice information is of importance for operational activities throughout the year, specifically in severe sea ice conditions (Alexandrov et.al 2007).

Navigation in Greenland waters differs significantly from navigation in other (non-Arctic) waters (International Marine Organization 2009). Sea ice conditions along the East coast are characterized by being more dynamic than in other parts of Greenland waters (DMI 2015). This happens due to the movement of big amount of Polar ice induced by currents of East Greenland. If an accident occurs at a remote area of Greenland Sea ice, assistance may possibly be far away, if available at all. In order to avoid accidents, detailed maps of sea ice conditions at the area of operation are needed.

Remote sensing is the primary tool for monitoring and retrieving information about the ice, especially, for regions located in remote locations. The extreme climate conditions

prevailing in those remote regions where sea ice exists, spaceborne remote sensing is the only tool that can be utilized for sea ice monitoring (Sinha and Shokr 2015).

Remote sensing by imaging radar systems on satellites is the most important method of observing sea ice on a regional scale independent of cloud cover and day light conditions (Alexandrov et.al 2007). Radar sensors are independent of solar radiation because they provide their own source of illumination in the form of electromagnetic waves which can penetrate though clouds and precipitation. This is particularly important for sea ice monitoring in the Polar Regions were cloud, fog and darkness significantly limit the use of visible data. The availability of SAR images has replaced the use of expensive helicopters for local ice reconnaissance to optimize the sailing route (Alexandrov et.al 2007).

For more than two decades, SAR has been the primary source of data for monitoring sea ice characteristics. In past years, sea ice centers were relied on data acquired from RADARSAT-1 or ENVISAT (ASAR) satellites (single polarization data operating at C-band) as they could deliver data in relatively high spatial resolution as well as covering a large area on the ground using wide swath mode. More recently, SENTINEL-1 SAR mission has been launched by European Space Agency (ESA) in 2014 delivering good quality SAR data.

1.2 Research problem and background

Many ships and vessels operate in the East part of Greenland waters (fishing vessels and cruise ships) throughout the year encountering problems in navigating though the ice.

The population of Greenland is heavily relied on fishing. Hence, fishing vessels operate in this region all year-round in severe weather conditions. Due to their small sizes, they encounter serious problems navigating though the ice covered waters.

On the other hand, cruises to Greenland have increased and gained popularity the last decade due to its wild life and scenery. Due to the fact that cruise ships are not specifically

designed for navigating in sea ice, extra care must be taken in order to avoid the hazardous areas.

Expeditions for educational purposes in this region of Greenland waters have also been increased. Students from different places around the world that show an interest in science are taken to places where they are introduced to elementary sea ice experiments by teachers. Greenland has always been popular destination for scientific purposes.

A detailed navigational ice chart is necessary for ships and vessels to avoid getting trapped in the ice. The greatest danger for ships traversing in the ice is to get trapped in a highly deformed sea ice where they lose the propulsion or maneuverability.

Organizations such as Ocean & Sea Ice Satellite Application Facility (OSI SAF), Danish Meteorological Institute (DMI) and Polar View (PV) constantly monitor the Greenland waters producing sea ice charts regularly. The sea ice charts produced by these organizations are of low resolution. Sea ice products of coarse resolution fail to discriminate all the different sea ice types over an area and this can be problematic for ships navigation.

OSI SAF provides sea ice products (sea ice concentration, sea ice edge and sea ice types) globally with a resolution of 10 Km. The sea ice products of OSI SAF are based on the Special Sensor Microwave Imager (SSM/I) as well as ASCAT instrument which is a C-band scatterometer with a resolution of 12.5 Km. Such low resolution products cannot be used by ships for safe navigation because they fail to detect potential hazardous areas.

DMI is focused on ocean currents, ocean waves and sea ice observations. The sea ice charts of Greenland waters produced by DMI (medium and high resolution sea ice charts) is for navigational purposes. Sea ice charts are manually produced by sea ice experts based on satellite data (SAR and IR/optical). These ice charts lack detailed information of sea ice types. The DMI sea ice charts mainly display the three major sea ice types that are present in the area.

1.3 Aim and objectives

The principal goal of this study is to develop an improved and detailed sea ice classification map for safer ship navigation using SENTINEL-1 dual polarization data.

For the achievement of this goal, the following objectives have been set:

- SENTINEL -1 SAR images acquisition over the area of interest.
- SAR images pre-processing. This step involves, applying precise orbit file to the datasets, thermal noise removal, radiometric calibration, incidence angle normalization and speckle noise removal.
- Texture analysis. In texture analysis, texture measures for sea ice are extracted which give us valuable information about the texture of each sea ice type.
- Classification of sea ice types using support vector machine classifier and texture analysis
- Validation of the results using sea ice charts from Danish Meteorological Institute (DMI)

2 Background and literature review on sea ice monitoring for marine navigation

2.1 History of remote sensing in monitoring the East part of Greenland waters

In this chapter, brief history of sea ice monitoring in Greenland waters is given with an emphasis on sea ice discrimination for marine navigation.

The interest of sea ice monitoring in Greenland waters started back in 1984. The Technical University of Denmark (TUD) carried out a research on microwave signatures of sea ice types for the East part of Greenland waters using a multi-frequency airborne microwave radiometer (5, 17, 35 GHz) which has been flown over the area. This instrument could discriminate well between sea ice and open water but data had to be integrated over large footprints (Sinha and Shokr 2015). Due to its large footprint (47 x 73m at 34GHz and 94 x 146m at 17GHz) it was impossible for the radiometer to discriminate the different sea ice types that were present in Greenland waters. In areas where Multi-year ice was present, the instrument was not able to establish a clear signature, as the multi-year ice floes consist of broken and re-frozen smaller floes of different age, including also first year ice (Pedersen, T.L and Skou, N 1984). This instrument was able only to establish clear signatures between water and first year ice or between multi-year ice and water. As Pedersen and Skou (1984) concluded after conducting this experiment, the data collected by the microwave radiometer were not very useful for sea ice classification but it could be used for sea ice concentration.

After the pioneer work of Drinkwater and Carsey (1991) that demonstrated the capability of space-borne SEASAT radar scatterometer to detect sea ice, it has been shown that space-borne scatterometers can be employed for sea ice detection. The mission of SEASAT ended three months later due to power failure. Despite the fact that this instrument was primarily for ocean wave imaging, images of Arctic were also acquired. The 25m fine resolution imagery data from SEASAT were used to produce the first

detailed sea ice motion maps (Sinha and Shokr 2015). The drawback of SEASAT was that it operated in a single channel (vertical polarization) and the discrimination of different ice types was difficult due to the overlapping of backscatter signatures from the ice surface

A research carried out by Ezraty (2002) demonstrated how the QuickSCAT satellite carrying the SeaWinds scatterometer can be utilized in detecting new ice in in East Greenland Sea. SeaWinds is a two-beam scatterometer operating at Ku band (13 GHz) with a footprint size of 37 Km x 25 Km (Ezraty, R 2002). The inner beam is HH (horizontally transmitted and horizontally received) and the outer beam is VV (vertically transmitted and vertically received). For the sea ice discrimination, polarization ratio, mean, and normalized standard deviation have been used. Sea ice areas were clearly identified on the map of mean backscatter (Ezraty 2002). The difficulty was to set quantitative criteria for the discrimination of the low backscatter values of forming new ice which are in the range of open water backscatter for any wind speed (Ezraty 2002). SeaWinds instrument proved capable of detecting new sea ice using polarimetric ratio. Combining scatteromer and radiometer polarization rations, it helps on locating new sea ice within a grid size of 25 Km x 25 Km (Ezraty 2002).

Since 1980, the sea ice observation of Greenland waters has been carried out using scatterometers. Scatterometers proved useful tools in identifying the sea ice covered the East part of Greenland but it could not provide detailed maps of sea ice types due to its low resolution. The Danish Meteorological Institute (DMI) was established in 1872 and provides meteorological services of the realm of Denmark, Faroe Islands, Greenland and surrounding waters (DMI 2015). It produces weather, wind and sea ice maps.). At that time, many studies have been carried out by DMI around Grrenland waters using scatterometer and radiometer instruments (Tonboe and Ezraty 2002; Toudal and Tondoe 2005). With the advance of remote sensing instruments, DMI is now heavily relied on SAR data for sea ice monitoring due to its high resolution which allows very detailed ice maps. DMI contributes to sea ice monitoring of Greenland waters providing medium resolution navigational sea ice charts using SAR imageries for safer navigation.

The most recent SAR platform for sea ice monitoring is SENTINEL-1. It is a polar, sun-synchronous orbiting SAR satellite with a revisit frequency higher than 1 day at high latitudes. The SENTINEL 1 SAR platform can operate in dual polarization (HH + HV or VV+ VH) where sea ice observation can be improved. The first sea ice study was carried out by DMI in 2014 and the satellite demonstrated the capability of delivering SAR data (a few weeks after its launch) at a quality sufficiently for operational ice charting (Pederson et.al 2015). Now, SENTINEL 1 data is the primary source for sea ice observation by DMI and other organizations such as Norwegian Ice services.

In 2003, Polar View, an Earth Observation (EO) programme started which has been focused on both Arctic and Antarctica providing services to users for improved environmental and security related monitoring (Cheek 2009). Polar View provides high resolution ice charts for the Barents Sea on a weekly basis with a focus on Svalbard area and are used primarily for marine safety and environmental research (C-Core 2010). These ice charts provide information about ice edge and ice concentration. Regional ice charts for Greenland Sea of medium resolution are produced based on SAR data. These charts contain information about sea ice parameters such as ice edge, ice concentration, ice thickness and icebergs (C-Core 2010).

2.2 Sea ice types in the East Greenland

The sea ice along the East part of Greenland can be grouped into three zones:

1. Land-fast ice. Land-fast ice forms along the coastline and stays in place during winter time. Normally it breaks up and drifts away or melts in spring, but under exceptional circumstances it may stay in place the whole summer and survive the next year (DMI 2000).
2. Pack ice. The drifting pack ice in the East Greenland is composed of ice floes (thickness of each floe varies) originating from various places in the Arctic region (DMI 2000).

3. Marginal Ice Zone (MIZ). The MIZ is a region that forms at the boundary of the open and frozen oceans (Wikiwaves 2010). MIZ may consists of large or small ice floes drifting over a large area and is affected by weather conditions (wind, currents). The process that produces the MIZ is when the open sea interacts with the sea ice.

Multi-year ice (between 2.5 and 4m thick) originating from the Arctic Ocean is being transported through the Fram Strait (between Greenland and Svalbard) into the Greenland sea and it drifts along the East coast of Greenland (Torben and Carsten 2003). The sea ice exported to East Greenland through Fram Strait consists in general of multi-year ice with a little contribution from glaciers and sea ice that is formed locally.

Therefore, the formation of Polar Ice in the Arctic Ocean plays a crucial role for the net balance of the sea ice concentration in the Greenland Sea (Hinkler 2005). The largest part of the Arctic is covered by ice during the year, and the two circulation systems responsible for the ice flux towards Greenland are the transpolar drift and Beaufort Gyre (ocean current driven by wind located in the Arctic) as shown in figure 2.0

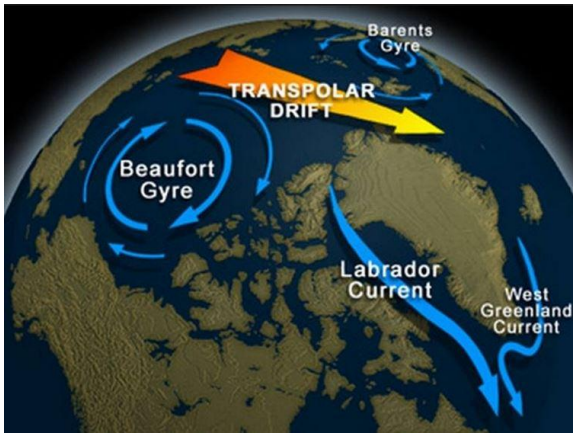

Figure 2.0: Circulation systems that transport the sea ice to Greenland. The blue arrows show a clockwise circulation of Beaufort Gyre due to winds. The long yellow arrow illustrates the sea ice transporting to Greenland waters (source: https://www.google.co.uk/search?q=beaufort+gyre&sa=X&biw=1366&bih=606&tbm=isch&tbo=u&source=univ&ved=0ahUKEwjo-ILb0ejLAhVDthQKHVtIA5gQsAQIKw#imgrc=1LOVp8lPDHOFKM%3A)

As the ice drifts in the gyre, it follows a clockwise circulation forced by the surface winds and ocean currents around the Beaufort high and then it continues towards the Fram Strait (Hinkler 2005). The ice volume flux transferred to East Greenland is estimated to 2846 Km^3 yr^{-1} on average, but varying between 2046 and 4687 Km^3 (Torben and Hansen 2003). Due to the inflow through the Fram Strait, sea ice distribution and formation in the Greenland Sea is much more complex and dynamic in nature than for instance the ice formed in West Greenland (Hinkler 2005).

3 Principles of Radar and Synthetic Aperture Radar

3.1 Introduction

Active microwave systems are instruments that transmit microwave signals from their antennas. This outgoing packet of energy eventually interacts with the landscape and some of it is backscattered to return towards the antenna (Lusch 1999). The components of an imaging radar system include a transmitter, a receiver, an antenna array and a recorder (Campbell and Wynne 2011). A transmitter is designed to transmit repetitive pulses of microwave energy at a given frequency (Campbell and Wynne 2011). A receiver accepts the reflected signal as received by the antenna, then filters and amplifies it as required (Campbell and Wynne 2011). An antenna array transmits a narrow beam of microwave energy (Campbell and Wynne 2011). Such an array is composed of waveguides, devices that control the propagation of an electromagnetic wave such that waves follow a path defined by the physical structure of the guide (Campbell and Wynne 2011). Finally, a recorder records and displays the signal as an image (Campbell and Wynne 2011).

Active systems do not rely on external radiation sources such as solar radiation, thus, the presence of sun is not relevant to the imaging process, although it may affects the target scattering characteristics (Curlander and McDonough 1991). Furthermore, the radar frequency can be selected such that its absorption by atmospheric molecules (oxygen or water vapors) is small (Curlander and McDonough 1991). The figure 3.0 shows the absorption bands.

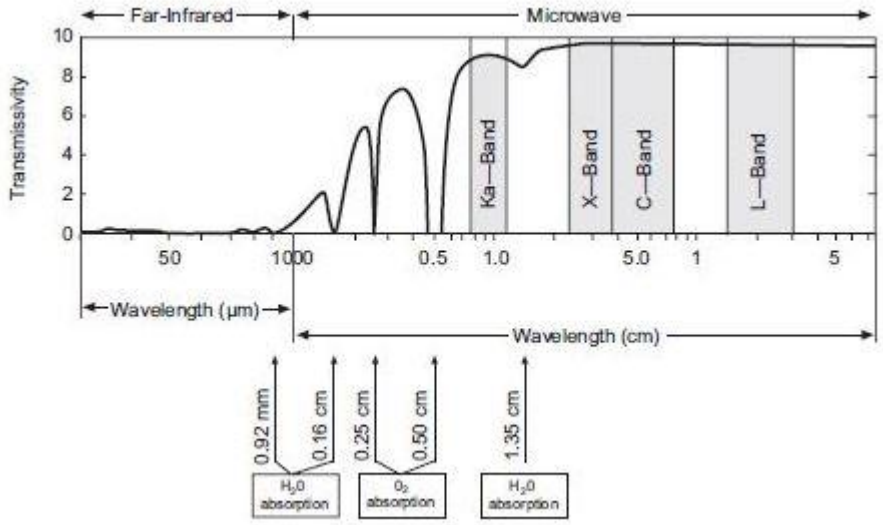

Figure 3.0: Diagram of the electromagnetic radiation absorption (Curlander and McDonough 1991)

As we can see, for the frequencies between 1-10 GHz (3-30 cm) the transmissivity is very high (approaches 100%). Thus, independent of the cloud cover or precipitation, a radar sensor operating in this frequency range is always able to image the earth's surface (Curlander and McDonough 1991). As the radar frequency is increased within the microwave spectrum, the transmission attenuation increases (Curlander and McDonough 1991).

The selection of the radar wavelength, however, is not simply governed by resolution and atmospheric absorption properties (Curlander and McDonough 1991). The interaction mechanism between electromagnetic (EM) wave and the surface is highly wavelength dependent (Curlander and McDonough 1991). The EM wave interacts with the surface by a variety of mechanisms which are related to both surface composition and its structure (Curlander and McDonough 1991).

3.2 Radar image resolution

As a radar illuminates an area by transmitting pulses of microwave energy, it precisely measures the time difference between the transmitted pulse and the receipt of the reflected energy and it is able to determine the distance of the reflected object (called slant range) (Jackson and McCandless 2004). The range resolution of a radar system is its ability to distinguish two objects separated by some minimum distance (Jackson and McCandless 2004).

Spatial resolution in the range direction is a function of the processed pulse-width (τ) multiplied by the speed of light (c) and divided by two (Jackson and McCandless 2004).

$$\text{Range Resolution} = \frac{c\tau}{2} = \frac{c}{2\beta} \tag{3}$$

Where β is the pulse bandwidth

In slant range terms, range resolution is constant and solely dependent on pulse duration (Lusch 1999). The shorter the pulse duration, the narrower the transmitted energy packet and the better the slant range resolution. Figures 3.1 and 3.2 depicts the pulse duration and range resolution respectively.

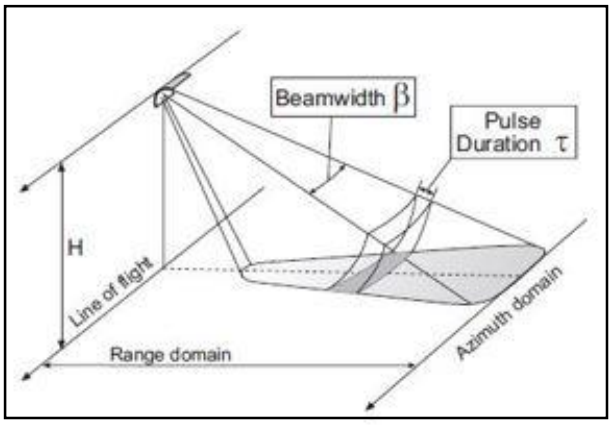

Figure 3.1: Diagram of pulse duration (Lusch 1999)

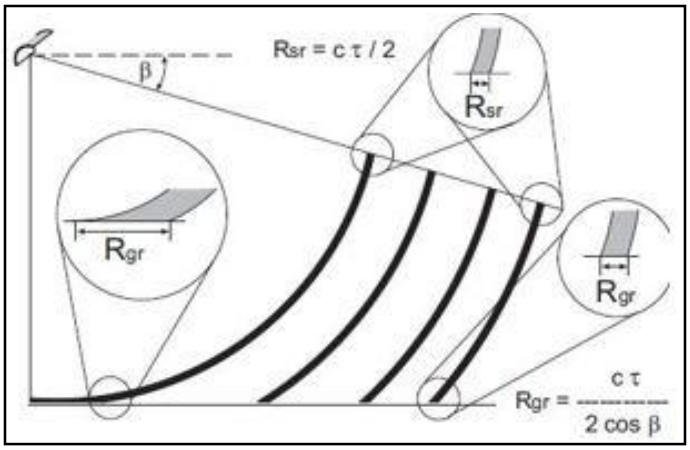

Figure 3.2: Diagram of range resolution (Lusch 1999)

Azimuth resolution refers to the ability of a radar to discriminate different targets in the azimuth direction (direction of the satellite's flight) and is defined by the beam width (β) (figure 3.3). The azimuth resolution is higher in the near range and it becomes coarser as the distance from sensor increases.

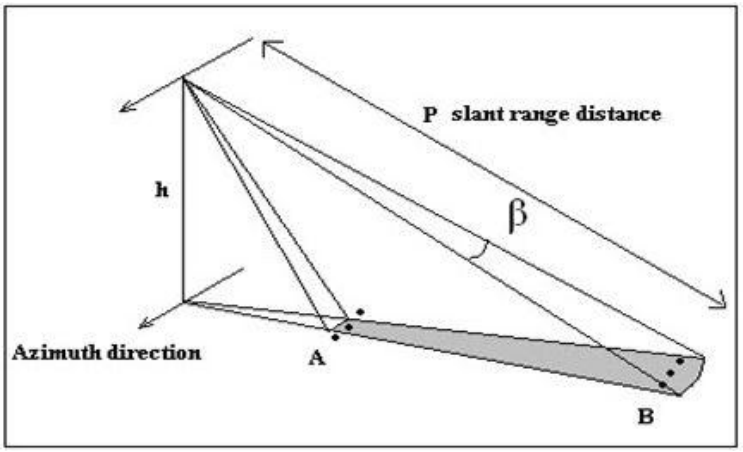

Figure 3.3: Azimuth resolution in RAR (Source: http://ecoursesonline.iasri.res.in/mod/page/view.php?id=2068)

In figure 3.3, the three objects at near range are located outside the beam (the distance between the objects itself is greater than the size of the beam), the return signal of those targets will be received separately, hence, these targets are resolved. At the far end, the three objects will not be able to be resolved because they are all located inside the beam.

The azimuth resolution is defined as:

$$R_a = \frac{H*\lambda}{L*cos\theta} \tag{3.1}$$

Where:

H = Height of the platform

L = Length of the antenna

λ = Wavelength of the pulse

θ = Incidence angle

The above equation shows that, as the altitude of the platform increases, the azimuth resolution decreases. In order to achieve a better azimuth resolution, a very long antenna (L) is required. By increasing the physical length of the antenna is impractical. Hence, the resolution can be increased by increasing the antenna length virtually, which is known as Synthetic Aperture Radar (SAR) (e-krishi Shiksa 2014).

The synthesis term refers to a method of processing the returned echoes to improve the azimuthal resolution by utilizing the Doppler beam sharpening approach allowing spatial resolution of the imaged scene (Woodhouse 2006). The SAR system saves the phase histories of the responses at each position as the real beam moves through the scene and then weights, phase shifts, and sums them to focus on one point target (resolution element) at a time and suppress all others (Jackson and McCandless 2004). SAR achieves a very

high signal processing gain because of coherent (in-phase) summation of the range-correlated responses of the radar (Jackson and McCandless 2004). All of the signal returns that occur as the real beam moves through each target can be coherently summed as shown in the figure 3.4 (Jackson and McCandless 2004).

A Doppler shift (f_D) imposed on the backscatter from each target and is determined by the motion along the line of sight (LoS) between the SAR antenna and the target (figure 3.5) (Lusch 1999). As the platform is constantly moving, the echoes returning from objects in the front part of the beam are Doppler shifted to higher frequencies, while echoes from the aft part of the beam are shifted to lower frequencies (Woodhouse 2006). During the time that any target is illuminated in the fore beam zone, its backscatter is upshifted (f_{D+}) because the range between the antenna and the target is diminishing (Lusch 1999). After passing the zero Doppler shift line, the range between the antenna and the target is constantly increasing and its backscatter signal is downshifted (f_D -) in frequency (Lusch 1999).

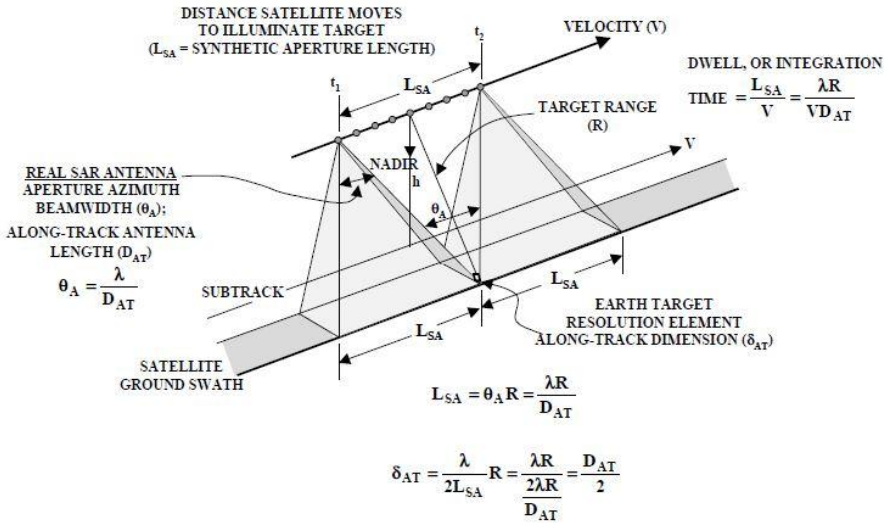

Figure 3.4: Synthetic Aperture Radar. As the platforms moves along, the target located inside the beam is constantly illuminated improving the azimuth resolution. (Jackson and McCandless 2004)

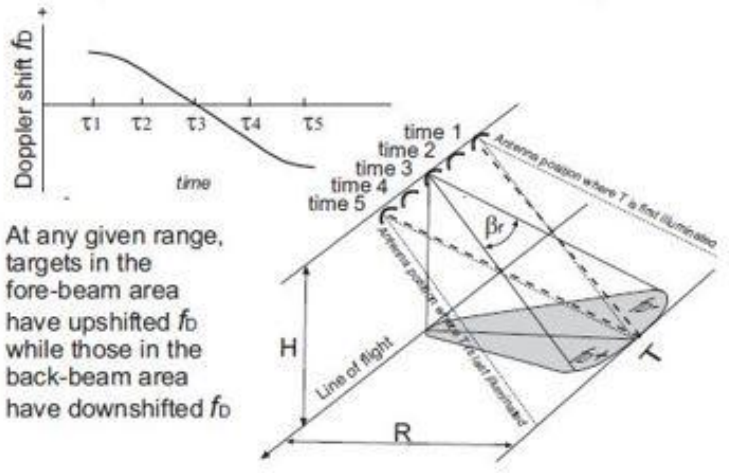

Figure 3.5: Doppler shift effect (Jackson and McCandless 2004)

3.3 The radar equation

The radar transmitter (figure 3.6) generates a brief (microseconds) high power burst of radio frequency electromagnetic energy and this is conveyed to an antenna through appropriate microwave 'plumbing' (Curlander and McDonough 1991). Once the pulse has been transmitted, the transmitter turns off until the receiver receives the pulse returned from the earth's surface. Any perceived echo has its time of reception noted, relative to the time of transmission of the pulse (Curlander and McDonough 1991). The time delay τ is interpreted in terms of range to target, $R = c\tau/2$, providing another spatial dimension for localization (Curlander and McDonough 1991).

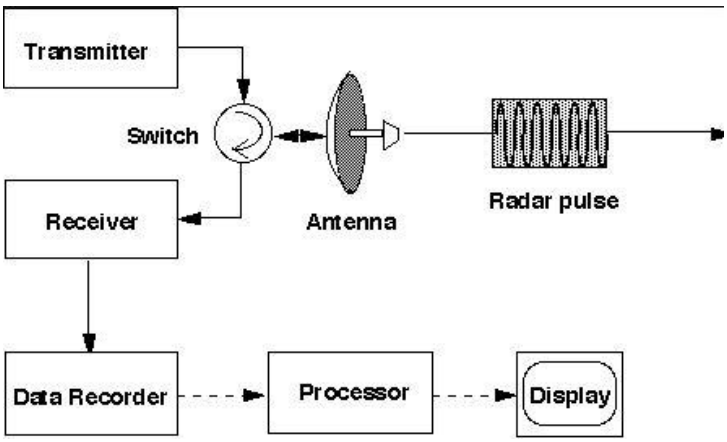

Figure 3.6: Radar system (Curlander and McDonough 1991)

The power of the signal returned to the antenna after interacting with the surface of the earth is given by the radar equation:

$$P_r = \frac{\sigma^{G^2} P_t \lambda^2}{(4\pi)^3 R^2} \tag{3.2}$$

Where:

$\boldsymbol{P_r}$ is the power of the received signal returned to the antenna from the Earth's surface.

R is the range between the target and the antenna

$\boldsymbol{P_t}$ is the transmitted power

λ is the wavelength

G is the antenna gain (the ability of the antenna to focus outgoing energy into the beam)

σ is the backscatter coefficient

All of these variables are determined by the design of the radar system and are known quantities apart from variable σ (Curlander and McDonough 1991). The variable σ is controlled by specific characteristics of the surface of the earth. The value of σ conveys information concerning the amount of energy scattered from a specific region on the landscape as measured by σ^o, the radar cross section. The backscattering coefficient (σ^o) expresses the observed scattering from a surface area as a dimensionless ratio between two real surfaces; it measures the average radar cross section per unit area (Curlander and McDonough 1991).

3.4 Geometry of imaging radar

The geometry of an imaging radar is illustrated in figure 3.6. The radar antenna is oriented parallel to the flight direction; it is looking sideward to the ground (Wang 2008). The radar is moving along the flight path above the earth with height H, at velocity V and the radar antenna which is assumed to be a phased array, has dimensions of length L and width W (Wang 2008). The ground surface area from which the radar pulse is reflected is called footprint and swath is the ground surface area covered by the consecutive radar pulses (Wang 2008). The radar transmits short pulses with duration $T_p$and repeats at period PRI = 1 / $f_{PRF}$to the ground, where f_{PRF} is the pulse repetition frequency (Wang 2008). The 3-dB beam-width along the track is θ_H=λ/L, while across the track it is θ_v=λ/W and the wavelength of the transmitted signal is λ (Wang 2008). The pulse is directed at some angle off nadir called the look angle or incident angle (Wang 2008).

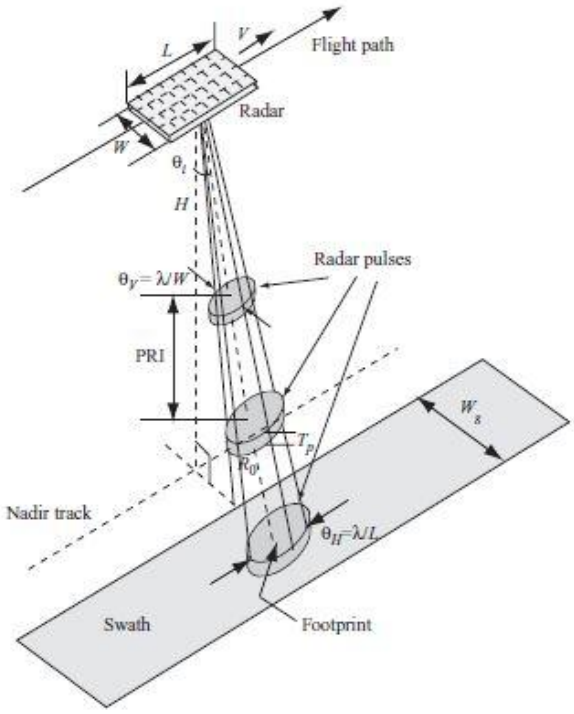

Figure 3.7: Geometry of an imaging radar (Wang 2008)

3.4.1 Geometric distortions of the radar image

Because the radar measures the distance to features in slant range rather than the true horizontal distance along the ground, radar images inherently contain geometric distortions (Wang 2008). Some of the geometric distortions are, layover, foreshortening and shadow.

3.4.1.1 Layover

Layover occurs when the radar signal reaches the top of an object before it reaches the base (figure 3.7). The return signal from the top of the feature will be received before the signal from the bottom will (Wang 2008). As a result, the top of the feature is displayed towards the radar from its true position on the ground, and 'lays over' the base of the feature (B' to A') (Wang 2008).

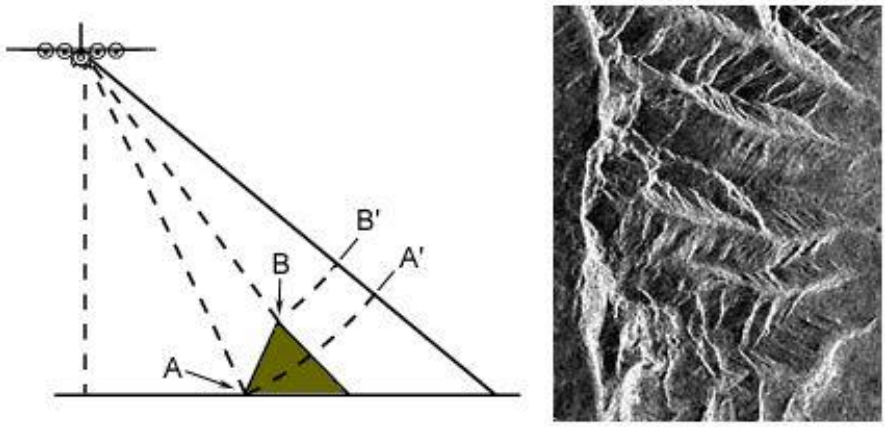

Figure 3.8: Radar layover in a mountainous terrain. The point B is closer to the radar antenna than is point A, so it is shown closer on the image (Source: http://hosting.soonet.ca/eliris/remotesensing/bl130lec13.html)

3.4.1.2 Foreshortening

Foreshortening occurs when the radar beam reaches the base of a feature before it reaches the top (Wang 2008). As the radar measures distance in slant-range, the slope A-B of the figure 3.8 appears as compressed in the image and the slope C-D is severely compressed.

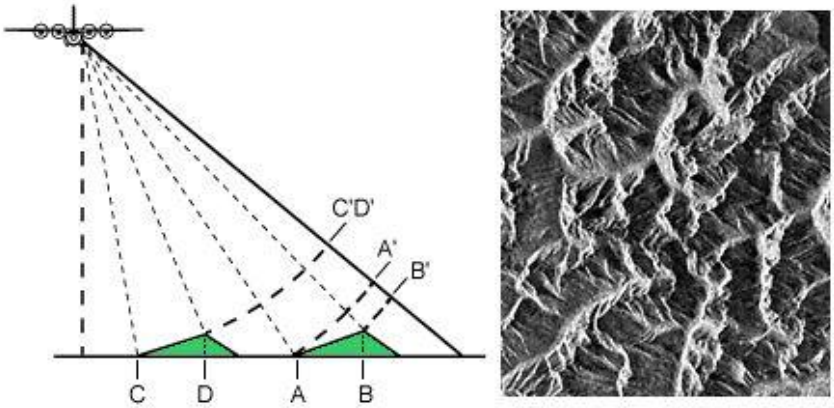

Figure 3.9: Image foreshortening. The projection of A', B' into the slant-range domain distorts the representation of the slope A, B (Source: http://hosting.soonet.ca/eliris/remotesensing/bl130lec13.html)

3.4.1.3 Shadowing

The shadowing effect occurs when the radar beam cannot reach part of a tall feature as illustrated in figure 3.9 (Wang 2008). Shadow in a radar image usually occurs due to small depression angles

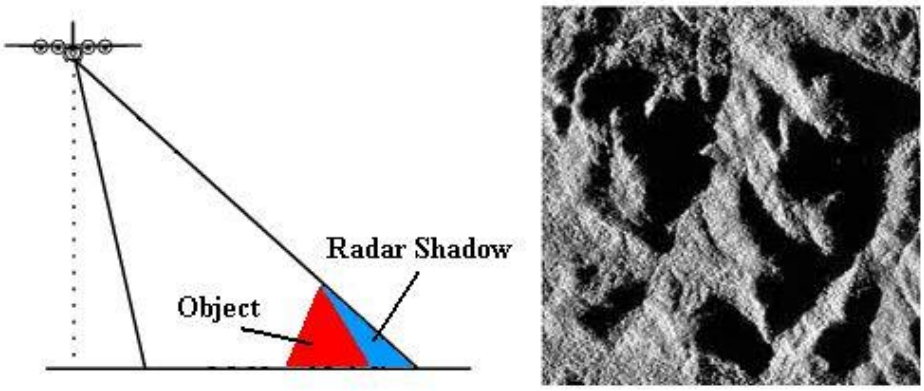

Figure 3.10: Shadow effect. The blue area of the image on the left represents the shadow as the beam cannot reach this part of the feature (Source: http://hosting.soonet.ca/eliris/remotesensing/bl130lec13.html)

3.5 Backscatter

Radar backscatter is the amount of energy returned to the sensor after interacting with the surface of the earth and it is determined using the quantity called backscattered coefficient (σ^o) where the σ^o values are expressed in decibel scale. The radar signal that interact with a surface will be reflected back to sensor in a manner that depends on the radar wave properties, look angle of the sensor and the characteristics of the surface (rough or smooth surface). The incidence angle (θ) is defined as the angle between the axis of the incident radar signal and a perpendicular to the surface that the signal strikes (figure 3.10) (Campbell and Wynne 2011).

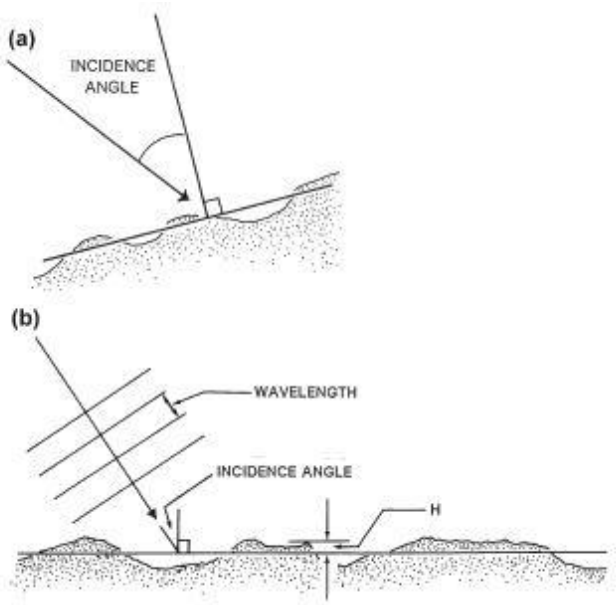

Figure 3.11: Incidence angle is shown in (a), surface roughness in (b) (Campbell and Wynne 2011)

If the surface is homogeneous with respect to its electrical properties and smooth with respect to the wavelength of the signal, then the reflected signal will be reflected at an angle equal to the incidence angle, with the most of the energy directed in a single direction (specular reflection) (Campbell and Wynne 2011). For rough surfaces, the signal will be scattered in all directions (diffuse reflection), and it will not depend only on the incidence angle. One definition that defines a rough surface as one in which the surface height (h) is greater than the wavelength (λ) of the radar signal divided by 4.4 (constant value) and the sine of grazing angle (γ). While, a surface can be characterizes as smooth when, surface height (h) is less than the wavelength (λ) of the radar signal divided by 25 (constant value) and the sine of grazing angle (γ) as shown in the equations 3.3 and 3.4 respectively.

$$h > \frac{\lambda}{25\ sin\gamma} \tag{3.3}$$

$$h < \frac{\lambda}{4.4 \sin \gamma} \quad (3.4)$$

Where:

h is the height of the surface

λ is the wavelength of the radar signal

γ is the grazing angle between terrain and incidence vector

As the roughness of the surface depends not only on its physical characteristics but also on the wavelength (the radar wavelength varies between different sensors) of the signal and the incidence angle (table 3).

Roughness category	K-band (λ=0.86cm)	X-band (λ=3cm)	L-band (λ=25cm)
Smooth	h < 0.05cm	h < 0.17cm	h < 1.41cm
Intermediate	h = 0.05-0.28cm	h = 0.17-0.96cm	h = 1.14-8.04cm

Table 3: Surface roughness defined for different wavelengths (Campbell and Wynne 2011)

3.6 Polarization

Polarization is an important property when discussing the propagation and scattering of microwave energy, and is a key determinant of both microwave backscatter and emission (Lubin and Masson 2006). Polarization describes the locus of the electrical field vector in the plane perpendicular to the direction of propagation (Lubin and Masson 2006). If the vector is aligned to a certain plane according to a predictable alignment while the EM wave is propagating, the wave is called polarized (Sinha and Shokr 2015). If, on the other

hand, the wave has a random time-varying electric vector, it is called un-polarized (Sinha and Shokr 2015).

3.6.1 Polarization in radar systems

Imaging radars can be configured to transmit EM waves either in vertical or horizontal polarization and to receive the energy scattered by the surface either in horizontal or vertical polarization. However, some radars are designed to transmit horizontally polarized signals but to separately receive the horizontally and vertically polarized reflections from the landscape (Campbell and Wynne 2011). Those radar systems produce two images for the same Earth's surface that has been imaged. One image is produced by transmitting horizontally polarized wave and receiving a horizontally polarized wave. This is referred to as like-polarization (HH image). A second image is formed by transmitting horizontally polarized wave and receiving a vertically polarized wave. This is referred to as cross-polarization (HV image).

By comparing the HH and HV images, Features on the ground that depolarize the microwaves can be identified. The terms depolarizations refers to the situation when the dominant polarization of the scattered signal is different than the polarization of the transmitted signal (Sinha and Shokr 2015). Areas that tend to depolarize the signal are identified as bright regions on the HV image due to the effect of the depolarization. On the other hand, the same areas will appear as dark regions in the HH image. Depolarization of the radar signal that is scattered from the surface of the Earth depends on the surface structure. Depolarization of a radar signal is caused by multi-scattering process (Sinha and Shokr 2015). For sea ice, multiple scattering can be caused by an ice blocks of ridge or when the microwave interacts with old ice (due to the volume scattering).

4 Physical and microwave remote sensing properties of sea ice

4.1 Physical properties of sea ice

Understanding the physical process and properties of sea ice is important in order to interpret microwave signatures. The ice temperature is the main physical property that affects the sea ice characteristics. For example, floating sea ice sheets are found to be more flexible or elastic than freshwater ice covers because of the finer structure of the sub-grains (Sinha and Shokr 2015). The sea ice physical properties are strongly depend on the characteristics of the sub-grains. Physical properties of sea ice are different for different ice types (Sinha and Shokr 2015). Table 4.0 shows the most important equations for determining the sea ice parameters and in the table 4.1 approximate values of properties of sea ice types are summarized.

The incorporation of salt in the form of brine inclusions in the ice makes sea ice a vastly different material than freshwater ice (Drinwater et.al 1992). Brine drainage begins immediately after ice formation, occurring slowly during the growth season but increasing considerably during summer (Drinwater et.al 1992). Enhanced surface melting, coupled with increased interconnectivity of the brine inclusions, almost completely flushes the salt from the ice in the upper layers, leaving air voids and channels; a process that greatly increases the ice's porosity (Drinwater et.al 1992).

Density (Kg/m^2)	ρ_{si} = 917.8 – 0.14T
Salinity(‰) versus ice thickness(m)	S_{si} = 14.24 – 19.39h_i , h_i <= 0.4m S_{si} = 7.88 – 1.59h_i , h_i > 0.4m
Porosity (%)	p = S_{si} (0.05322 – 4.919/T)
Specific heat (Kj/Kg*K)	C_{si} = 2.11 + 17.2 (S_{si}/T^2)
Thermal conductivity	$K_{si} = \frac{\rho_{si}}{\rho_{pi}}$ (2.11 - 0.011T + 0.09 $\frac{S_{si}}{T_{si}}$ - $\frac{\rho_{si}-\rho_{pi}}{1000}$)
Latent heat of fusion (Kj/Kg)	$L_{si} = L_{pi}$ – 2.117 – 0.1145 + 18.1(S_{si}/T_{si})
Effective heat capacity (J/K*Kg)	hc_{si} = 2113 + 0.00172 ($S_{si}/T_{si}^2 T^2$)
Enthalpy of sea ice (KJ/Kg)	e_{si} = -332.4 + 2.12T_{si} + 0.008T_{si}^2
Melting temperature of sea ice	T_m = μS_{si} where μ=0.054
Energy needed to melt a unit volume of ice	q = ρ_s L_s (1 + $\frac{0.054\,S_{si}}{T_{si}^2}$) – ρ_{si} C_{pi}(0.054S_{si} + T_{si}^2)

Table 4.0: Equations to determine the sea ice parameters (Sinha and Shokr 2015)

	New Ice	**Young Ice**	**First-Year Ice**	**Multi-Year Ice**
Thickness (m)	<0.1	0.1 – 0.3	>0.3	>2.0
Bulk salinity (‰)	14	9	4	0.5
Density (Kg/m^2)	920	900	900	750 - 910
Dielectric constant (10GHz)	5.65-j 2.25	4.0-j 0.81	3.32-j 0.23	2.77-j 0.03
Therm conductivity (W/m*K)	2.14	2.14	2.09	1.88
Brine volume fraction	0.20	0.08	0.05	0.0

Table 4.1: Physical and electrical properties of sea ice types (Sinha and Shokr 2015)

4.2 Sea ice formation and growth

Ice grows mostly thermodynamically due to the colder temperature of the atmosphere with respect to the temperature of the sea water (Sinha and Shokr 2015). The rate of the thermodynamic growth of sea ice depends mainly on three factors that can be measured: air temperature, ice thickness and snow cover (Sinha and Shokr 2015). Other factors include the solar radiation, wind conditions and the density and albedo of snow (Sinha and Shokr 2015). One of the most important process that occur during sea ice growth is the brine rejection to the underlying sea water and the brine entrapment within the ice mass (Sinha and Shokr 2015).

Sea ice is broadly similar to freshwater ice in its physical characterization, though some significant differences are introduced by the presence and by the dynamic environment in which it exists (Rees 2006). The first major difference between sea ice and fresh water ice is that the freezing point for the sea ice is around -1.8 ^{o}C for a typical salinity of 34 part per thousand (Rees 2006). For salinities above 25 parts per thousand, the temperature at which sea water attains its maximum density is actually less than the freezing point (Rees 2006). As a consequence, the continued removal of heat from the water results in an unstable distribution of density, leading to convective[1] overturning until the whole water column has reached the freezing point (Rees 2006). Figure 4.0, depicts schematically the sea ice evolution from thin ice up to first year ice.

The development of sea ice can be divided in several categories such as: new ice, nilas, young ice, first year ice, second year ice and multi-year ice. Each of these types can be further sub-divided into more sea ice types. Increase in the ice thickness and changes in its structural and salinity properties and surface roughness during its growth causes changes in its backscatter coefficient (Alexandrov et al 2007). Sea ice types can be identified in SAR images based on their different backscatter statistics.

The main stages of sea ice formation are described below:

[1] Convection is the transfer of internal energy into or out of an object by the physical movement of a surrounding fluid that transfers the internal energy along with its mass

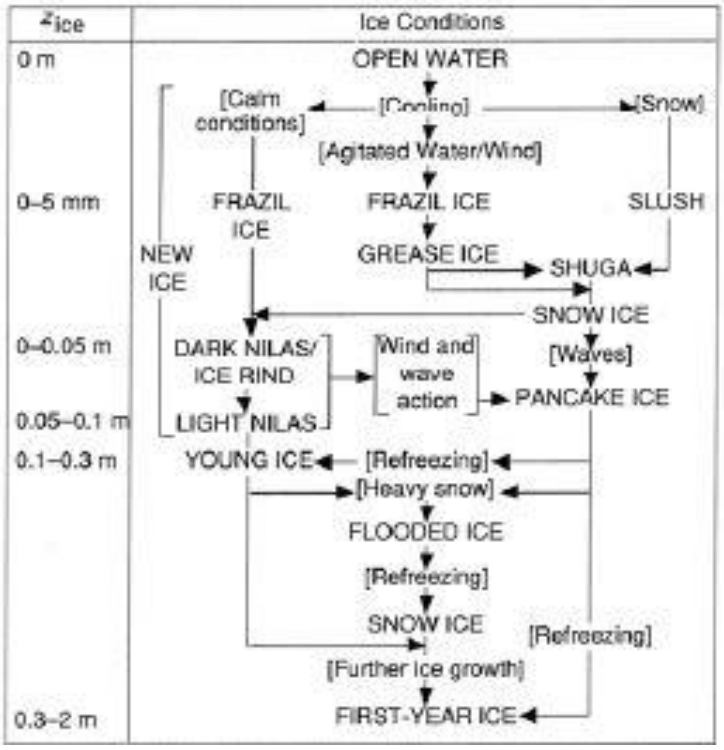

Figure 4.0: A schematic of the sea ice formation. The capital letters depict the ice types, while the brackets contain the related environmental process (Lubin and Masson 2006)

4.2.1 New ice

Sea ice recently formed on the water surface includes frazil ice, grease ice, slush and shuga (Alexandrov et al 2007). Under calm atmospheric and oceanic conditions, frazil ice is formed (Sinha and Shokr 2015). Frazil ice is formed as small, elongated crystals in the form of plates where it continues to grow (during the freezing period) until they touch each other and cover the whole surface of the water (Alexandrov et al 2007). It does not change the backscatter coefficient (σ^o) of the water surface, and therefore cannot be detected in SAR images (Alexandrov et al 2007). In the absence of waves, the number of crystals rapidly increase forming a continuous layer called grease ice which is characterized by its low reflecteivity and cannot be distinguished from calm open water in SAR image (Alexandrov et al 2007). Grease ice inhibits the formation of capillary

waves (Figure 4.1) and can be detected by its dark signature, often among bright areas of pancake ice (Alexandrov et al 2007).

Figure 4.1: New Ice formation near Arctic (source: https://www.asf.alaska.edu/sea-ice/)

4.2.2 Nilas

Nilas, which is formed from grease ice and represents an elastic ice crust bending under wave and swell action, is subdivided into dark and light nilas with thickness of less that 5cm and 5-10cm respectively (Alexandrov et al 2007). Nilas are usually broken into large pieces (a few meters to tens of meters wide) due to wind effect or oceanic conditions (Sinha and Shokr 2015). While floating and moving, the fractured pieces may slide over each other to form what is known a surface rafting (Sinha and Shokr 2015). Due to the near specular reflection of Electromagnetic (EM) waves from its surface, nilas has a low backscatter coefficient in the range from -24 to 28 dB for the C-band (Alexandrov et al 2007).

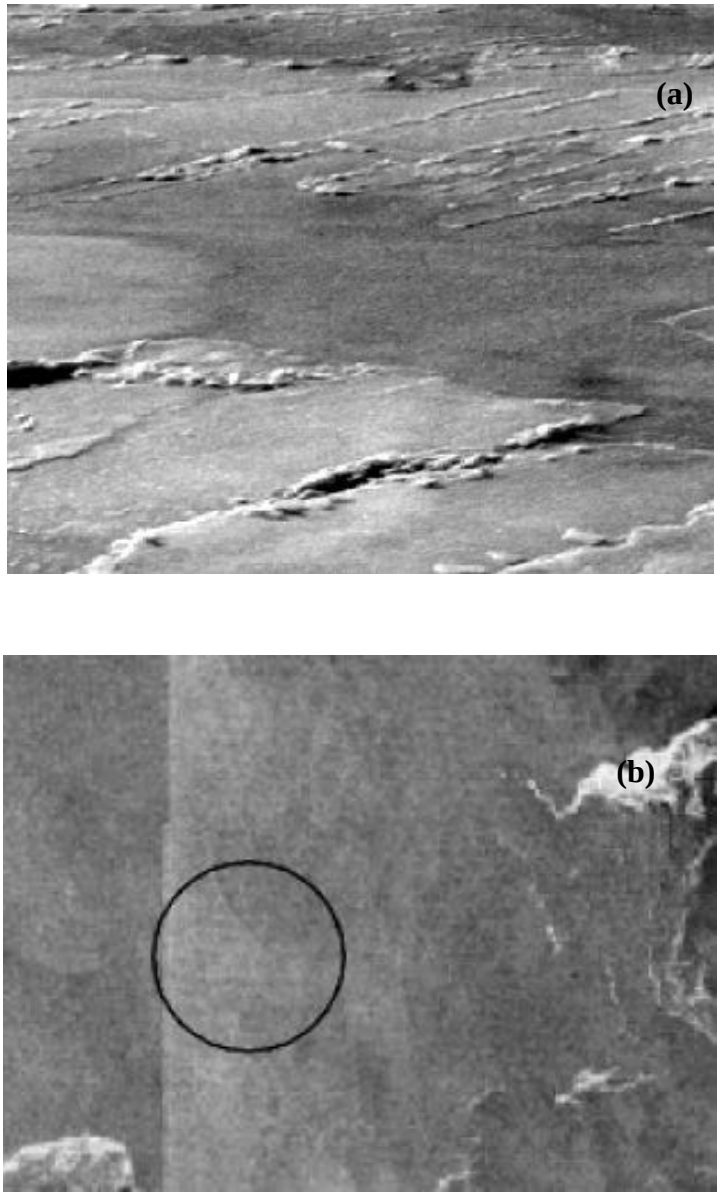

Figure 4.2: (a) Nilas with a formation of rafting, (b) nilas with a smooth surface and low backscatter inside the circle (Alexandrov et al 2007)

4.2.3 Pancake ice

When the ocean surface is rough at the time of initial ice formation, turbulence will not allow consolidation of the frazil crystals into nilas, instead, it causes frazil to undergo cyclic compression following the wave action (Sinha and Shokr 2015). The ice crystals rapidly freeze together to form near circular 5-10cm scale discs on the ocean surface (Alexandrov et al 2007). These pancakes raft and freeze together to form aggregates meters across and eventually form a consolidated ice cover tens of centimeters thick (Lubin and Masson 2006). Pancakes are usually notes as having rough edges that result from constant collisions with neighboring pancakes due to wind or wave action (Comiso 2010). During growth stages, the open water areas between pancakes are usually filled with frazil ice which serves to eventually glue the pancakes together (Comiso 2010). Figures 4.3 illustrates different stages of pancakes' growth.

Figure 4.3: Pancakes and grease ice. On the left, small pancakes with diameters of 10-20 cm and grease ice is illustrated. On the right, freely floated pancakes with diameters of 50-100 cm are illustrated (Sinha and Shokr 2015)

4.2.4 Young Ice

Young ice, which has a thickness between 10 and 30 cm, is subdivided into 10-15 cm thick grey ice and 15-30 cm thick grey-white ice (Alexandrov et al 2007). Gray ice is formed from nilas during its growth or when circular pieces of pancake ice are frozen together (Alexandrov et al 2007). As the grey ice continues to grow thicker, it becomes grey-white ice. Typically, it forms elongated ice floes with a length in the range from 1 to 10 Km separated by fractures (Alexandrov et al 2007).

These fractures can be detected in SAR images as dark lines (Alexandrov et al 2007). Grey-white ice has a medium backscatter value, which is lower than of grey ice (Alexandrov et al 2007).

4.2.5 First Year Ice

All sea ice developed from young ice from previous summer is defined as first year ice (Alexandrov et al 2007). The length of transition from young ice to first year (FY) ice depend on temperature, wind and location (Comiso 2010). At some stages, young ice and first year ice are difficult to discriminate especially when the ice sheet is un-deformed and has only few centimeters of snow cover (Comiso 2010). The first year ice is subdivided into thin, medium and thick first year ice types, with thickness of 30-70 cm, 70-120cm and more than 120 cm, respectively (figure 4.4) (Alexandrov et al 2007). During winter, ice thickness increases and thin ice becomes medium and later, first year ice (Alexandrov et al 2007). With an increase in its thickness, the backscatter of first-year ice slightly decreases (Alexandrov et al 2007).

In most cases, first year ice can be separated from both young and old ice, but, it is very difficult to separate thin, medium and thick first year ice from a SAR image (Alexandrov et al 2007). Cross-section of first-year ice is illustrated in figure 4.5

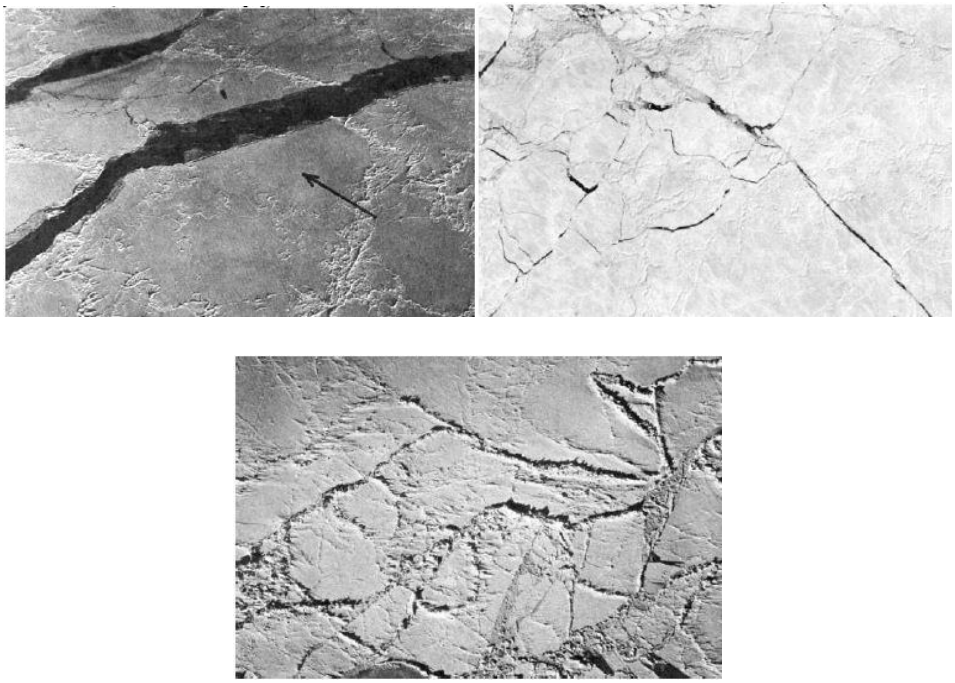

Figure 4.4. First-year ice in different stages. Upper left images shows the thin-first year ice, upper right image shows the medium-first year ice and on the bottom is the thick-first year ice (Alexandrov et al 2007)

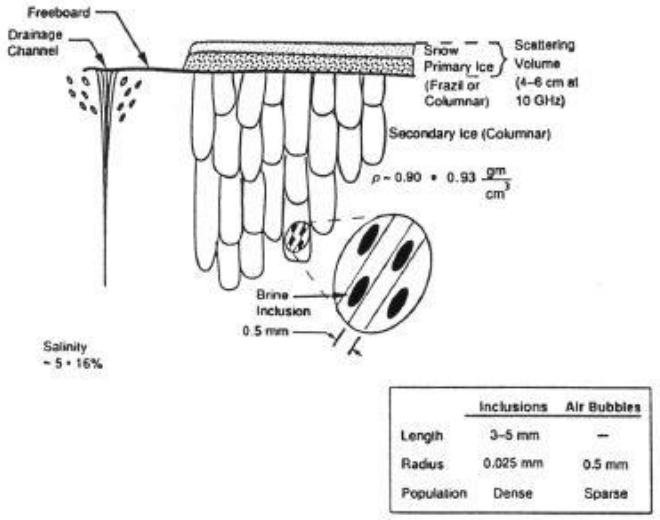

Figure 4.5: Cross-section of first-year ice (Onstott 1992)

4.2.6 Old ice

Most of the first year ice melts completely in the summer, but some are thick enough to survive the melt period and become second year ice (Comiso 2010). Old ice in subdivided into second-year (SY) ice and multi-year (MY) ice. The first-year ice that become second-year ice depends on cold the temperature gets in winter and how much rafting and ridging occurred before the summer melt period (Comiso 2010). The cycle repeats itself during the next winter period and the second year ice that survived becomes third-year ice (Comiso 2010). Multi-year ice is referred to the ice that survived at least two summers (figures 4.6 and 4.7). Cross-section of multi-year ice is show in figure 4.8.

Figure 4.6: Multi-year ice (Alexandrov et al 2007)

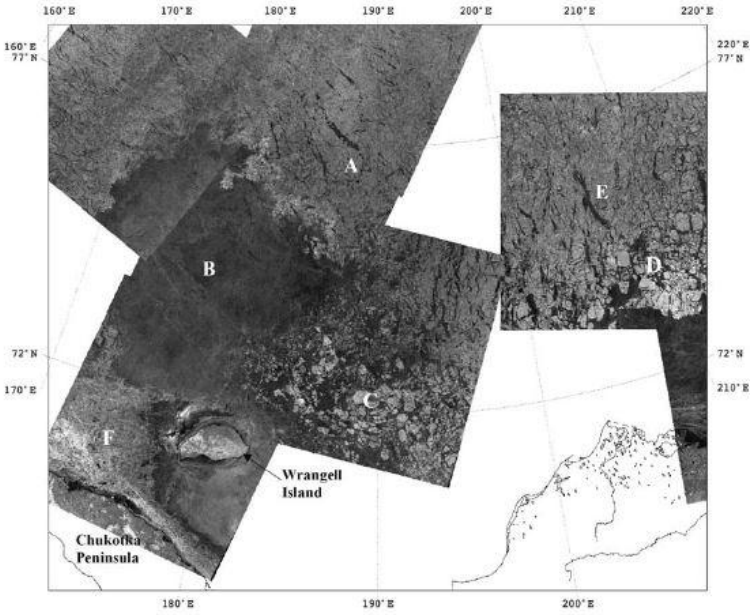

Figure 4.7: ScanSAR wide image from RadarSat showing old ice in the East Siberian Sea. Multi-year ice is illustrating in the area A which can be discriminated from first-year ice located in the area B. Floes of old ice are located in areas C and D (Alexandrov et al 2007).

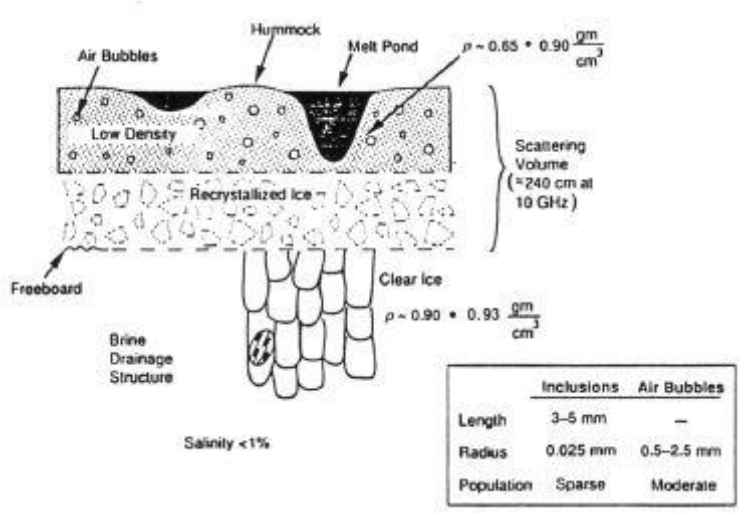

Figure 4.8: Cross-section of multi-year ice (Onstott 1992)

4.2.7 Sea ice deformation

Except for land-fast ice which freezes along the coastline, sea ice usually undergoes a complex motion at different scales (Sinha and Shokr 2015). The mobility of the ice is caused by one or more of the following geophysical forces: wind stress, ocean current stress, inertial ice resistance, sea surface tilt and tidal force (Sinha and Shokr 2015). The motion and interaction of ice floes result in ice deformation (Sinha and Shokr 2015).

Small scale deformations range from a few hundred meters to a few kilometers and are manifested in the forms of fracturing, rafting, ridging and rough ice surface (figure 4.9) (Sinha and Shokr 2015).

Figure 4.9: Pressure ridges in the Beaufort Sea (Hibler 2001)

At this scale, the deformed ice represents hazardous conditions for both marine navigation and offshore structure (Sinha and Shokr 2015). Medium scale deformations are defined by a spatial scale that extends a few tens of kilometers and are usually manifested in the forms of heavy and extensive ridging as well as cracks and leads in the ice sheet (Sinha and Shokr 2015). Large scale deformations with characteristic dimensions in the order of hundred to several hundred kilometers are caused by large circulation systems, particularly in the Arctic (Sinha and Shokr 2015).

Rifting and pressure ridging are the most common forms of ice compression at small and medium deformation scales and they contribute to the increase of ice thickness (Sinha and Shokr 2015). They occur when two ice sheets are pushed against each other (Figure 4.10) (Sinha and Shokr 2015). If the sheets are thin, rafting is more likely to occur and if they are thick, a pressure ridge will form (Sinha and Shokr 2015). Thin ice thickness that deforms into rafting is a few centimeters to a few tens of centimeters, although, rafting can be found with thicker ice when relatively small floes collide (Sinha and Shokr 2015). In rafting a moving thin ice overrides another sheet when they collide and continues ridging under compression force and against a frictional force and eventually stops when the frictional force between sheets stops (Sinha and Shokr 2015).

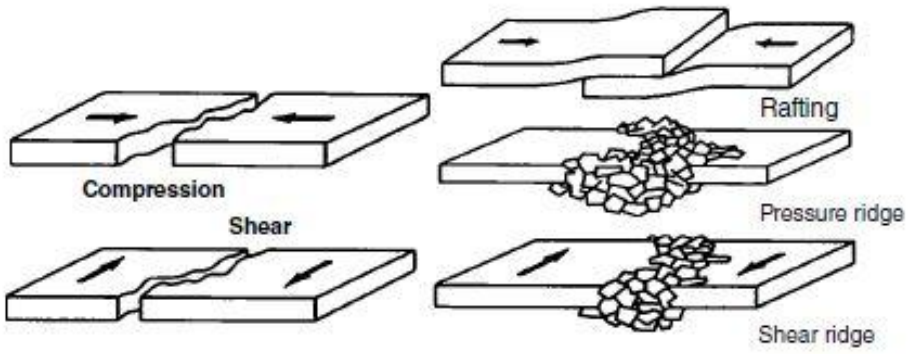

Figure 4.10: Ice cracking due to sheer forces on the left. Rafting and pressure ridging are illustrated on the right (Sinha and Shokr 2015)

4.2.8 Sea ice decay

The term ice decay refers to the decay or melting of first-year ice before it becomes second-year ice. The onset of ice decay depends on the latitude (Sinha and Shokr 2015). The overlying snow of FY ice starts to melt in mid-June and by the end of July or August, most of the FY ice would have melted (Sinha and Shokr 2015).

The prime factors that trigger the ice decay are the air temperature, incoming solar radiation and melting of snow cover (figure 4.11) (Sinha and Shokr 2015). Secondary

factors include rides, albedo, mechanical disruption (ice break up due to wind), and water temperature (Sinha and Shokr 2015). The (surface) albedo describes the fraction of the radiation reflected by the surface of sea ice (Stoffels and Wackerbouer 2012).

Sea ice decay starts at the surface in the form of melting initiated by two heat sources: (1) the absorbed solar radiation and (2) the conductive heat from the surrounding air (Sinha and Shokr 2015). The amount of absorbed solar radiation is determined by surface albedo, which varies with the type of surface (Sinha and Shokr 2015).

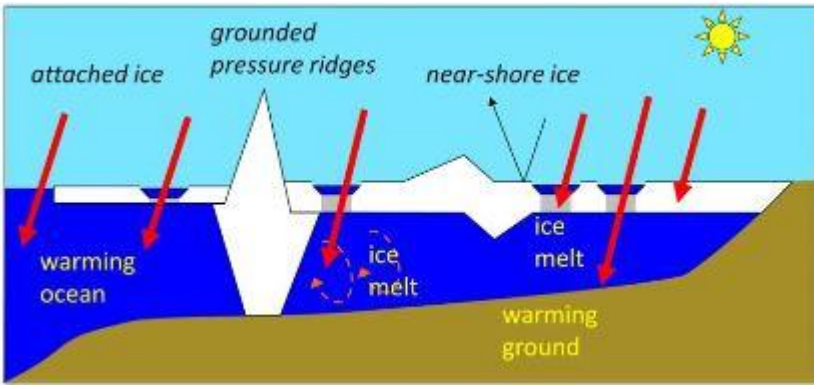

Figure 4.11: Land-fast ice decay during melt season (Source: http://seaice.alaska.edu/gi/observatories/barrow_breakup/Petrich_etal_2012_Barrow_break-up.pdf)

In the sea ice ocean system, the albedo can range from 0.9 for fresh snow to 0.07 for Open Ocean (Stoffels and Wackerbouer 2012). Values for ice lie within this interval, with young sea ice albedo around 0.7, melting ice and melting ponds down to 0.4 (Stoffels and Wackerbouer 2012). Water absorbs 90% or more of the incoming solar radiation, while melting snow absorbs 40%-60% and dry snow absorbs 10%-20% (Sinha and Shokr 2015). Higher absorption of solar radiation leads to greater increase of local temperature of the surface (Sinha and Shokr 2015). Figure 4.12 shows the decay process of sea ice

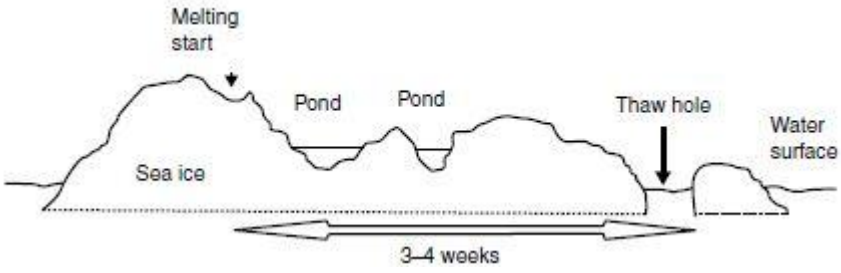

Figure 4.12: Decay process of sea ice. It usually takes between 3 to 4 weeks from the onset of surface melt for the appearance of thaw holes (Sinha and Shokr 2015)

4.3 Electromagnetic properties of sea ice

The electromagnetic properties of sea ice are governed by its physical state. The physical development of sea ice is governed by thermodynamic forcing of the ocean such as currents, water temperature, wind and all these variables contribute to the eventual sea ice roughness which determines its electromagnetic (EM) signature.

A dielectric medium can be either ideal or non-ideal. Ideal dielectrics possess no free charges to establish any conduction current, so, their conductivity is zero (Sinha and Shokr 2015). Non-ideal dielectrics possesses a very small number of free charges, hence, their electrical conductivity is small but no zero (Sinha and Shokr 2015). Permittivity is another important factor in those cases. Conductivity and permittivity of a dielectric material is combined in a single parameter termed complex dielectric constant ε, (complex permittivity) and is defined as:

$$\varepsilon = \varepsilon' - j\varepsilon'' \tag{4.0}$$

The real part of the complex dielectric constant is the permittivity and is denoted by ε' and the imaginary part is the conductivity denoted by jε''. Permittivity determines how much energy penetrates through the material and electrical conductivity determines how much energy is lost or scattered inside the material. High permittivity means less

penetration of energy (hence more scattering at the surface), while high loss means more energy dissipation inside the material (Sinha and Shokr 2015).

4.3.1 Pure ice

For pure ice, the real part of the complex dielectric constant is independent of frequency between 100 MHz and 900 GHz with weak dependence on temperature (Sinha and Shokr 2015). On the other hand, the imaginary part of the complex permittivity depends on both temperature and frequency of the EM signal. For calculating the real part of the complex dielectric constant, the following model is used:

$$\mathrm{Re}(\varepsilon_{ice}) = (3.099T - 992.65) / (T - 318.896) \quad (4.1)$$

Where T is the ice temperature.

The imaginary part of pure ice can be calculated as follows:

$$\mathrm{Im}\varepsilon_{ice} = \frac{A(T)}{f} + Bf \quad (4.2)$$

Where f denotes the frequency in GHz and the letters A and B are the coefficients that depend on the ice temperature. The values for A (T) and B (T) are calculated as follows:

$$A(T) = \frac{e^{\left[12.5 - \frac{3.77\,10^3}{T}\right]}}{T} \quad (4.3)$$

$$B(T) = 10^{-4} Re(\varepsilon_{ice})(273.41 - T)^{-1/2} \quad (4.4)$$

The presence of impurities (dust particles, ash particles, Sodium and Chloride ions) on ice can influence the values of permittivity. Impurities in the ice can change the values of both imaginary and real parts of the complex dielectric constant.

4.3.2 Dry snow

Dry snow can be seen as a mixture of ice and air, with permittivity depending on the permittivities of the single constituent materials and fractional volume (Sinha and Shokr 2015). Snow that has undergone several melt-freeze cycles tend to form multiple clusters and its density slowly increases with time due to metamorphism and melt-freeze cycles (Hallikainen and Winebrenner 1992). The real part of snow permittivity remains constant with temperature and frequency and is affected by the fractional volume of the snow. Hallikainen, et.al (1986) proposed two equations for the real part of the dry snow.

$$\varepsilon'_{ds} = 1 + 1.83 p_{ds} \qquad p_{ds} \leq 0.5 g/cm^2 \tag{4.5}$$

$$\varepsilon'_{ds} = 0.51 + 2.88 p_{ds} \qquad p_{ds} \geq 0.5 g/cm^2 \tag{4.6}$$

Where p_{ds} is the density of dry snow in g/cm^2

4.3.3 Wet snow

Wet snow can be seen as a mixture of dry ice and liquid water, which can appear as free or bounded and is therefore more difficult to characterize electromagnetically than dry snow (Sinha and Shokr 2015). The snow permittivity can be written as:

$$\varepsilon = \varepsilon_{ds} + \Delta\varepsilon \tag{4.7}$$

The ε_{ds} term denotes the permittivity of the dry snow and $\Delta\varepsilon$ denotes the presence of liquid water.

The table 4.0 shows the empirical relations between the presence of liquid water $\Delta\varepsilon$, and snow wetness.

Empirical relation	Remarks
$\Delta\varepsilon = 0.206 * Wv + 0.0046Wv^2$	$0.01 \leq$ freq $\leq$ 1 GHz
$\Delta\varepsilon = 0.02 * Wv + (0.06\text{-}3.1*10^{-4}freq - 4)^2)Wv^{1.5}$	4 $\leq$ freq $\leq$ 12 GHz
$\Delta\varepsilon = 0.089Wv + 0.0072Wv^2$	freq = 1GHz
$e'' = 0.073 * (e')^{1/2}Wv/freq$	4 $\leq$ freq $\leq$ 12 GHz
$e'' = 0.073 * Wv + 0.0007Wv^2$	freq = 1 GHz
$e'' = c\ (freq) * Wv^{1.5}$	

Table 4.2: relation between ε'' or Δε and snow wetness (Sinha and Shokr 2015)

4.3.4 Brine inclusions

As the sea ice grows thicker, it rejects brines to the ocean. Any brine within sea ice is contained in millimeter to centimeter scale enclosures and tubes between the crystals of recently formed sea ice (Haskell et.al 2012). These tubes provide a route for salt to leave the ice. As these networks close off, their remnants are the small brine inclusions that determine many of the physical properties of sea ice (Haskell et.al 2012). The brine inclusions of the sea ice have high permittivity that affects the electromagnetic properties of sea ice. Brine has a high dielectric loss factor which attenuates the EM signal. For instance, the backscatter from a thin saline ice will be low, while, the multi-year ice which is less saline produces higher backscatter.

4.3.5 Air bubbles

Air bubbles in the sea ice which exist at depths above the water level influence the dielectric properties of sea ice, as a result increasing the scattering effect. The saline-free nature of the upper layer of multi-year ice allows more microwave energy to penetrate and interact with air bubble (Sinha and Shokr 1994). As microwave energy interacts with air bubbles, multiple scattering occurs, which, together with the surface scattering, gives the total backscatter received by the SAR sensor.

4.4 Microwave interaction with sea ice

Sea ice types, leads, ridges, icebergs and other geological features have their own unique microwave signature that can be discriminated from radars. Hence, backscatter is influenced by different aspects of sea ice structure (Onstott 1992). The microwave energy can interact with the snow surface, the interior of the snow, the upper layer of the ice sheet (as the microwave penetrates through the snow), the interior of the ice sheet and the water surface. The way in which sea ice forms, its history, and its age are important in determining its microwave properties (Onstott 1992). When the ice is young, it exhibits a thin layer of brine on its surface, thereby limiting electromagnetic wave propagation to depths of a wavelength of less (Onstott 1992). The volume of the brine reduces as the ice gets older which enables the electromagnetic wave to penetrate further in the ice. Also, the selection of radar polarization (Horizontal or Vertical), its wavelength (X-band, C-band or L-band) and viewing angle can help in determining the dominant scattering mechanism of sea ice (surface or volume scattering). The figure 4.14 illustrates the interaction of electromagnetic wave with different sea ice types.

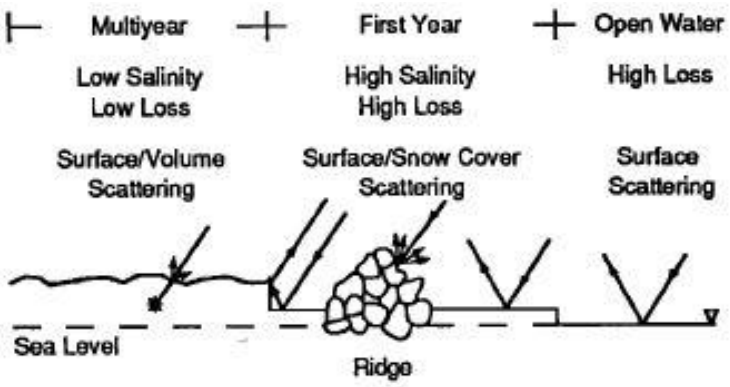

Figure 4.13: Interaction of electromagnetic wave with first year ice, multi-year ice and open water (Onstott 1992).

4.4.1 Microwave scattering from New and First Year Ice

New ice is composed of a thin layer of ice of few centimeters up to 10-20 cm thick. As the ice forms, the amount of brine is considerable high. Hence, new ice can be characterized by a high fractional brine volume and an effective dielectric constant that, while considerably smaller than that of seawater, is large relative to that of thick ice (Hallikainen and Winebrenner 1992).

As the ice gets thicker, passing the stage of grey ice and becomes first year ice, its salinity reduces, the surface becomes rougher and it acquires snow cover. The backscatter intensity of sea ice depends on different factors such as surface roughness, dielectric constant, incidence angle and the radar frequency. The dominant backscatter mechanism associated with first year ice is surface scattering (Onstott 1992). Its lower absorption of electromagnetic wave, the lower amount of brine volume and the surface roughness tend to increase scattering. Observations show that snow on sea ice plays an important role in determining the backscatter response from first year ice (Hallikainen and Winebrenner 1992). The dry snow on top of the sea ice is transparent to electromagnetic wave (for frequencies of 5.5 GHz which corresponds to C-band of radar instrument) due to low dielectric permittivity and the small grains compared to microwave length. The snow as well as the ice surface cause a specular reflection to horizontally polarized waves, whereas vertically polarized waves are transmitted through the sea ice. Backscatter cross sections for first year ice are roughly 5 decibels (dB) higher than for new ice at frequencies from 1 GHz up to at least 10 GHz (Hallikainen and Winebrenner 1992). A sea ice core from first year ice is illustrated in the figure 4.15. The upper layer of FYI contains some amount of brine (roughly 10 ‰) which prevent the microwave from penetrating through.

Figure 4.14: FYI core with diameter 100 mm. The brine is ejected through the drainage channel (Sinha and Shokr 1994)

4.4.2 Microwave scattering from Multi-Year Ice

Multi-Year Ice is the ice that has survived a summer melt season and continued to grow thicker. The upper part of MYI consists of fresh, raised areas (hummocks) with bubbly, low-density upper layers and lower lying, higher density areas that are refrozen melt ponds (Hallikainen and Winebrenner 1992). The small sized bubbles in the MYI (the size of millimeter) as well as its low absorption leads to volume backscattering. The intensity of the backscatter (σ^o) of the MYI is stronger than that of the FYI at wavelength of 5.8 cm (C-band) and above. Hence, volume scattering occurs when the microwave energy interacts with the sea ice and the energy is scattered by the bubbles inside the old ice. The figure 4.15 illustrates the volume scattering of the sea ice. The considerable amount of bubbles exists in the upper part of MY hummock ice is responsible for the strong backscatter of the microwave.

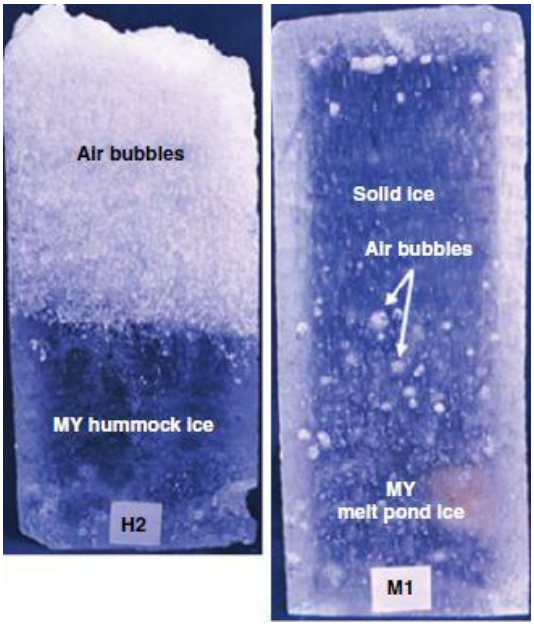

Figure 4.15: .MYI cores (Sinha and Shokr 1994)

When a significant part of the electromagnetic wave is scattered itself and re-scattered inside the medium then multiple scattering occurs. Multiple scattering takes place when there is a little absorption to soak up energy and when individual scattering events redirect a significant amount of energy (Hallikainen and Winebrenner 1992). On the other hand, single scattering tends to dominate when the medium is lossy so that multiple scattered waves are strongly attenuated (Hallikainen and Winebrenner 1992). The look up table below (table 4.1) shows the backscatter coefficients of sea ice types that were derived from measurements carried out in different frequencies.

4.4.3 Optimum frequency and polarization

During winter, the critical mechanism in separating first-year and multi-year ice is discriminating backscatter dominated by volume scattering from that dominated by surface scattering (Onstott 1992). Despite the fact that the surface texture of these two

sea ice types is similar, the volume scattering from multi-year ice enables us discriminating it from first year ice. Surface scattering increases with frequency. The optimum frequency will be one that exploits the fact that volume scattering dominates (Onstott 1992). Hence, one should choose a wavelength (λ) such that surface scattering remains the principal backscatter mechanism for first year ice, also, the wavelength should be short enough for strong multi-year ice volume scatter (Onstott 1992). In summer, high frequency wavelengths (X-band with frequency of 9.6 GHz) are not suggested because they cannot penetrate the wet snow. On the other hand, longer wavelengths such as L-band (23cm) are less sensitive on the dielectric constant of the wet snow and can interact with sea ice. Hence, using L-band the sea ice discrimination is feasible.

Apart from choosing the ideal frequency on sea ice observations, polarization choice plays an important role as well. For sea ice discrimination, HH and VV polarizations are similar. However, for open water and calm conditions, the cross section at VV polarization is 5 to 7 dB greater than at HH polarization (Onstott 1992). For thin ice, the backscatter coefficient at HH polarization is 2 to 3 dB lower that it is in VV polarization.

An accurate interpretation of a single polarized SAR images is hard to achieve. Dual polarization improves the discrimination of the sea ice features due to the fact that two polarization channels as used (HH + HV) instead of one (HH or VV). Cross-polarization has been shown to increase the range between multi-year and first year returns by an additional 3 dB (Onstott 1992). This is attributed to the very weak depolarization that occurs over smooth and slightly rough surfaces (Onstott 1992).

A research conducted by Abreu et.all 2006 at Beaufort Sea has shown that HV channel produced a greater contrast between MYI and the rough FYI compared to HH channel. In the HH polarization channel the rough FYI was almost indistinguishable from the MYI.

Season	Ice type	Thickness (cm)	X (HH) - σ^0	C (VV) - σ^0	L (HH) - σ^0
winter	MY	>220	-3.6	-8.6	-7.0
	TKFY	70-220	-14.2	-11.5	-23
	TNFY	20-70	-	-13.5	-23.4
	OW	0	<-29.7	>= -29.7	<= -30.7
Late spring	MY	>220	-	-10.7	-15.5
	TKFY	70-220	-	-13.2	-23.4
	OW	0	<-29.7	<-19.7	<= -30.7
Early summer	MY-TKFY	>70	-15.9	-16.3	-15.1
	TNFY	20-70	-15.1	-13.1	-
	OW	0	<-29.7	<= -19.7	<= -30.7
Mid-summer	MY	>220	-15.7	-16.3	-22.7
	TKFY	70-220	-15.7	-14.7	-19.8
	TNFY	20-70	-14.7	-13.1	-19.8
	OW	0	<-29.7	<= -19.7	<= -30.7
Late summer	MY	>220	-	-16.8	-21.9
	TNFY	20-70	-	-18.6	-28.1
	OW	0	<-29.7	-19.7	<= -30.7

Table 4.3: Look up table of backscatter coefficients (Shokr and Sinha 2015)

.

5 Methodology

5.1 Introduction

This chapter describes the methodology that has been followed for performing sea ice classification. An overview of this procedure is illustrated in the scheme below.

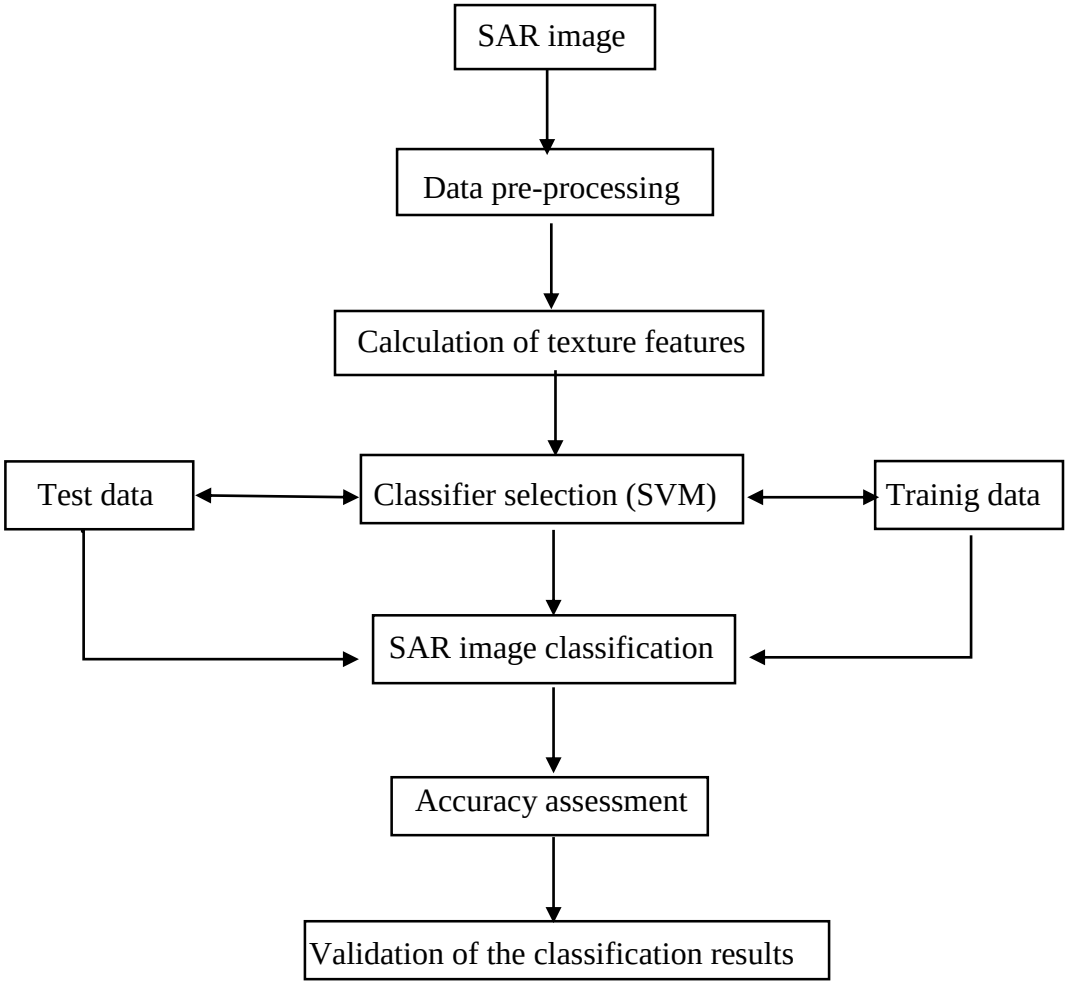

Figure 5.0: A workflow of the steps for the SAR data processing

5.2 Area of study

The study area is located in the Eastern part of Greenland with coordinates, $71.81^{o}\ latitude$, 21.47^{o} longitude (upper left), $67.60^{o}\ latitude$, $21.08^{o}\ longitude$ (bottom right). Ittoqqortoormiit is the only settlement located along the coast of the area of interest. It attracts many tourists every winter as well as people interested in sports such as climbing and hiking.

Figure 5.1: Area of study. The red rectangular on the map indicates the area of interest.

5.2.1 Climate and oceanography

Greenland is an island where strong winds are present all year round, especially in winter. Strong and cold winds descent from the North Pole to the southern part of Greenland. For the South-East part of Greenland, it is exposed to high and strong winds as well as to gale

forces which occur 15-20 % of the time. The velocity of winds can reach 25m/s or even higher.

The surface layer in the Eastern part of Greenland Sea is dominated by the northward flowing Norwegian Atlantic Current (Pedersen et.al, 2004). Atlantic waters recirculate and are transported to the South-East part of Greenland through the Fram Strait region (figure 5.2). The East Greenland current flows southern along the coast of East Greenland (Pedersen et.al, 2004). Currents, known as Irminger current, turns westward along the west coast of Island (Pedersen et.al, 2004).

Sea ice in South-East part of Greenland primarily occurs as multi-year drift ice of Polar region is carried to Southern Greenland. The Northerly winds cause fresh polar water from the Arctic Ocean with large amount of Polar ice to be carried along the East coast of Greenland by strong currents (Buch, 2000).

Figure 5.2: Ocean surface currents in Greenland's waters (Pedersen et.al, 2004)

5.3 Data description

SENTINEL -1 data are used for this study. SENTINEL-1 was built for acquiring data that can be used in many applications. One of these applications include sea ice monitoring. The satellite can capture data in high and medium resolution that can be used for generating sea ice maps for the safety of ships navigation. The radar can distinguish between thin and a thicker sea ice as well as thick from the hazardous much thicker ice providing valuable help and safety into the ice covered Artic zones.

Two SENTINEL-1 Extra Wide Swath (EW) images acquired over the same area of the South-East part of Greenland waters ($71.81^o\ lat$, 21.47^o long (upper left), $67.60^o\ lat$, $21.08^o\ long$ (bottom right)) in HV and HH polarizations in February 23 of 2016 and May 25 of 2016. The second image was captured three months later where it will give us an indication of how much the sea ice has changed in a period of three months. The spatial resolution of the products is 40m with an incidence angle range from 20^o to 47^o. The detailed description of the data are given in the table 5. Figures 5.3 and 5.4 depict the SENTINEL-1 SAR images.

Parameters	**SAR configurations**
Product type	Ground Range Detection (GRD)
Acquisition mode	Extra Wide Swath (EW)
Incidence angle	20 – 47 (degrees)
Polarization	Dual (HH+HV)
Swath	410 Km
Azimuth looks	3
Range looks	6
Spatial resolution	40m
NESZ	-22 dB

Table 5: SENTINEL-1 data description

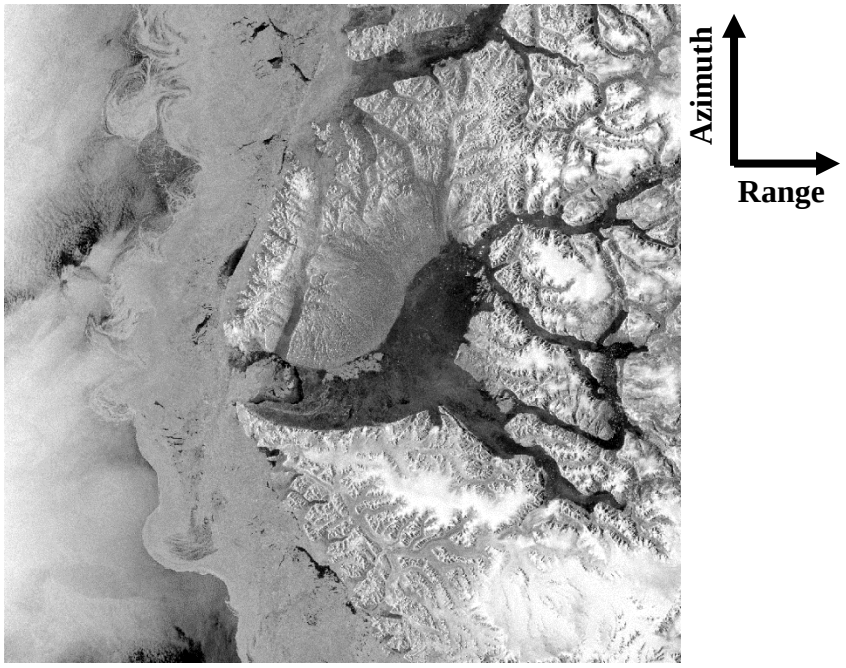

Figure 5.3: SENTINEL-1 image acquisition in satellite geometry captured in February 23 of 2016

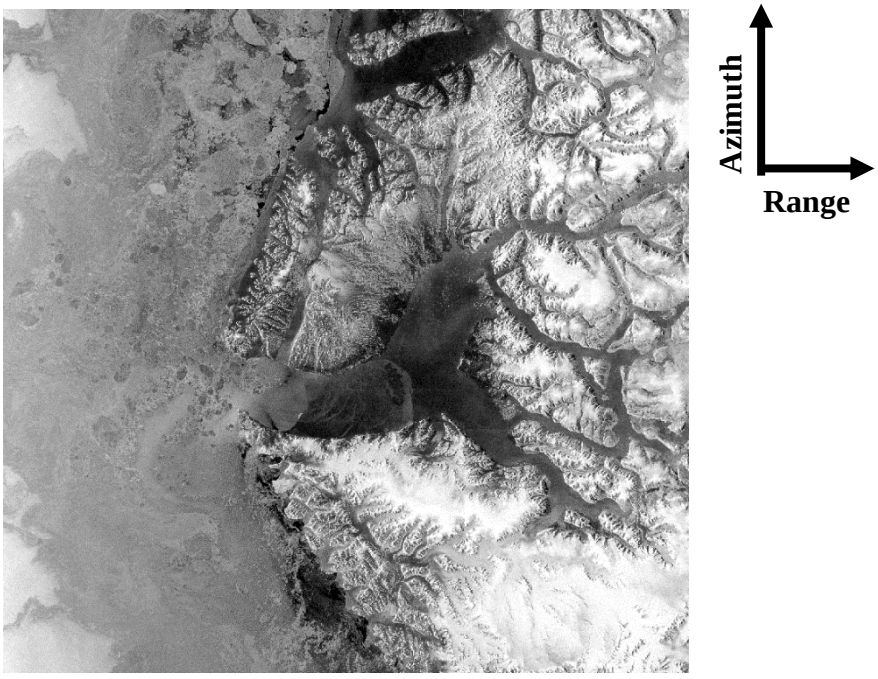

Figure 5.4: SENTINEL-1 image acquisition in satellite geometry captured in May 25 of 2016

5.4 Data pre-processing

Satellite imageries acquired by SAR sensors contain uncertainties which have to be properly corrected before proceeding to SAR image post-processing. The pre-processing steps of the SENTINEL-1 image include, applying precise orbit file for more accurate geolocation of the SAR image, thermal noise removal, calibration, incidence angle correction and speckle noise reduction.

These steps are described in detail below. A general scheme of the pre-processing steps is illustrated in figure 5.5.

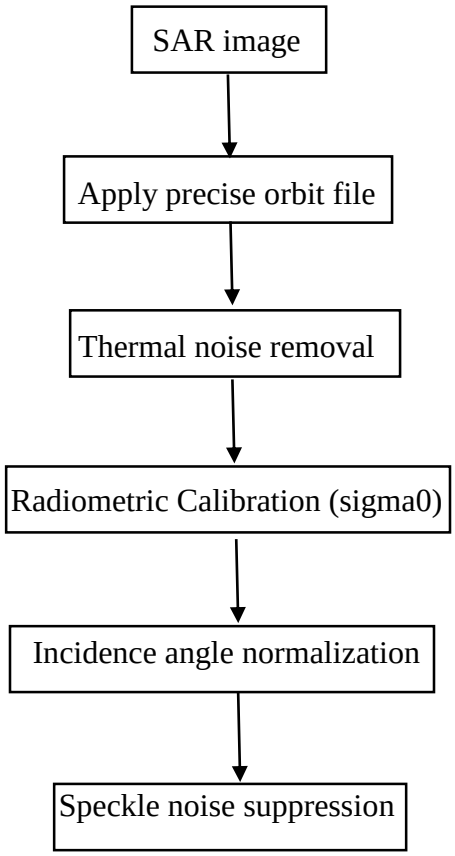

Figure 5.5: Flow chart of pre-processing steps for the SENTINEL-1 data

5.4.1 Precise orbit file

Precise orbit information is necessary for accurate geolocation of the SAR product. The location accuracy of the SAR image depends on the orbit information, incidence angle and the Digital Elevation Model (DEM) that is used for ortho-rectification. In order to retrieve the highest location accuracy, the best orbit information that is available should be used.

Precise orbit state vectors has not been applied for the SENTINEL-1 images as they are available days or weeks after the product generation. Hence, precise orbit ephemerides (POEORB) has been applied to both SENTINEL-1 datasets for a precise geolocation of the SAR images.

5.4.2 Thermal noise removal

Ground Range Detected (GRD) SENTINEL 1 SAR images suffer from thermal noise. The noise can be noticed in areas of low backscatter signal (calm waters, lakes, etc.). The cross polarization (HV) images are mostly affected by thermal noise because the signal received from the sensor is too low (close to the noise floor) and too noisy to be useful. Moreover, in multi-swath acquisition modes this noise has typically a different intensity in each sub-swath, causing an intensity step at inter-swath boundaries (Piantanida et.al 2016). During raw data focusing, a range varying radiometric corrections applies on SAR data resulting in a re-shaped noise contribution in a range varying fashion (Piantanida et.al 2016).

Hence, the thermal noise can be removed improving the quality of the SAR image. The thermal noise level vectors are given in the metadata file of the SAR product and this enables us to remove it. The equation shown below is applied for subtracting the noise from the image.

$$E[s(R,\eta)^2] = E[(s(R,\eta) + n(n_s\,;\eta))^2]\; G_{tot}^2\;(\eta_s) \tag{5.1}$$

R, η - $\sigma_n^2\;(n_s,\,\eta)\; G_{tot}^2\;(n_s,$R, η)

Where:

R: slant range

η: slow time

n_s: sub-swath number

$s(R, \eta)$: received backscatter signal

G_{tot}^2 (n_s,R, η) : total gain applied to the data during SLC processing

$n(n_s\,;\eta)$: bi-dimensional white thermal noise for a given swath

5.4.3 Radiometric calibration

The SAR products used for this study are characterized as level 1. For this type of product radiometric calibration has not been applied. The objective of radiometric calibration of SAR images is convert the digital number (DN) of each pixel into physical units. After the interaction of radar wave with the surface of the earth, factors such as system loss, antenna gain and the aperture of the antenna should be accounted for, otherwise a significant radiometric bias in the SAR image is introduced and renders it unsuitable for use in applications that entail quantitative use of SAR data (El-Darymli 2014). Radiometric calibration provides for converting the pixel values in the SAR image from being qualitatively representative of the biased backscatter signal to being quantitatively representative of the backscatter coefficient (El-Darymli 2014). Also, radiometric calibration is important for comparing SAR images captured with different SAR sensors.

The calibration parameters for SENTINEL 1 images are given in the Look Up Table (LUT). In order to radiometrically correct the product, the equation below is used.

$$\sigma^o = \frac{DN^2}{A_{dn}^2\, k} \sin(a) \qquad 5.2$$

Hence, the radar cross section (A_σ) is written as:

$$A_\sigma = \sqrt{\frac{A_{dn}^2\, k}{\sin(a)}} \quad 5.3$$

The other values in the LUT are defined as:

$$A_\beta = \sqrt{A_{dn}^2}\mathrm{k} \quad 5.4$$

$$A_\gamma = \sqrt{\frac{A_{dn}^2\, k}{\tan(a)}} \quad 5.5$$

Where:

a, is the local incidence angle

A_{dn}, is the product final scaling from SENTINEL 1 Single Look Complex (SLC) to final Ground Range Detected (GRD) product

K, is the calibration constant

It is also possible to calibrate the SAR image using the calibration parameters directly from LUT. The equations are described below

$$\sigma^o = \frac{DN^2}{A_\sigma^2} \quad 5.6$$

$$\beta^o = \frac{DN^2}{A_\beta^2} \quad 5.7$$

$$\gamma^o = \frac{DN^2}{A_\gamma^2} \quad 5.8$$

After deriving the values for σ^o, β^o and γ^o, we can convert these values into decibel (dB) units as follows:

$$\sigma_{\gamma\beta}^o = 10\ log_{10}\ \sigma^o \quad 5.9$$

The SENTINEL-1 products come with four look up tables that allow for A_β, A_σ, A_γ, and $A_{dn.}$ A_β is used to transform the radar reflectivity into β^0 where the area normalization is aligned with the slant range (Miranda. and Meadows 2015). β^0 is known as radar brightness coefficient and is dimensionless. A_σ is used to transform the radar reflectivity into radar cross-section σ^o where the area normalization is aligned with ground range plane (Miranda. and Meadows 2015). σ^o is the radar cross section per unit area in the ground area (El-Darymli 2014). $A\gamma$ is used to transform the radar reflectivity into gamma γ^0 where the area normalization is aligned with a plane perpendicular to slant range (Miranda. and Meadows 2015). γ^0 is the radar cross section per unit area of the incident. Figure 5.6 shows schematically the three scattering coefficient5

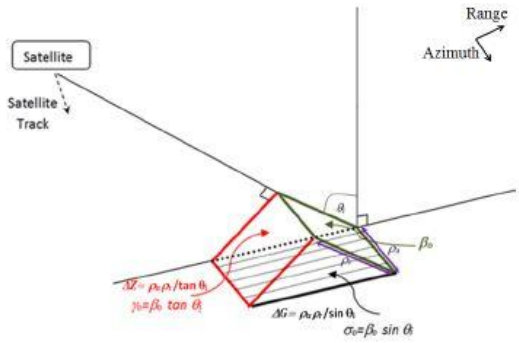

Figure 5.6: The relationship of three scattering coefficients (β^0,γ^0 and σ^o). (El-Darymli et.al 2014)

5.4.4 Incidence angle normalization

The Extra Wide (EW) swath mode of SENTINEL-1 acquires data over a wide area with a swath over 400 Km. The main problem related to EW mode is the degrease of backscatter energy from near to far range of the SAR image. The backscatter coefficient values, depend to a great extent on the incident angle. This means that the backscatter energy at low incidence angle is higher from that at high incidence angle. Therefore, incidence angle normalization is required to reduce the variation of backscatter energy over the SAR scene.

Topouselis et.al 2016 suggested a methodology for correcting the incidence angle for images acquired in wide swath mode. Incidence angle correction can be carried out according to equation 5.10.

$$\sigma^0_{\theta ref} = \frac{\sigma^o_\theta + (\sigma^0_\theta)^{-1}}{2} \qquad 5.10$$

Where, $\sigma^0_{\theta ref}$ is the normalized backscatter coefficient at a reference incidence angle, θ_{ref}, σ^0_θ is derived by using a linear regression model which describes the relation of σ^0 values and incidence angle and $(\sigma^0_\theta)^{-1}$ is the symmetric function of σ^0_θ . The σ^0_θ parameter is derived by:

$$\sigma^0_\theta = a\theta + b \qquad 5.11$$

Where, a and b are the linear coefficients. The $(\sigma^0_\theta)^{-1}$ parameter which is the symmetric function can be derived as follows:

$$(\sigma^0_\theta)^{-1} = -a\theta + 2a\theta_{ref} + b \qquad 5.12$$

5.4.5 Speckle noise removal

All SAR images suffer from speckle noise. The presence of speckle noise in the image degrades its quality and the image interpretation becomes more difficult. The speckle noise comes from the fact that scatters within the resolution cell interfere destructively. The speckle effect in SAR images varies over homogeneous areas. If we consider a case of a distributed target, such as agricultural field that has characteristics such as surface roughness that are statistically homogeneous, the adjacent pixels in the SAR image will exhibit a different backscattered echo (Woodhouse 2006). Despite the fact that an agricultural area looks homogeneous in the SAR image, the scatterers between two adjacent homogeneous pixels will differ changing the scattered interference pattern.

The speckle noise is based on the assumption that the resolution cell contains a large number of scatterers with a wavelength hat is comparable to the roughness of the terrain (Mascarenhas 1997). In this case, the returned wave is the result of the superimposition of all these reflected components (Mascarenhas 1997). A vector representation of speckle noise is illustrated in figure 5.7

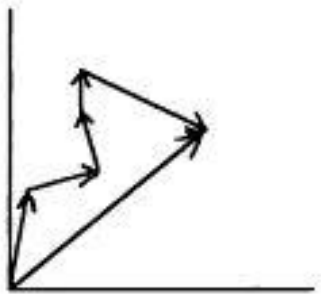

Figure 5.7: Contribution of different scatterers in a resolution cell (Mascarenhas 1997)

It is necessary to apply a de-speckle filter on SAR data for noise suppression before using it for further processing. Many speckle suppression filters have been developed for remotely sense data the last years. Regarding a radar image, a performance of a filter should not be assessed only on suppressing the noise, but preserving the edges of the

features in the image as well. Filters such as median and mean have been developed to suppress the noise but they have poor performance and fail to preserve the edges.

More complex filters are necessary for effectively removing the speckle effect from SAR images. Some of the most popular filters that have been extensively used on SAR images are the Frost, Lee, Lee sigma, median and boxcar filter. An extensive research on assessing the performance on these filters on SAR images has been carried out by many authors (De Leeuw and de Carvalho 2009, Qiu et.al 2004, Lee 1981, Lee et.al 2009, Joshi and Garg 2012).

The simplest de-speckle filter is the median in which the central pixel of a moving window is replaced by its median. The median filer successfully suppress the noise of a SAR but it does not preserve single pixel wide features, which will be altered if speckle noise is present (Qiu et.al 2004). Adaptive filters, such as Lee filter, are based on the assumption that the mean and variance of the pixel of interest are equal to the local mean and variance of all pixels within the user selected moving window (Qui et.al 2004). The Lee filter suppresses the noise by minimizing either the weighted least square estimation or the mean square error (Qui et.al 2009). The frost pixels replaces the pixels of interest with a weighted sum of the value within the moving window, the weighting factors decrease with distance from the pixel of interest and increase for the central pixels as variance within the window increases (Qui et.al 2009).

The Lee sigma filter on the other hand is simple but superior to the other sophisticated filters and it one of the most widely used suppression filters in SAR images. It first computes the sigma (standard deviation) of the entire scene, and the replaces each central pixel in a moving window with the average of only those neighboring pixels that have an intensity value within a fixed sigma range of the central pixel (Qui et.al 2009). Also, The Lee sigma filter is superior in preserving the edges, linear features and texture information.

6 Texture analysis

6.1 Introduction

Developing automatic ice classification methods for SAR images has been a long-standing goal for sea ice research and operational ice charting services (Alexandrov et.al 2013). The objective of sea ice classification of SAR images is to identify the main sea ice features related to ice types and surface roughness and classify them into a set of pre-defined categories (Alexandrov et.al 2013). An efficient classification method, which it can be either supervised or unsupervised, involves choosing the ideal image parameters for classifying sea ice classes effectively. These parameters should be chosen before the implementation of the classification algorithm. The two type of parameters that are widely used in remote sensing for describing a satellite imagery are the tonal and textural parameters. Tonal parameters describe the reflected energy received by the satellite sensor (gray tone) after interacting with the surface of the Earth. Texture contains important information about the structural arrangement of surfaces and their relationship to the surrounding environment (Haralick. and Shanmugam 1973).

At the early stages of sea ice discrimination, attempts of using first order statistic approach have been made. This technique utilizes the backscattering coefficient (σ^o) of the SAR image for sea ice type separation. Using this method, the discrimination between First Year (FY) ice (which is about 0.3m thick) and Multi Year (MY) ice (where its thickness ranges between 2 and 4m) is possible but it is hampered by ambiguities in separating different FY ice classes because of the similar backscatter signatures. Several studies that have been carried out suggest that using first order statistics alone is not able to successfully discriminate all the different sea ice types (Holt et.al; Robert et.al 1987; Kwok and Cunningham 1994; Fettere et.al 1994).

As tonal statistics have failed in clearly discriminating sea ice types, researchers used the texture information of the image. Texture statistics helped in improving the discrimination of sea ice types. Some of the widely used texture feature extraction methods are the

wavelet transform, Grey Level Co-occurrence Matrix (GLCM) and Gabor filters. There are evidence to indicate that texture is more suitable than tonal features for extracting information from SAR sea ice imagery (Clousi 2002; Soh and Tsatsoulis 1999). However, texture analysis alone may not be sufficient for discriminating the SAR sea ice data (Clousi and Deng 2004).

6.2 Grey Level Co-Occurrence Matrix

Grey level Co-Occurrence Matrix describes how often a combination of two pixels (grey level values) occur in an image within a pre-defined computational window. GLCM takes into account the relation between two adjacent pixels, the reference and the neighbor pixel. GLCM is considered as second order statistics. Unlike first order statistics (Kurtosis, Skewness), second order statistics consider the relationship between the reference and the neighbor pixel in the image. Once the GLCM matrix is calculated, statistical parameters can be derived from the matrix to characterize texture (Shokr 1991).

For the creation of GLCM matrix, four important parameters are considered. These parameters are the orientation, displacement, grey level values and a window size. The GLCM is a square matrix of dimension N and is computed using a number of quantized levels within a given computational window (Shokr 1991). An entry P_{ij} of the matrix represents the number of occurrences of two neighboring pixels, at locations (X_1, Y_1) and (X_2, Y_2) within the window which have grey levels equal to i and j respectively (Shokr 1991). The two pixels are separated by a distance (in pixels) δ and an orientation θ. Four orientations are available 0^o, 45^o, 90^o, 135^o. The entries of each matrix are normalized by dividing each entry by the total number of paired occurrences of quantized levels along the given direction (Shokr 1991). The mathematical equation of GLCM is given below.

$$P_{r(x)} = \{C_{ij} \mid (\delta, \theta)\} \qquad 6.1$$

Where C_{ij} is the co-occurrence probability between gray levels i and j and is defined as,

$$C_{ij} = \frac{P_{ij}}{\sum_{i,j=1}^{G} P_{ij}} \qquad 6.2$$

Where P_{ij} represents the number of co-occurrence of gray levels i and j within a computational window with defined δ and θ values and G represents the number of gray level values. The denominator represents the total number of co-occurrence of gray levels i and j.

6.2.1 GLCM parameters

As we have already mentioned above, four parameters (orientation, displacement, gray level values and computational window) should be considered before calculating the GLCM matrix. Each of these values should be carefully selected in order to achieve the best separation between sea ice types. These parameters are described below in more details. Table 6.0 shows what GLCM parameters have been chosen by different authors for the interpretation of SAR sea ice image.

Authors	**δ**	**θ**	**G**	**Co-occurrence statistics**
Barber and LeDrew (1991)	1*, 5, 10	0, 45, 90	16	CON,COR, DIS, ENT, UNI
Holmes, et.al (1984)	2	Average	8	CON, ENT
Shokr (1991)	1 ,2*, 3	Average	16, 32	CON,ENT, IDM,UNI,MAX

Table 6.0 Selected number of studies for GLCM parameters. The asterisk indicated the preferred choice (Clausi, 2002)

6.2.1.1 Orientation

Orientation describes the direction in which the co-occurrence matrix will be computed as shown in figure 6.0.

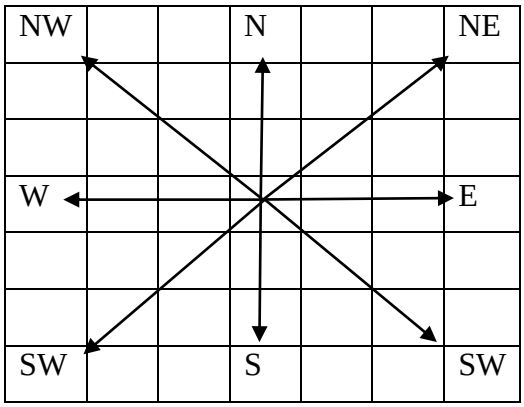

Figure 6.0. Orientation

The diagram shows eight different orientations that can be chosen but only four (N, S, W, E) are widely used. The orientation parameter is less significant compared to the other factors in co-occurrence matrix. A few studies have been conducted on what orientation should be used (table 6.0 above). The majority of the authors used the average among the four orientations. For SAR sea ice imagery, there are no symmetric patterns based on orientation (Soh and Tsatsoulis 1999). Sea ice feature rotate in all directions in given weather conditions, therefore, the orientation factor is not so important in SAR sea ice research (Soh and Tsatsoulis 1999).

6.2.1.2 Displacement

The displacement parameter plays an important role in the computation of GLCM. Applying a large displacement to a fine texture would yield a co-occurrence matrix that does not capture the textural information (Soh and Tsatsoulis 1999). High displacement values (above 10) result in decreasing the classification accuracy. Barber and LeDrew

(1991) demonstrated that a displacement value of 1 produced superior classification results when compared to displacement values of 5 and 10. Also, Shokr (1991) after experimenting with different δ values concluded that δ=2 is the most appropriate.

6.2.1.3 Quantization

The number of quantization levels is one of the most important factors in the computation of GLCM. The decision that we have to make is how many levels are needed to represent a set of textures successfully (Soh and Tsatsoulis 1999). The higher the number of gray levels involved in the computation, the more accurate the textural information. If the number of quantized levels is too high (over 64), this leads to an increase in computational cost since the dimensions of GLCM matrix is indicated by the number of gray levels. On the other hand, using a low number of gray level values (below 8), the texture information of a SAR image is reduced but it accelerates the computation of co-occurrence texture features. It is expected that coarser quantization would reduce both classification accuracy and seperability of the sea ice classes (Clausi, 2002). On the other hand, finer resolution increases both the accuracy and seperability of sea ice classes.

6.2.1.4 Window size

The computational window is effectively a sub-image of the SAR imagery moving across the image calculating the co-occurrence matrix.

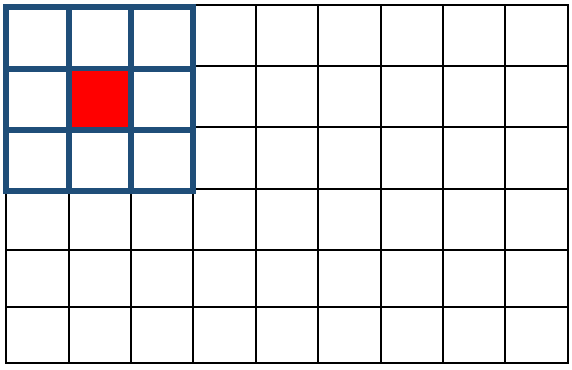

Figure 6.1. Computational window size. The cell in red receives the value of the calculations

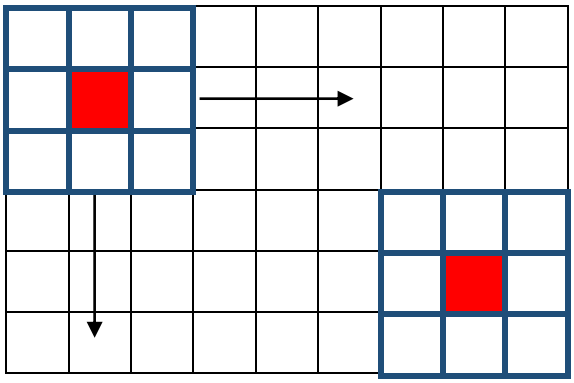

Figure 6.2. A moving computational window

In texture analysis, it is important that the textural features of the various class types need to be extracted over a local area of unknown size and shape (Pathak and Dikshit 2010). If the areas are not large enough with respect to the texture element, then one cannot expect these local analysis to provide feature values that are invariant across the textured region (Pathak and Dikshit 2010). Hence, it is preferable the texture information to be extracted over a large area. Existing studies suggest that large window sizes (11 x 11, 13 x 13 or even larger) provide better results in sea ice class seperability (Pathak and Dikshit 2010, OTUKEI, et al 2012). Window size is crucial parameter for image segmentation and classification where large window sizes have higher possibilities of overlapping more than 2 classes. One cannot ensure that the window size selected will not overlap more than 2 classes. If this is the case, then the features would be representing a hybrid value and this leads to the so-called window effect (Pathak and Dikshit 2010). This situation usually occurs for linear features where its spatial extent is smaller than the window size (ridge or leads) and at the boundaries of classes.

6.2.2 GLCM computation

For the calculation of GLCM matrix, fourteen texture features have been defined by Haralick (Haralick and Shanmugam, 1973) to extract characteristics of texture statistics of remote sensing imageries. For the classification of remotely sensed data, eight texture

features out of fourteen are usually used. It is worth mentioning that some features are correlated to each other, hence, a careful analysis on the feature selection should be carried out. Below, figure 6.3 and figure 6.4 illustrate the construction of the GLCM matrix. Consider a gray tine image with a size of 4 x 4 pixels (figure 7.3).

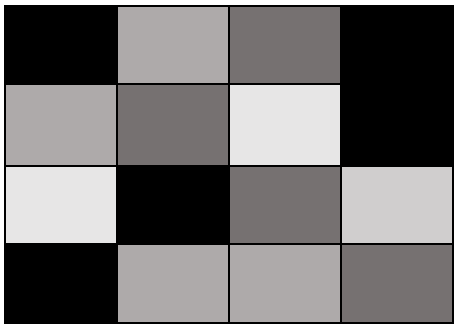

(a)

0	2	1	0
2	1	3	0
3	0	1	2
0	2	2	1

(b)

Figure 6.3: Matrix 4 x 4 pixels. (a) Shows an image with 3 quantized gray tones and (b) illustrates the corresponding pixel values of the image.

From the image above, GLCM matrix can be obtained as follows.

0	2	1	0
2	1	3	0
3	0	1	2
0	2	2	1

(a)

n/bor / **ref**	**0**	**1**	**2**	**3**
0	0	1	1	0
1	1	0	1	1
2	0	2	0	0
3	2	0	0	0

(b)

0	0.111	0.111	0
0.111	0	0.111	0.111
0	0.222	0	0
0.222	0	0	0

(c)

Figure 6.4. GLCM computation. (a) Initial image, (b) GLCM computation and (c) Normalized GLCM

The dimensions of GLCM depend on the number of gray level of the initial image. In the example above, four gray levels are shown in the image, hence, the dimensions of GLCM will be 4 x 4 as shown in the figure 6.4b. The top row and the column at the far left of the figure 7.4b illustrates the quantized gray levels of the initial image. In this example, $\delta = 1$ and $\theta = 0^o$ are chosen for the computation of GLCM. The number 2 in figure 7.4b represents the frequency of the pixel pair values 2 and 1in the initial image. Finally, the GLCM matrix should be normalized (figure 6.4c) by dividing each value of P_{ij} with the total gray level values in the GLCM matrix. As it was mentioned above, fourteen texture features have been developed to describe the properties of an image, but only the most important ones that are used for classifying remotely sensed data will be mentioned in this study. These texture features are described below.

1. **Mean**

$$\sum_{I,J=1}^{G} i(P_{i,j}) \qquad 7.3$$

The GLCM mean refers to how many times the reference pixel value occurs in combination with the neighbor pixel. The GLCM mean feature is considered one of the best features for discriminating different sea ice types.

2. **Variance**

$$\sum_{i,j=0}^{G} P_{i,j}(i - \mu_i)^2 \qquad 7.4$$

Variance is a measure of the dispersion of the values around the mean of combinations of reference and neighbor pixels (Patrola 2013). GLCM variance is strongly correlated to the first order statistics. This statistic is a measure of heterogeneity and increases when the quantized gray level values differ from the mean.

3. Correlation

$$\sum_{i,j=0}^{G} \frac{(\mathrm{i} - \mu_i)(\mathrm{j} - \mu_j)\, \mathrm{P}_{ij}}{\sqrt{\sigma_i^2\, \sigma_j^2}} \qquad 7.5$$

Correlation expresses linear dependency between the gray tones within the image (Haralick and Shanmugam 1973). High values (close to 1) indicate a linear dependency between the brightness levels of pixels in the computation window and can be obtained for similar gray level regions (Zakhvatkina et.al 2016). Hence, the correlation increases when there are uniform surface on the image such as smooth first year ice.

4. Angular Second Moment (ASM)

$$\sum_{i,j=0}^{G} (P_{ij})^2 \qquad 7.6$$

ASM increases when there are uniform surfaces in the SAR image. When features in the image have similar gray level values, then energy increases. On the other hand, ASM decreases when there is a lot variation in a SAR image. For instance, for non-structured areas such as calm waters, energy receives high values (close to 1).

5. Energy

$$\text{Energy} = \sqrt{ASM} \qquad 7.7$$

Energy behaves the same as ASM. In uniform areas, ASM produces high values and low values for areas with a lot of variation

6. Entropy

$$\sum_{ij=0}^{G} P_{ij}\ (logP_{ij}) \qquad 7.8$$

Entropy measures the disorder in an image and assigns high values to the pixels with random gray tones. The entropy increases with low variability in the computation area of radar image and indicates a random mixture of scattering mechanisms (Zakhvatkina et.al 2016). Hence, high values in a SAR image could indicate sea ice deformation or ice edge which create strong reflections. Inhomogeneous areas will also produce enhanced values, due to intensity differences in the mixture components, even when the radar reflections are not strong (Zakhvatkina et.al 2016).

7. Contrast

$$\sum_{ij=0}^{G} P_{ij}\ (i-j)^2 \qquad 7.9$$

Contrast is a measure of local variation in the SAR image (a number of pixels pairs have different brightness values). If the SAR image has more heterogeneous texture character and if there is a large amount of brightness variations, contrast has higher significance that makes objects distinguishable (Zakhvatkina et.al 2016). In case of SAR image, the border between a sea ice floe and open water has the highest values.

8. Dissimilarity

$$\sum_{ij=0}^{G} P_{ij}\ (i-j) \qquad 7.10$$

Dissimilarity measures the difference between pixel pairs in the image and assigns high values to features with high contrast. Hence, dissimilarity and contrast texture features are strongly correlated.

9. Homogeneity

$$\sum_{ij=0}^{G} \frac{P_{ij}}{1 + (i - j)^2} \qquad 7.11$$

Homogeneity is a measure of uniformity and assigns high values to the areas with the lowest contrast. Calm waters or young ice have high values due to their homogenous surface.

The results of GLCM matrix depends on a few factors such as Gray level values (G), window size, orientation (θ) and the distance (δ). In order to achieve good classification results, experimentation with the aforementioned parameters should be carried out in order to choose the most appropriate values.

7 Supervised classification

7.1 Introduction

For classifying a SAR image, a classifier is needed where associates each pixel of the image with a class (this class can be labeled as Multi-year ice, young ice, water, etc.). The classification methods can be categorized in un-supervised and supervised. In the literature, there are numerous studies conducted using both supervised and unsupervised techniques for sea ice classification.

In terms of unsupervised classification method, the computer learn how to perform the classification without prior knowledge or inputs from the user. The algorithm tries to group all pixels in the image with similar spectral values (standard deviation, mean) into unique clusters. ISODATA and K-means clustering are some of the widely used techniques for un-supervised classification. This classification methods usually produces poor results due to the lack of information about the area in which the classification will be performed. Without prior knowledge about the scene, the algorithm has to decide how to assign the pixels of the image into different classes. The un-supervised method is time consuming and is insensitive to the variations of the spectral signatures of different features. For instance, if two or more features have similar spectral signature then the probability of pixel miss-classification is high.

On the other hand, supervised classification is the most common method in classification problems because it is more accurate than the unsupervised method but it heavily depends on training data. The user defines the number of classes that will be used and is responsible for specifying the pixel values of the image that should be associated with each class. Supervised classifiers such as maximum likelihood classifier, minimum distance classification and Neural Networks have been extensively studied in sea ice classification.

The maximum likelihood classifier has been the most popular method of classification in remote sensing (Japan Association of Remote Sensing 1999). In order for this method to work, sufficient number of ground truth data is required. Also, the inverse matrix of the

variance-covariance matrix becomes unstable in the case where there is a high correlation between two bands (Japan Association of Remote Sensing 1999). Finally, if the distribution of population does not follow a normal distribution, the maximum likelihood method cannot be applied (Japan Association of Remote Sensing 1999).

Minimum distance classifier is a simple method and faster than the maximum likelihood. Due to the fact that it does not use covariance data, it is not as flexible and cannot be used to model complex data.

Neural Networks (NN) has been a very popular technique (the last two decades) for sea ice classification in SAR images. This classification technique outperforms the other classification methods described above. It has proven to be useful in the past but is slowly losing popularity and is showing a trend of being taken over by the Support Vector Machine (SVM) (Satyanarayana and Anuradha 2013).

7.2 Supervised learning

In order to perform supervised learning, we need to provide the algorithm with some labeled data (training data) and tune its parameters so that it works well for unseen datasets. The first step in supervised classification is the collection of the training samples. Say for example, we need to perform a supervised classification for identifying different sea ice types. In order to construct the training samples, we need to collect a number of samples for each sea ice type shown in the image. These samples are just blocks of pixels. In order for the algorithm to perform well, a good set of features is required. One feature that we could use is the intensity values of the pixels. It is important to provide the algorithm with a good set of features for better performance.

We may have n models and we want to select the one that performs best through training and validation process. The performance of the model is evaluated on different dataset (data that has not seen before). Hence, supervised learning can be divided into training, testing and validation algorithms.

7.2.1 The concept of training, validating and testing the classifier

First of all, the classifier should be trained first before making predictions. In the training process, the algorithm chooses the best parameters using labeled datasets. These labeled datasets are called training data. What we are interested in is the performance of the model on the new data and not the performance on the old data (where the training process takes place).In order to predict the performance of a classifier on new data, we need to assess its error rate on a dataset that played no part in the formation of the classifier (Witten et.al 2016). This dataset is called the test data. We assume that both the training and test data are representative samples of the underlying problem (Witten et.al 2016).

Secondly, after the training process is completed, we use validation data for tuning the parameters of the model to perform better in unseen data and to avoid overfitting.

Finally, test data are provided to the classifier to do the final classification and evaluate its performance. One important parameter is that the test data has not been used to train the classifier.

7.3 Support Vector Machine classifier

In this chapter, the support vector machine (SVM) classifier will be discussed. SVM is a supervised classifier and it was developed in 1990s. Since then, it has grown rapidly in popularity since high resolution satellite data was available. The use of high quality data for a classification problem is very important in order to appreciate the effectiveness of a supervised classifier. SVM is the newer trend in machine learning algorithm which is popular in many pattern recognition problems in recent years, including texture classification (Satyanarayana and Anuradha 2013). SVM is considered one of the most powerful classifier which have shown to outperform well established classification methods such as NN and has slowly evolved into one of the most important main stream classifier (Satyanarayana and Anuradha 2013). Due to its popularity as a classification

methods, it has recently been applied to SAR image for sea ice classification producing very good results.

The SVM classifier was first developed for binary classification and it was extended to support more than two classes. We can divide the SVM into linear and non-linear models. If data can be divided linearly be using a straight line then this called a linear classification. On the other hand, if data cannot be divided with a straight line then more complex models can be used (non-linear models). In this case we perform a classification using non-linear model.

In this chapter we will introduce to SVM binary classification, the maximal margin classifier and its extension to a multi-class classification.

7.3.1 Classification using a separating hyperplane

In this chapter, we will introduce the concept of the optimal separating hyperplane. In a p dimensional space, a hyperplane is a flat affine subspace of dimension p – 1^1(James et.al 2013). If the data is in two dimensions then the dimensions of the hyperplane is one (a line). Hence, in three dimensions, the hyperplane is a two dimensional subspace.

The mathematical definition of a hyperplane in two dimensions is given below.

$$\beta_0 + \beta_1 X_1 + \beta_2 X_2 = 0 \qquad 7.1$$

for parameters $\beta_0, \beta_1 \; and \; \beta_2$. If a point X = $(X_1 , \; X_2)^T$ on the hyperplane satisfies (8.1), the X lies on the hyperplane. Equation 7.1 can be extended into p dimensions as follows.

$$\beta_0 + \beta_1 X_1 + \beta_2 X_2 + \ldots + \beta_p X_p = 0 \qquad 7.2$$

Now, consider the case where X does not satisfy (7.2); rather

$$\beta_0 + \beta_1 X_1 + \beta_2 X_2 + \ldots + \beta_p X_p > 0 \qquad 7.3$$

Then, the equation tells us that X lies on the one side of the hyperplane. Conversely, if

$$\beta_0 + \beta_1 X_1 + \beta_2 X_2 + \ldots\ldots + \beta_p X_p < 0\,, \qquad 7.4$$

then, X lies on the other side of the hyperplane.

Another mathematical definition that describes the hyperplane that can be found in the literature is the following.

$$y = w^T \cdot x + b, \qquad 7.5$$

where,

w is the weight vector

x is the input vector

b is the bias weight

Note that $w^T \cdot x$ is the inner product. In other words, $w^T \cdot x = \sum_1 w_i\, x_i$

Hence, any point x where w^T x + b > 0, it lies on the one side of the hyperplane. If any point x where w^T x + b < 0, it lies on the other side of the hyperplane.

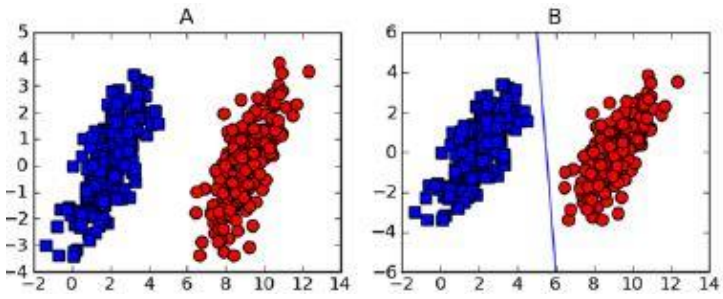

Figure 7.0. A hyperplane. (A) Shows two classes to be classified and (B) shows the hyperplane separating the two classes (Harrington 2012)

Now, consider the case where we have a matrix X that consists of a number of training observations ($x_1 \ldots\ldots x_n$) in p dimensional space and these training observations fall into

two classes. Also, we have test data ($y_1 \ldots\ldots y_2$) to be used for the classification. The goal is to construct a classifier based on the training data that will correctly classify the test observations. Figure 7.1 illustrates the classification of the test data.

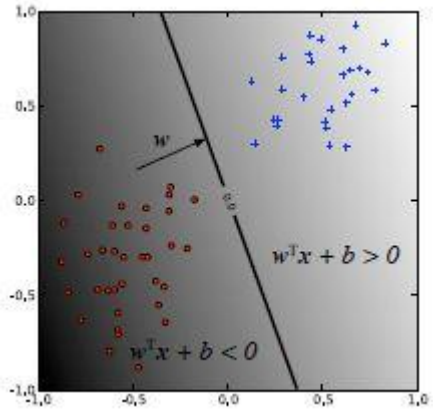

Figure 7.1. Classification of test observations. The separating hyperplane (w^T · x + b = 0) divides the two datasets depending on the sign of w^T · x + b (Ben-Hur and Weston 2010).

The test data shown in figure 7.2 has been classified according to the sign. If the sign is positive, then the point (x) is classified as blue and if the sign is negative, then the point (x) is classified as red. If point x is far from zero, then that means that x lies away from the hyperplane and we can be confident that this point has been classified correctly. Conversely, if point x is close to zero, that means that x lies close to the hyperplane, and we feel less confident about the assignment of x to a particular class.

7.3.2 Maximal margin classifier

The Support Vector Machine (SVM) is a generalization of a simple an intuitive classifier called maximal margin classifier (James et.al 2013). Unfortunately, the maximal margine classifier cannot be applied on complex datasets as it requires the different classes be separable by a linear boundary. Due to of this limitation, an extension of maximal margin

classifier called support vector machine classifier which can accommodate non-linear class boundaries, it will be introduced in chapter 7.3.5.

As we can see in figure 7.1, we can fit more than one hyperplane to separate the two classes. In fact, an infinite number of hyperplanes can be used to separate the two classes. Hence, the question which is raised is which of the infinite possible hyperplanes to use.

A natural choice is the maximal margin hyperplane (also known as the optimal separating hyperplane), which is the separating hyperplane that is farthest from the training observations (James et.al 2013). Hence, we compute the distance from each point to a given hyperplane and the distance that is the smallest is known as the margin. The maximal margin hyperplane is the separating hyperplane for which the margin is largest – that is the hyperplane that has the farthest minimum distance to the training observations (James et.al 2013). Hence, each point can be classified on which side of the maximal margin hyperplane it lies. This is the maximal margin classfier. What we want is a classifier that has a large margin on both training and test dataset in order to correctly classify the test data. Training data is the data we have used to identify the separating hyperplane. The algorithm is trying to learn these data and evaluate its performance on the test data.

Figure 7.2 illustrates the maximal margin hyperplane between the two classes.

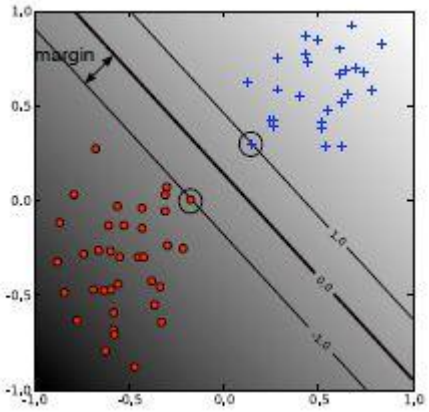

Figure 7.2. Maximal margin hyperplane. The circled points are the support vectors and they determine the margin between the two classes (Ben-Hur and Weston 2010).

It can be observed in figure 7.3 that there are two points inside the black circles either side of the hyperplane. These two points are knows as support vectors and they 'support' the maximal margin hyperplane in the sense that if these points were moved slightly then the maximal margin hyperplane would move as well (James et.al 2013). It can been seen that the maximal margin hyperplane depends on the support vectors and not on the other points. Hence, a movement of the other observations would not affect the hyperplane.

We have described above the concept of maximal margin classifier and now we can describe it mathematically as shown below.

$$\mathrm{M} = \frac{1}{2\,|w|} = \frac{1}{2\sqrt{w^2}} \qquad 7.6$$

Now, given a classification boundary (a vector w and a scalar b that defines the line $w^T \cdot$ x + b) the margin M can be computed. So, what we want is to find those values for w and b that maximizes the margin M. Equation 8.6 tells us that in order to make the margin as large as possible, we need to make w^2 as small as possible. This would be an easy problem if the minimization of w^2 was the only constrain. We would set w = 0 and the problem would be solved. Apart from making w as small as possible, we also need a hyperplane that can separate the two classes and act as a classifier. Hence, two problems must be satisfied. Minimizing w and find a classification boundary that can classify well. This leads to the following constrain.

$$\underset{w,b}{Minimize} \quad \frac{1}{2}\,|w|^2 \qquad 7.7$$

$$\text{Subject to } y_i(w^T \cdot \mathrm{x} + \mathrm{b}) \geq 1 \qquad i = 1 \ldots . n \qquad 7.8$$

The constraint in this formulation ensure that the maximum margin classifier classifies each example correctly, which is possible since we assume that the data is linearly

separable (Ben-Hur and Weston 2010). The equation above is an optimization problem where its solution will give us the optimum margin classifier.

7.3.3 The non-separable case

In the previous chapter we discussed the case where data can be linearly separated. However, most of the times, due to data complexity, no separating hyperplanes exist and hence, there is no maximal margin classifier. In this case, we cannot apply the optimization problem. An example of a non-separable case is shown in figure 7.3.

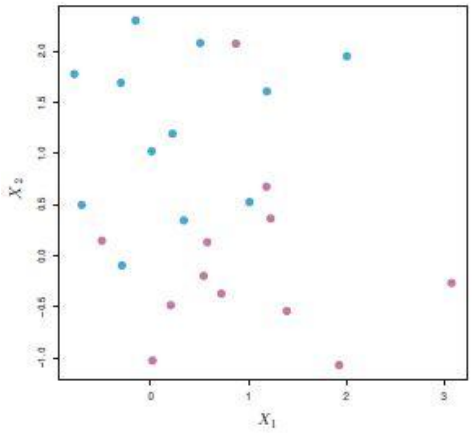

Figure 7.3. Two classes are shown in blue and purple. In this case, these two classes cannot be separated using a linear boundary (James et.al 2013)

In the next chapter we will see how we can develop a hyperplane that separates the two classes using soft margin. This is known as support vector classifier

7.3.4 Support Vector Classifier

In figure 8.4 we can see that the observations are not separable by a hyperplane. If we tried to fit a linear boundary in those data, the misclassification error would be very large and we would be able to find a desirable hyperplane. The maximal margin hyperplane is extremely sensitive to a change in a single observation which suggests that it may have

overfit the training data (James et.al 2013). In this case, we can construct a hyperplane that does not perfectly separate the two classes in favor of performing better classification of most of the test data.

The support vector classifier (soft margin) rather than seeking the largest possible margin so that every observation is not only on the correct side of the hyperplane but also on the correct side of the margin, we instead allow some observations to be on the incorrect side of the margin, or even on the incorrect side of the hyperplane (James et.al 2013). An example is shown in figure 7.4.

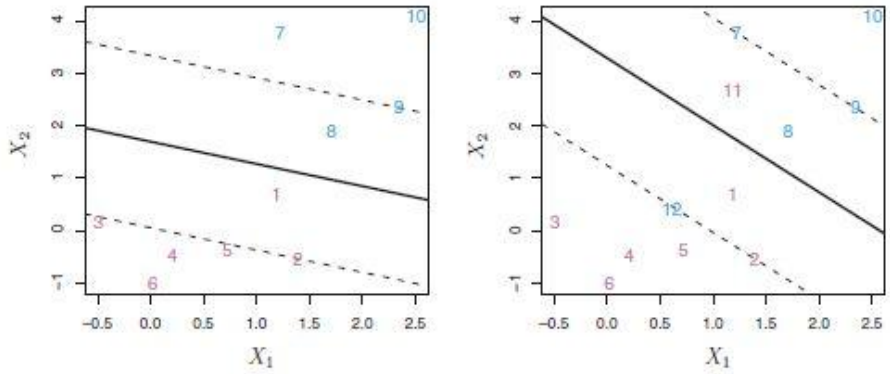

Figure 7.4. On the left, support vector classifier separates the two classes. Points 3, 4, 5 and 6 are on the correct side of the margin while the point 2 sits exactly on the margin and the point one is on the wrong side of the margin. For the blue points, the point 9 is on the margin and the point 8 is located on the wrong side of the margin. On the right, points 11 and 12 are on the wrong side of the margin and on the wrong side of the hyperplane (James et.al 2013).

The support vector classifier can handle data that cannot be separated with a linear boundary by introducing a slack variable ξ_i that relax the constraints in (8.7). $\xi_1 \ldots . \xi_n$, are called slack variables because they allow some points to be on the wrong side of the margin or the hyperplane. Hence, to allow errors, the equation (7.7) becomes

$$y_i(w^T \cdot \mathrm{x} + \mathrm{b}) \geq 1 - \xi_i \qquad i = 1 \ldots . n \tag{7.9}$$

Where $\xi_1 \geq 0$ is the slack variable as we mentioned before. If $\xi_1 = 0$, then the ith point is located on the correct side of the margin. If $\xi_1 > 0$, then the ith point is on the wrong side of the margin and this means that this point has violated the margin. On the other hand,$\xi_1 > 1$ then the point is on the wrong side of the hyperplane. Now, the optimization problem becomes

$$\underset{w,b}{Minimize} \qquad \frac{1}{2} |w|^2 + \mathrm{C} \sum_{i=1}^{n} \xi_i \tag{7.10}$$

$$\text{Subject to } y_i(w^T \cdot \mathrm{x} + \mathrm{b}) \geq 1 - \xi_i \,, \quad \xi_i \geq 0 \tag{7.11}$$

$$\xi_i > 0, \qquad \sum_{i=1}^{n} \xi_i \leq C \tag{7.12}$$

The constant C > 0 is a tuning hyperparameter that specifies the misclassification penalty and it can be tuned by the user. Hyperparameter C calculates the sum of $\xi_i's$ and it determines the number of points that violated the margin (and to the hyperplane). If C =0 then there are no violations which means that $\xi_i \ldots\ldots \xi_n$ =0. For C > 0 no more than C observations can be on the wrong side of the hyperplane, because of an observation is on the wrong side of the hyperplane then $\xi_i > 1$, and (8.12) require that $\sum_{i=1}^{n} \xi_i \leq C$ (James et.al 2013). For large values of C, the margin narrows and we do not allow many violations. On the other hand, as C decreases, the margin widens and we allow more violations to the margin. The role of C parameter is illustrated in figure 7.5. The hyperparameter C also controls the bias-variance trade off of our model (models with high bias are prone to errors and fail to capture the complexity of the data. Models with high variance tend to overfit the data and the model is unable correctly classify the observations). When a user chooses a large value for C, this means that the margin narrows and the classifier fits the data very well. This leads to a classifier which has low bias but

high variance. On the other hand, if a user chooses a small value for C, the margin widens and we allow more violations. Such a model does not fit the data very well so, it is more biased but may have lower variance.

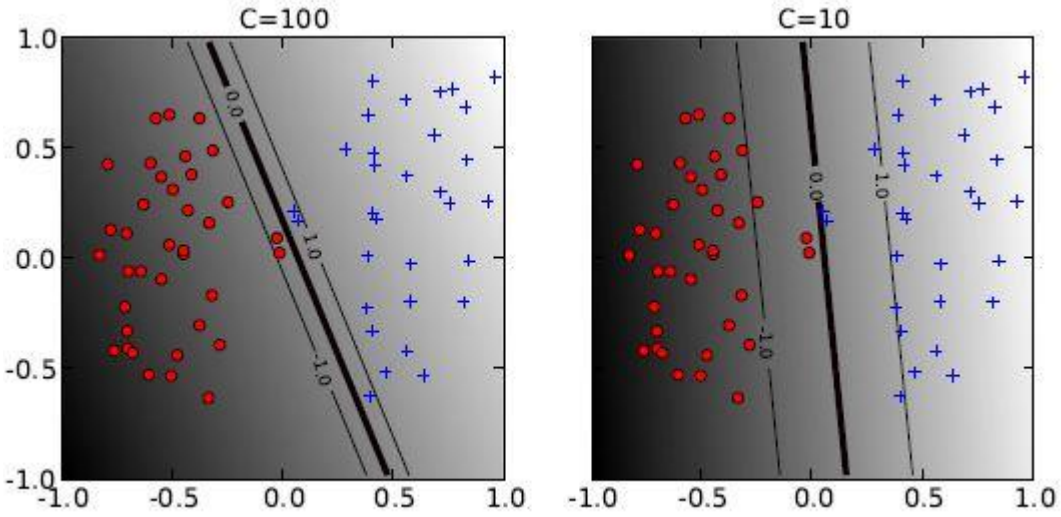

Figure 7.5. The effect of C value to the decision boundary. On the left, C value was increased to 100 resulting in a very narrow margin where only a few points violated the margin. On the right, the C value was decreased to 10 resulting in a wider margin with more violations (Ben-Hur and Weston 2010).

7.3.5 The support vector machine

Until now, we have discussed about data classification using a linear decision boundary. There are cases where linear boundary cannot be used to separate two classes because the data might be too complex. Hence, another way should be found to map the data complexity. Support Vector Machine (SVM) classifier is the solution to that. SVM is an extension of support vector classifier that results from enlarging the feature space using kernels in order to accommodate a non-linear boundary between two classes (James et.al 2013).

Kernel parameters affect the decision boundary significantly. The degree of the polynomial kernel controls the flexibility of the classifier. The linear kernel, as we can see in figure 7.6 is not sufficient for separating the two classes. As the polynomial degree increases, the flexibility of the decision boundary increases which allows the discrimination of the two classes.

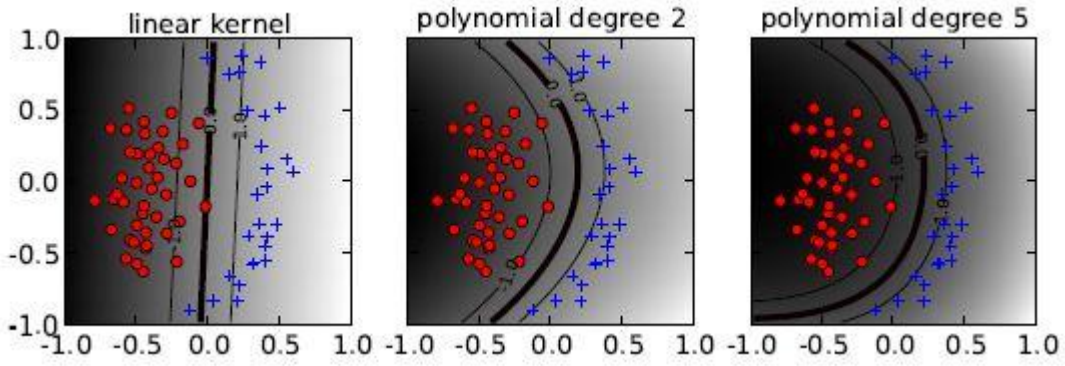

Figure 7.6. How the polynomial degree affects the decision boundary. The higher the polynomial degree, the more flexible the decision boundary is going to be (Ben-Hur and Weston 2010).

There are four kernels we can choose from for classifying the data. These kernels are, linear kernel, polynomial kernel, Radial Basis Function (RBF) kernel and sigmoid kernel. A question that is posed is which of these kernel a user should choose to classify the data. An experimentation with different kernels should be conducted first before deciding which kernel to use. Users can try a linear kernel first and then the model can be improved by using a non-linear kernel. The mathematic description of kernels is given below.

- Linear kernel

$$K(x_i\, x_j) = x_i^T\, x_j \qquad 7.13$$

K is some function which is referred to as kernel. Linear kernel is the simplest model that can be used by SVM but it fails when the data are not linearly separable.

- Polynomial kernel

$$K(x_i\, x_j) = (\gamma x_i^T\, x_j + r)^d\ ,\ \gamma > 0 \qquad 7.14$$

This is a polynomial kernel of degree d, where d is an integer number. By using a kernel with d > 1, this leads to an algorithm with more flexible decision boundary.

- Sigmoid kernel

$$K(x_i\, x_j) = \tanh(\gamma x_i^T\, x_j + r) \qquad 7.15$$

The sigmoid kernel is very popular because it comes from Neural Network. It is interesting to note that an SVM model using a sigmoid kernel function is equivalent to a two layer perception Neural Network (Ahuja and Yadav).

- Radial Basis Function (RBF)

$$K(x_i\, x_j) = \exp(-\gamma \left\| x_i - x_j \right\|^2),\ \gamma > 0 \qquad 7.16$$

RBF is another popular kernel that is used for classifying complex dataset (figure 7.7 illustrates how RBF kernel works). The RBF kernel works as follows. Given some test data x^* = (x_1^*…….x_p^*) and some training data x = (x_1…....x_p), if x^* is far from a training point x (in terms of Euclidian distance) then $\left| x_i - x_j \right|^2$ will be large and $K(x_i\, x_j)$ =

$\exp(-\gamma\|x_i - x_j\|^2)$ will be very small. In other words, if a training observation x_i is far away from a test observation x^*, it will play no role in predicting the class label for x^*.

Note that all the kernels above apart from the linear kernel have the parameters r and γ. These parameters can be used to tune the model during the training phase for higher performance. The hyperparameter γ is critical for the performance of the model. The γ parameter defines the influence that each observations has. When γ value increases, the locality of the support vector expansion increases, leading to greater curvature of the decision boundary (Ben-Hur and Weston 2010). If this value is too high then the model will overfit the data.

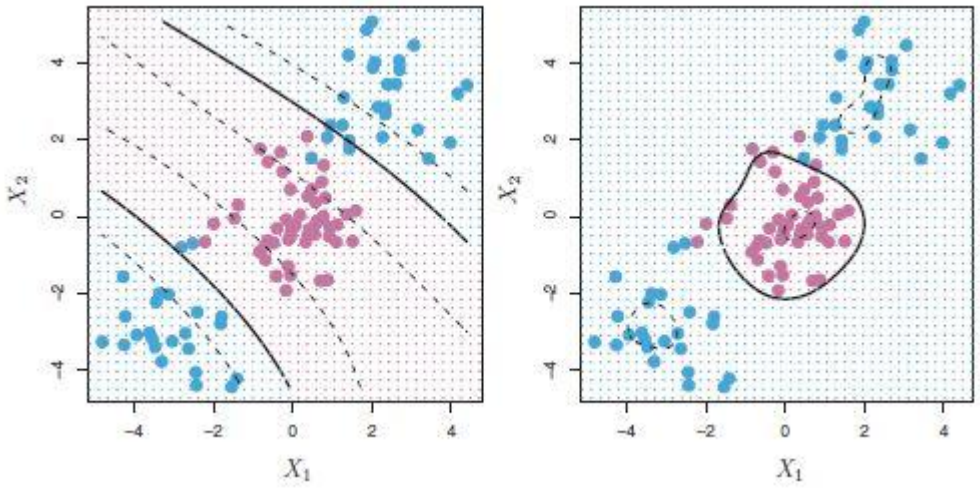

Figure 7.7. On the left, a 3rd degree polynomial kernel is illustrated. On the right, an RBF kernel has been applied (James et.al 2013)

7.3.6 Multi-class SVM

SVM classifier was originally developed for binary classification (k=2). However, real world data is more complex and requires the separation for more than 2 classes. Hence, as an extension to the binary classification, two methods for multi-class SVM have been developed. These methods are one-against-one and one-against-all. A potential problem with one-against-all is that when the number of classes is large, each binary classification becomes highly unbalanced (Xue and Wang 2014). The unbalanced classification problem can occur when the number of samples of some classes is much higher than other classes. In this case, most of the classifiers ignore the classes with a small number of samples and focus on the classes with the high number of samples. SVM can be more accurate on unbalanced data since only the support vectors (observations located on the margin) are used for classification while observations far from the hyperplane do not play a role. Below, the mathematical explanation for the two approaches of multi-class problem is given.

- <u>One versus all</u>

One versus all is the earliest method that has been used for SVM multi-class classification problems. This method constructs k binary classifiers (k is the number of classes) for k classes. The m-th binary classifier is trained using the data from the m-th classas positive examples and the remaining k-1 classes as negative results and the class label is determined by the binary classifier that gives maximum output value (Xue and Wang 2014) .Given some training data (x_i, y_i, ……,(x_n, y_n), where i = 1…….n and the classes for each x_i, we need to solve the following problem.

$$\begin{aligned} \min_{w,b,\xi} \quad & \frac{1}{2}(w^m)^T w^m + \mathrm{C}\sum_{i=1}^{l}\xi_i^m \\ & (w^m)^T \Phi(x_i) + b^m \geq 1 - \xi_i^m \text{ , if } y_i = \mathrm{m}, \\ & (w^m)^T \Phi(x_i) + \leq -1 + \xi_i^m \text{ , if } y_i \neq \mathrm{m}, \\ & \xi_i^m \geq 0 \text{ , } \mathrm{i}=1,\ldots\ldots,\mathrm{l} \end{aligned} \qquad 7.17$$

C parameter, as we have seen in previous chapters is the penalty parameter and Φ denotes the higher dimensional space. $\frac{1}{2}(w^m)^T$, means that we want to maximize $\frac{2}{\|w^m\|}$ which is the margin between the classes. There is a penalty term C $\sum_{i=1}^{l} \xi_i^m$ for the data that are not linearly separable which reduces the training errors. What we are looking for is a balance between $\frac{1}{2}(w^m)^T w^m$ and the training errors.

- <u>One versus one</u>

One versus one is another method for multi-class classification for SVM. It evaluates all possible pairwise classifiers and thus induces k(k-1)/2 individual binary classifiers (Xue and Wang 2014). Each classifier is applied to test observations and gives one vote to the winning class. A test observation is assigned to a class with the highest number of votes. This problem can be solved as follows.

$$\min_{w^{ij},\, b^{ij},\, \xi^{ij}} \quad \frac{1}{2}(w^{ij})^T w^{ij} + C \sum_{i=1}^{l} \xi_i^{ij}$$

$$(w^{ij})^T \Phi(x_i) + b^{ij} \geq 1 - \xi_i^{ij} \text{ , if } y_i = i,$$

$$(w^{ij})^T \Phi(x_i) + \leq -1 + \xi_i^{ij} \text{ , if } y_i = j, \qquad 7.18$$

$$\xi_i^{ij} \geq 0$$

The approach with voting described above is all called ‘max wins’ strategy. The only issue with this method is when there is a case where two classes might have identical votes, in this case, ‘max wins’ strategy might not work well in classifying the two classes.

8 Results and discussion

8.1 SAR data pre-processing

In this chapter, the pre-processing of SAR images are illustrated. All pre-processing steps were performed on SNAP toolbox

8.1.1 Noise floor reduction

The Extra Wide Swath (EW) SAR data are contaminated with noise which appears as bright stripes along the SAR image. Thermal noise suppression has not been applied to SENTINEL-1 data, hence, noise reduction is crucial for better discrimination of sea ice types. Image de-noising has been applied to both SAR scenes as shown below.

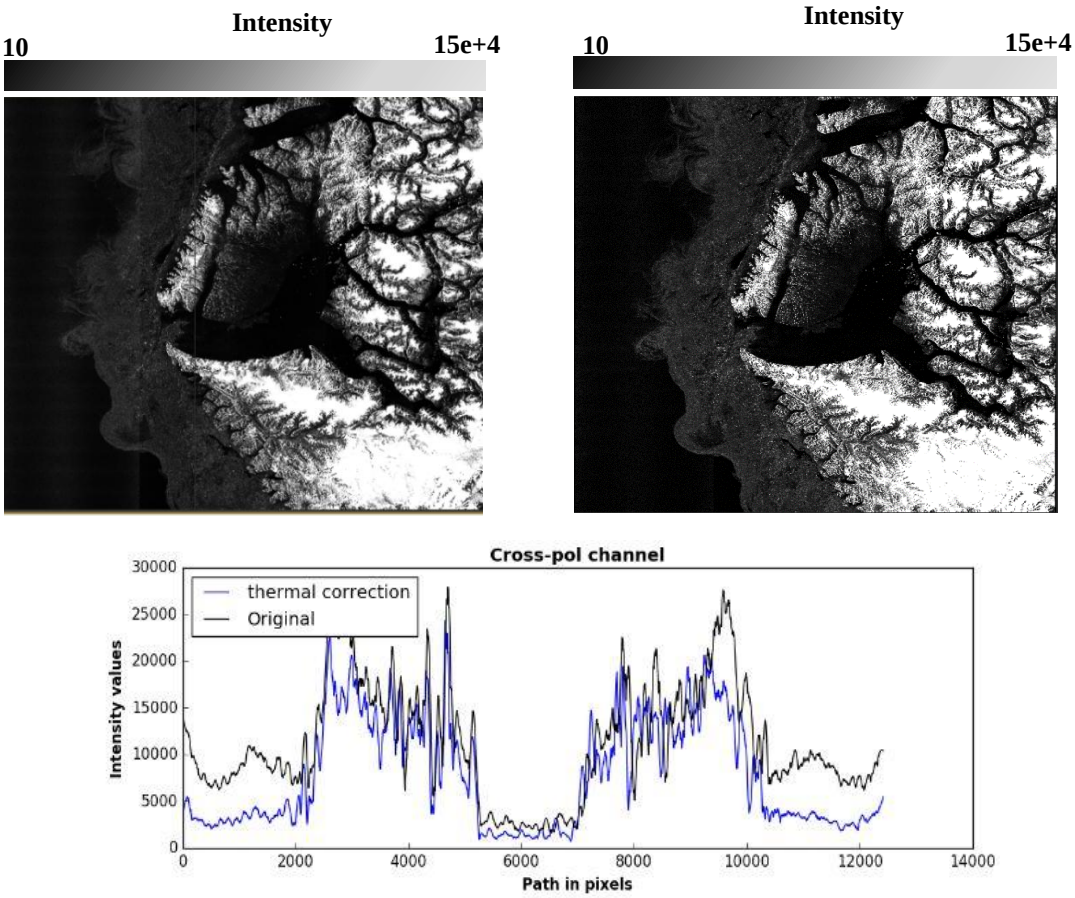

Figure 8.0: SAR cross-polarized images captured in February 23 of 2016. On the left image, the presence of thermal noise is obvious. On the right, the bright stripe is no longer there after the thermal noise correction. The graph shows the intensity values before and after the thermal noise reduction

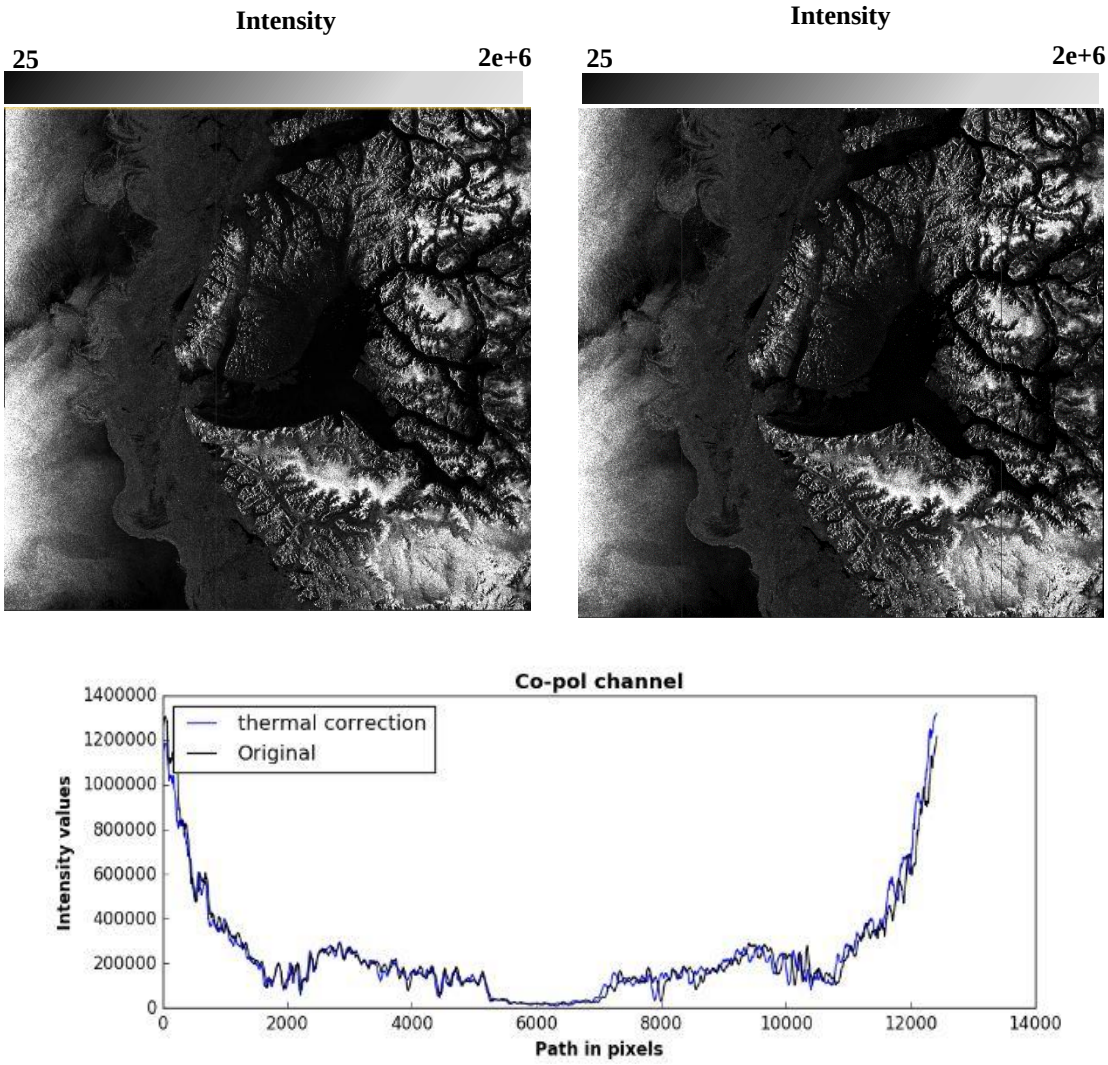

Figure 8.1: SAR co-polarized images captured in February 23 of 2016. On the left, the SAR image before thermal noise correction is shown. On the right, the de-noised image is depicted. As it can be noticed, the HH polarization is not affected by thermal noise. The graph shows the intensity values before and after the thermal correction where they overlap.

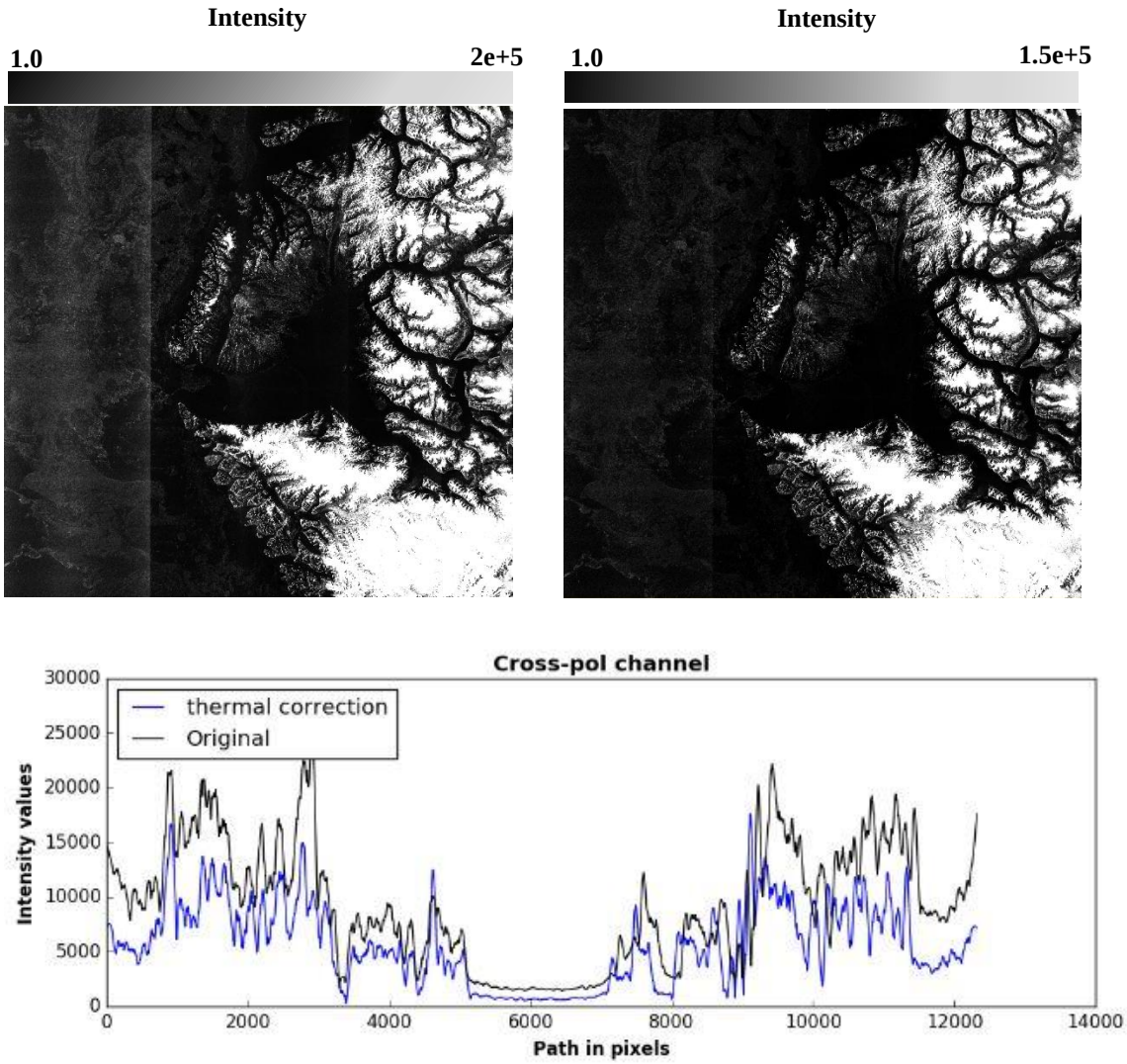

Figure 8.2: SAR cross-polarized images captured in May 29 of 2016. On the left, the presence of thermal noise is illustrated. On the right, the de-noised image is shown. On the bottom, the graph shows the intensity values before and after the thermal correction

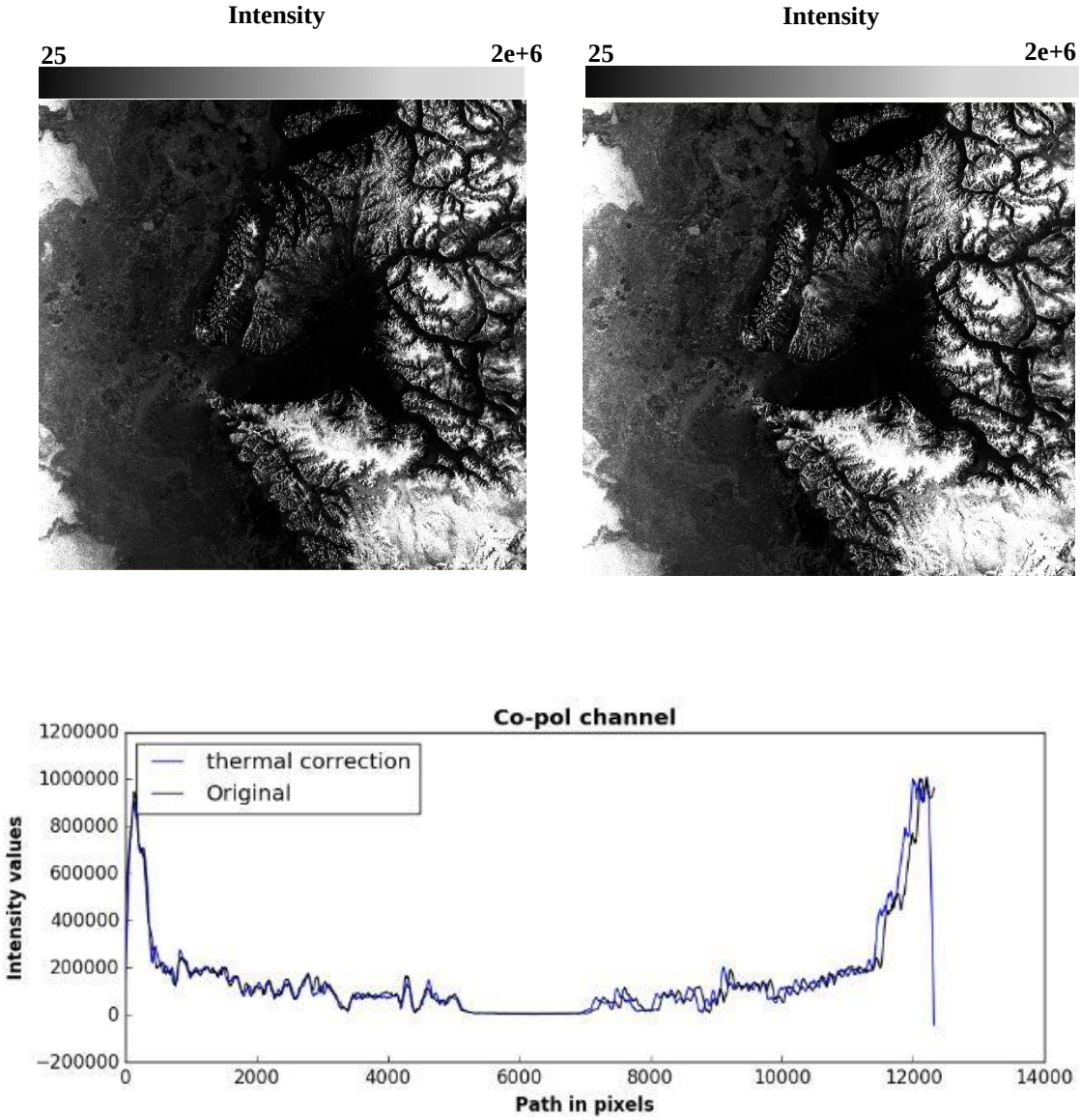

Figure 8.3: SAR co-polarized images captured in May 29 of 2016. On the left, the presence of thermal noise is illustrated, while on the right we have the de-noised image is. The values of the image before thermal noise correction and the values of de-noised image overlap. This is because HH polarization channel is not affected by thermal noise. On the bottom, the graph shows the intensity values before and after the thermal correction

The presence of noise (no signal is returned to the sensor) on the cross-polarized images is obvious in both datasets. After thermal noise reduction, the bright stripe has been removed improving the image quality. For the SAR scene acquired in May 2016, we notice that after image de-noising some residuals were left in the SAR image. The reason for this is that this SAR scene is severely affected by thermal noise due to the extremely low backscatter energy (<29 dB).

Apart from visual inspection, graphs have also been created (taking a cross section along the image) showing the different before and after thermal noise reduction. The plotted black line shows the intensity values before thermal correction was applied and the line in blue shows the intensity values of the image after thermal noise correction was applied. It can be clearly seen the drop of the intensity values (blue line) after the thermal noise was removed.

On the other hand, the SAR images in co-polarization channel has not been affected by the thermal noise. This is due to the fact that the backscatter energy in HH polarization channel is much higher than that in HV polarization channel. The graphs produced for the images in HH polarization channel confirm that thermal noise is not present as both plotted lines overlap. We can see that the black line (before thermal noise correction) overlaps with the blue line (after thermal noise correction).

8.1.2 Radiometrically calibrated SAR images

Before proceeding to post-processing of SAR data, calibration should be performed to convert the DN values into physical units (dB). Calibration performed for both datasets using the SNAP tool.

Below, in figure 8.4 and figure 8.5 the radiometrically calibrated SAR datasets are presented.

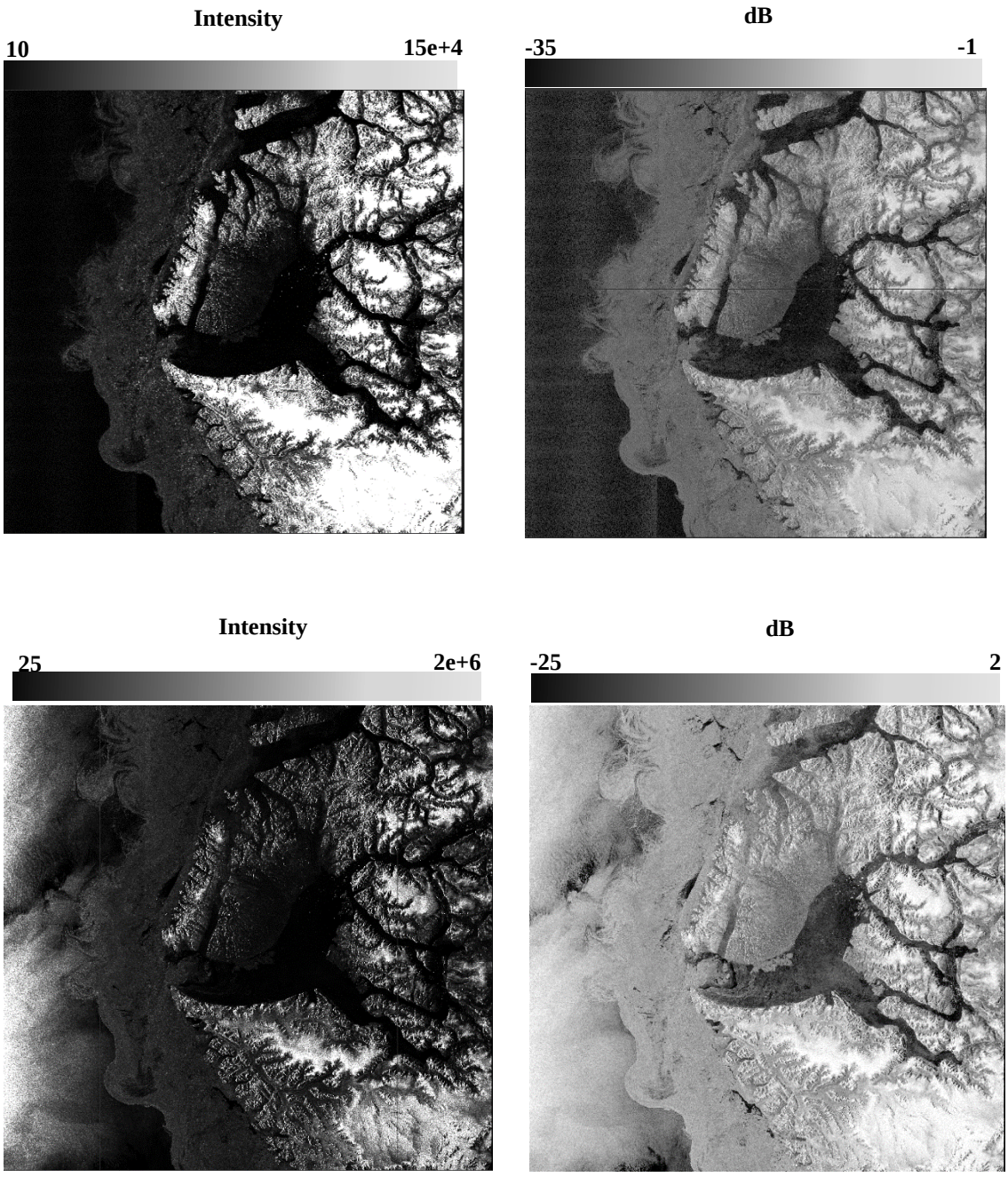

Figure 8.4: Image calibration in both polarization channels has been performed for the data captured in 23 of February in 2016. On the top, calibration has been performed in HV polarization channel and on the bottom in HH polarization.

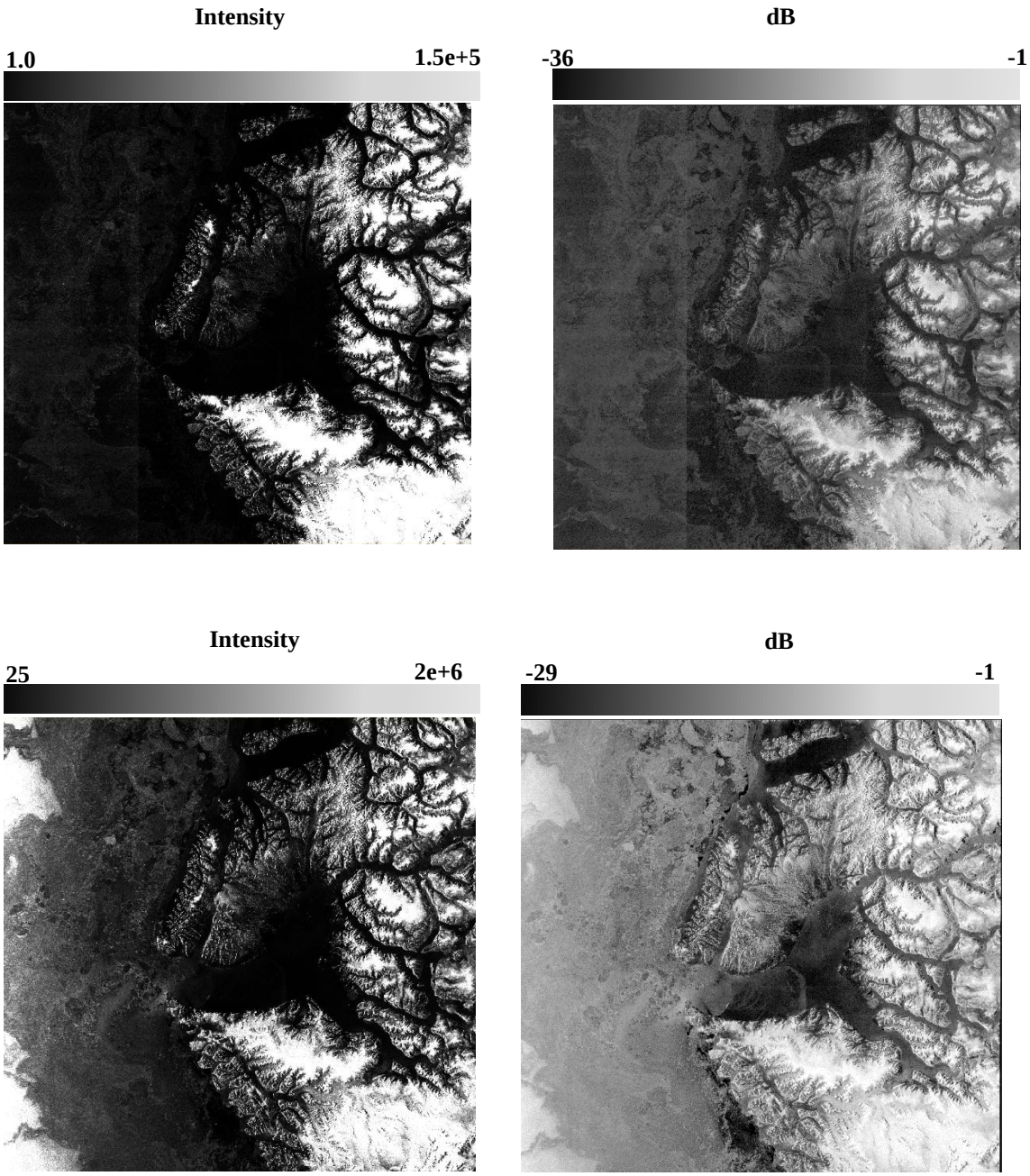

Figure 8.5: Image calibration in both polarization channels has been performed for the data captured in 25 of May in 2016. On the top, calibration has been performed in HV polarization channel and on the bottom in HH polarization.

The units of radiometrically calibrated SAR images are expressed in decibels (dB). Sigma nought (σ^0) describes the strength of the backscatter radar signal after interacting with the sea ice. The higher the dB values the brighter the SAR image, the lower the dB values, the darker the SAR image.

The backscatter coefficient for the dataset of February in 2016 range from -25 to 2 dB for HH polarization and from -35 to -1 for HV polarization. Low dB values correspond to areas where calm waters or young ice is present. Due to their smooth surface, they cause a specular reflection to the radar signal and only a small proportion of the energy reaches the sensor. On the other hand, high dB values can be attributed to rough surfaces such as old ice and rough FYI. The difference between HH and HV polarization channels in the two images is very obvious. The backscatter coefficient for HV polarization channel is lower than the backscatter coefficient in HH polarization channel. Very high dB values (up to 2dB) where the water is present can be observed in the HH image, while in HV image, the water has very low backscatter energy (close to -30dB).This is because HV polarization is not affected by the wind.

For the datasets captured in May of 2016, the backscatter coefficient of HH channel range from -29 to -1 dB and from -36 to -1 for HV channel. High dB values in this dataset are produced by the big sea ice floes (old ice and FYI). Lower intensity values can be seen at calm waters and new ice. The residuals after the thermal noise reduction in HV polarization channel are obvious.

8.1.3 Normalization of the incidence angle for the SAR data

The results of the linear regression analysis for normalizing the incidence angle can be viewed in figure 8.6. The pre-computed coefficients that were derived by regression analysis from incidence angle (20^0-49^0) were used for the normalization. For the selection

of the reference incidence angle, the most suitable option is the middle angle of the SAR image. Hence, the incidence angle was normalized to 30^0. We can see in the plots below that the incidence angle dependency on the backscatter energy is not present after incidence angle normalization.

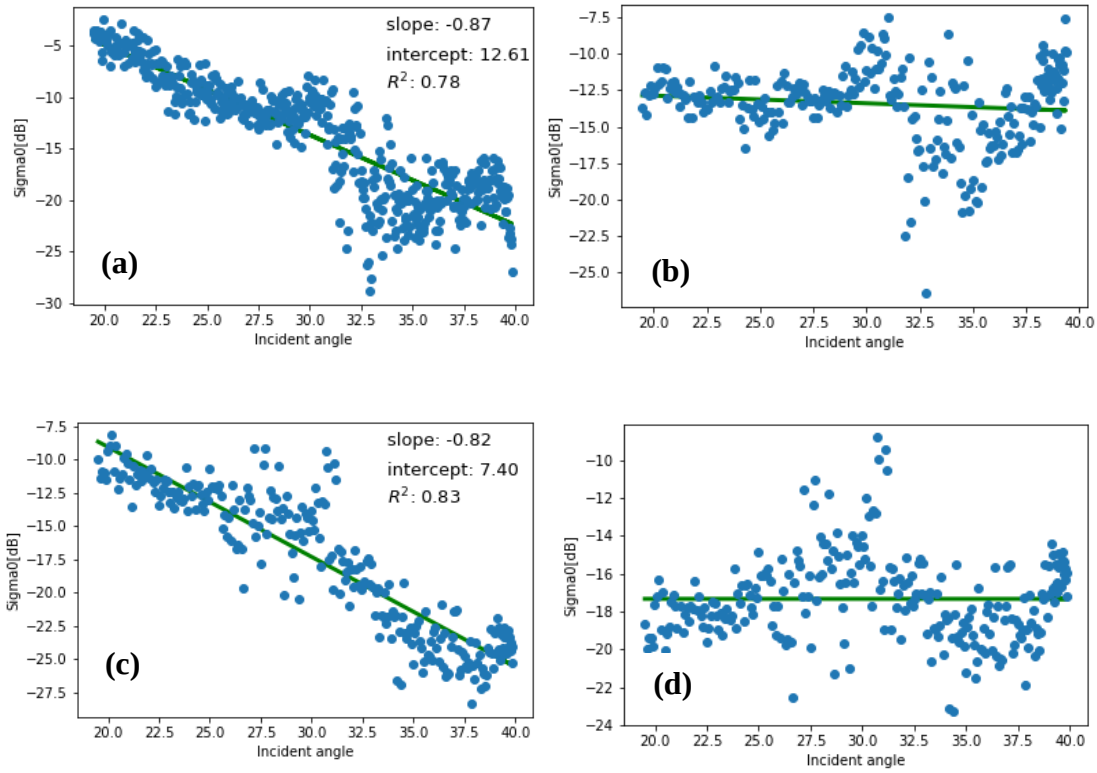

Figure 8.6. (a) EW SAR product 2016/02/23 and (b) normalization of incidence angle. (c) EW SAR product 2016/05/25 and (d) normalization of incidence angle

8.1.4 Speckle noise suppression and comparison of different filters

A number of filters with various window sizes (3x3, 5x5 and 7x7) were applied to SENTINEL-1 SAR images for minimizing the speckle noise. These filters are the Median filter, Boxcar filter, Frost filter, Lee filter and Lee sigma filter. The PyRadar (Herranz and Tita 2013) python package and SNAP toolbox were employed for speckle noise suppression. For evaluating the performance of the filters, the SAR images were segmented. The segmented images contains homogeneous areas and linear features.

In order to evaluate the capability of those filters not only in reducing the speckle noise but preserving the image details and content, a number of quantitative performance measures were employed and visual inspection was performed. Figures 8.7 and 8.8 show the de-speckled images using different speckle noise suppression filters.

8.1.4.1 Visual assessment

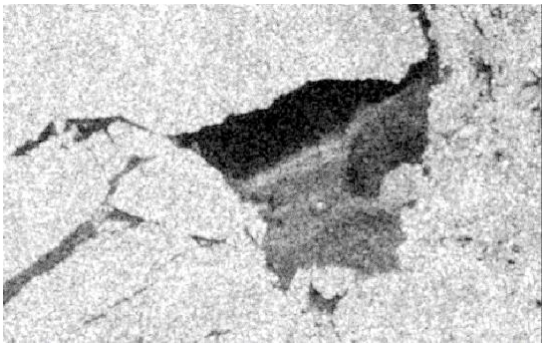

Original SAR image

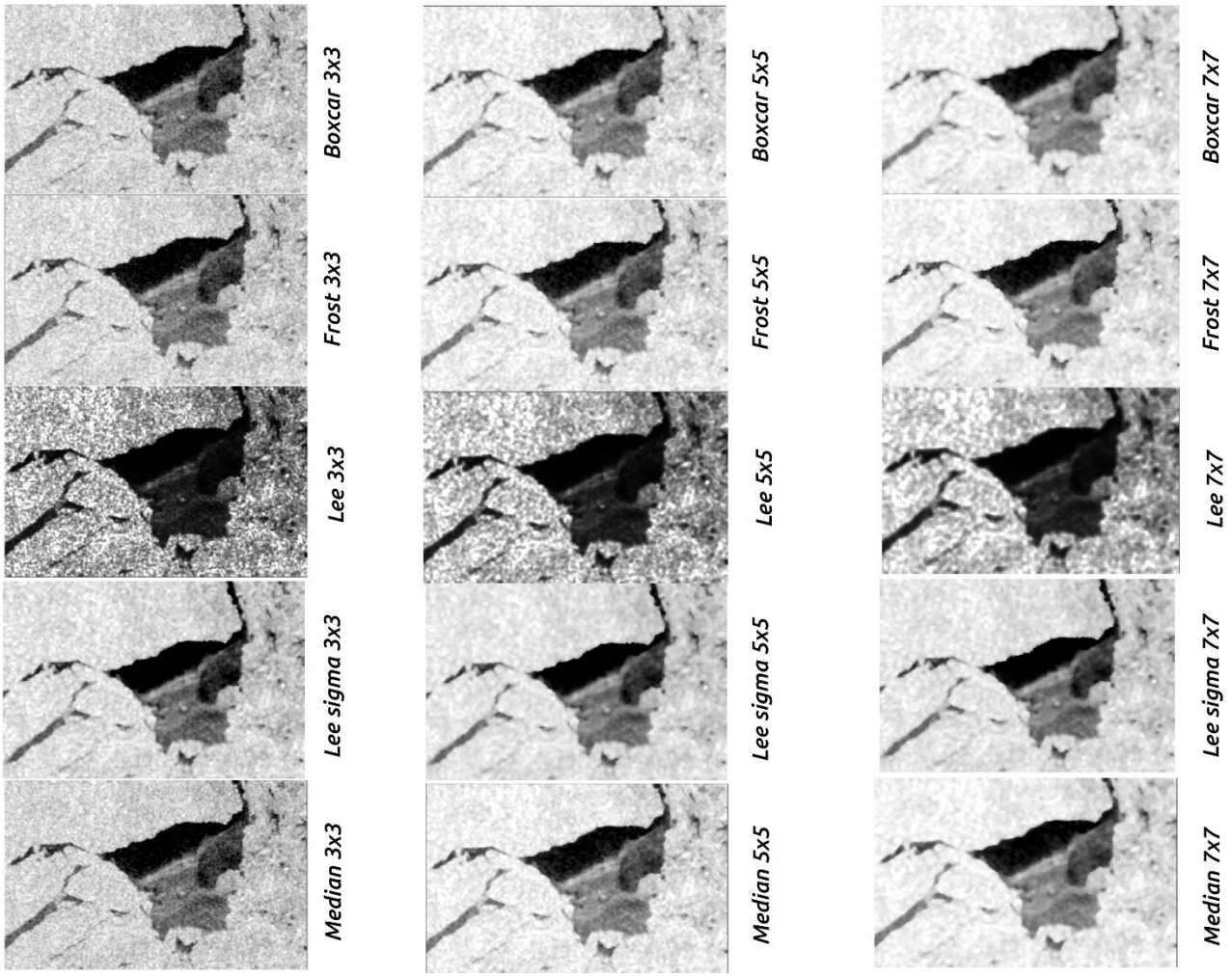

Figure 8.7. Filtered SENTINEL-1 images (February 2016) with various window sizes

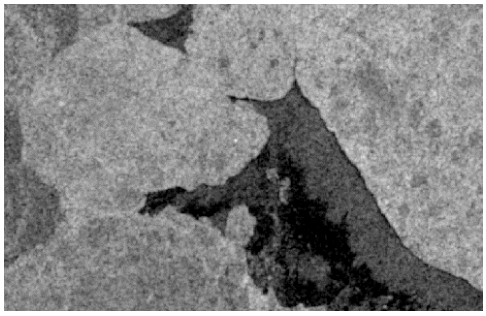

Original SAR image

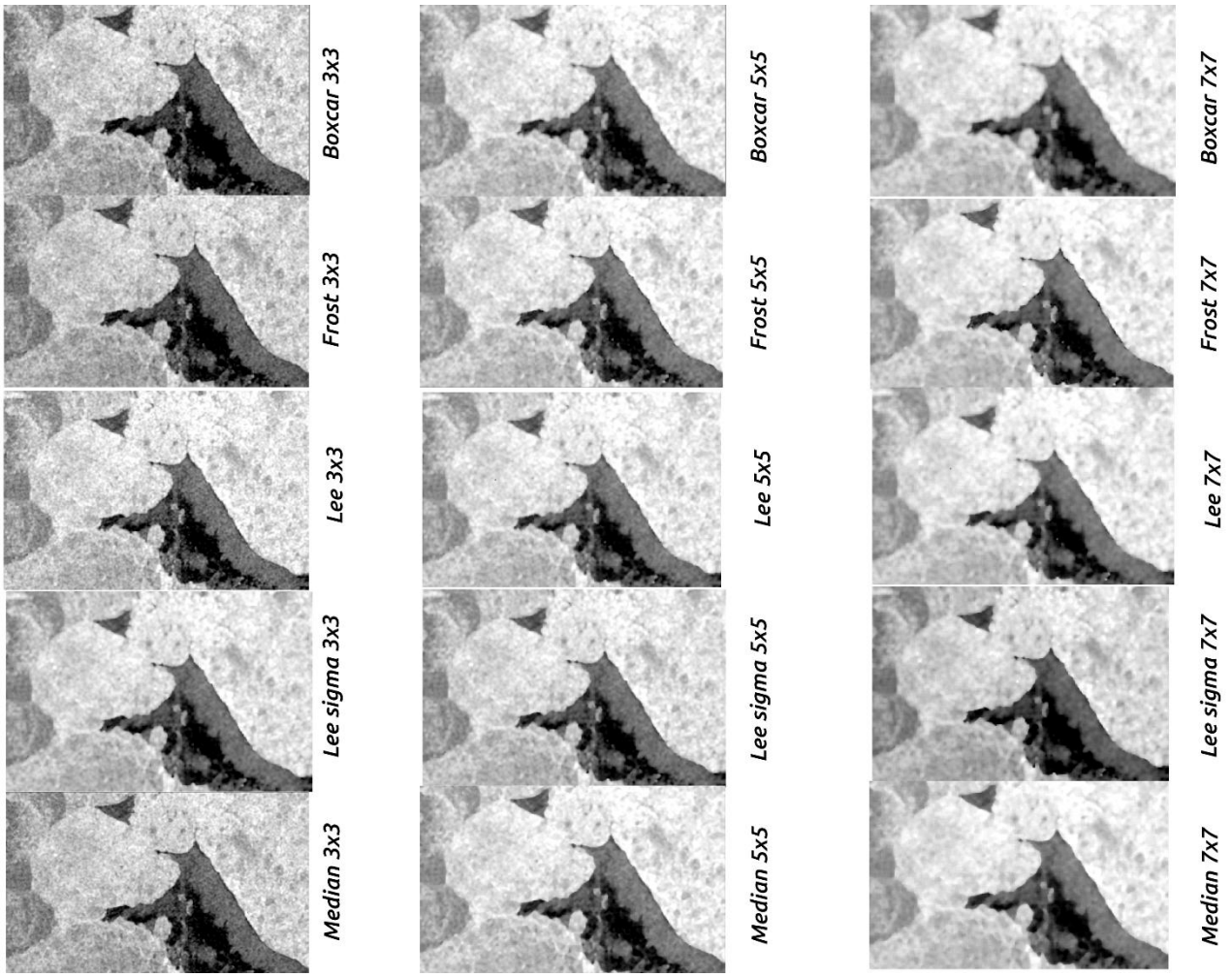

Figure 8.8. Filtered SENTINEL-1 images (May 2016) with various window sizes

Overall, all speckle filters are capable of minimizing the speckle noise and preserve the edges. We can observe that by increasing the size of the window (from 3x3 to 7x7) for all filters, the noise is further reduced but it blurs the SAR image. Hence, this results in losing image details and valuable information.

In figure 8.7, the Lee filter managed to preserve most of the image details but the noise suppression is inadequate. The noise (black and white) is still apparent in the de-speckled image. It can also be observed, in the center of the image subset, there is some information loss. The young ice is not clearly visible. In terms of Median filter, by taking a closer look at the dark area (water), we can observe that some gray speckles remained after noise suppression. Boxcar and Lee sigma performed the best amongst all the other filters.

For the SAR scene of May 2016, we can also observe for the speckles of the Median filter left in the water. However, all de-speckle filters performed well in achieving a detail preserving effect.

Before deciding which speckle filter should be used for this study, a quantitative assessment should be performed. By combining the visual inspection of the SAR images and the quantitative assessment, a more intuitive decision can be made.

8.1.4.2 Quantitative assessment

For the quantitative assessment, three performance measures including normalized mean (NM), standard deviation to mean (STM) and speckle suppression index (SSI) were computed.

Normalized mean is used to examine the ability of the filter to preserve the mean of homogeneous areas (equation 8.1).

$$NM = \frac{M_{filtered}}{M_{original}} \qquad 8.1$$

Where $M_{filtered}$ is the mean of the de-speckled image and $M_{original}$ is the mean of the original image. The closer the normalized mean is to one, the better the filter's ability to preserve the mean.

Standard deviation to mean is used for determining the filter's ability to suppress the speckle noise (equation 8.2).

$$STM = \frac{Standard\ deviation}{Mean} \qquad 8.2$$

For the equation, the standard deviation and the mean of the filtered image are used. Low STM values indicate a better noise suppression

Another measure quantitative for assessing the performance of a filter in reducing the speckle noise is the speckle suppression index. The speckle suppression index is the coefficient of variance of the filtered image normalized by that of the original image, which is defined as (Qiu et.al 2004)

$$SSI = \frac{\sqrt{Var(R_f)}}{Mean(R_f)} \frac{Mean(R_f)}{\sqrt{Var(R_f)}} \qquad 8.3$$

Where R is the original image and R_f is the de-speckled image. A de-speckled image tend to have lower variance compared to the original image due to the noise suppression. Hence, SSI tends to be less than one. The lower the SSI value the better the noise suppression. Tables 8.1 and 8.2 illustrate the results.

Filters	Pol.	NM	STM	SSI
Boxcar 3x3	HH	1.000	0.533	0.998
	HV	1.000	0.640	1.000
Boxcar 5x5	HH	1.000	0.493	0.995
	HV	1.000	0.573	0.997
Boxcar 7x7	HH	1.000	0.472	1.000
	HV	1.000	0.537	0.992
Frost 3x3	HH	0.999	0.534	1.000
	HV	0.998	0.644	0.997
Frost 5x5	HH	0.997	0.500	0.998
	HV	0.995	0.589	0.994
Frost 7x7	HH	0.996	0.484	1.000
	HV	0.994	0.567	0.997
Lee 3x3	HH	0.999	0.534	0.993
	HV	0.999	0.641	0.999
Lee 5x5	HH	0.997	0.497	0.996
	HV	0.997	0.576	1.000
Lee 7x7	HH	0.996	0.479	1.000
	HV	0.996	0.544	1.000
Lee Sigma 5x5	HH	1.000	0.508	0.998
	HV	1.000	0.621	0.997
Lee Sigma 7x7	HH	1.000	0.494	1.000
	HV	1.000	0.599	0.998
Median 3x3	HH	0.986	0.545	1.000
	HV	0.969	0.650	1.000
Median 5x5	HH	0.967	0.506	1.000
	HV	0.940	0.579	1.000
Median 7x7	HH	0.959	0.487	0.997
	HV	0.925	0.546	1.000

Table 8.1. Noise suppression and edge preservation characteristics of different filters for the dataset of February 2016

Filters	Pol.	NM	STM	SSI
Boxcar 3x3	HH	0.999	0.682	0.997
	HV	0.999	0.673	1.000
Boxcar 5x5	HH	0.999	0.640	0.997
	HV	0.999	0.611	1.000
Boxcar 7x7	HH	0.999	0.615	0.997
	HV	1.000	0.577	1.000
Frost 3x3	HH	0.999	0.684	0.998
	HV	0.997	0.677	1.000
Frost 5x5	HH	0.996	0.647	0.997
	HV	0.994	0.623	1.000
Frost 7x7	HH	0.995	0.628	0.999
	HV	0.993	0.597	0.996
Lee 3x3	HH	0.999	0.683	1.000
	HV	0.999	0.674	0.997
Lee 5x5	HH	0.998	0.642	1.000
	HV	0.998	0.613	0.997
Lee 7x7	HH	0.997	0.619	0.999
	HV	0.997	0.580	1.000
Lee Sigma 5x5	HH	1.000	0.665	0.996
	HV	1.000	0.649	0.998
Lee Sigma 7x7	HH	1.000	0.648	1.000
	HV	1.000	0.630	0.993
Median 3x3	HH	0.980	0.694	0.999
	HV	0.977	0.690	1.000
Median 5x5	HH	0.961	0.652	1.000
	HV	0.956	0.652	0.996
Median 7x7	HH	0.950	0.629	1.000
	HV	0.944	0.589	1.000

Table 8.2. Noise suppression and edge preservation characteristics of different filters for the dataset of February 2016

When comparing the above filters (for both datasets) for their ability in noise suppression (STM and SSI) and preserving the mean of a homogeneous area, the following results can be observed.

For the dataset in February 2016, Boxcar 5x5 and Lee sigma 7x7 filters have the lowest values of 0.493 and 0.494 respectively in STM quantitative measure highlighted in light gray color. Low STM value indicates a good performance in suppressing the noise. A good performance from Boxcar and Lee sigma filters observed for SSI measure achieving a value below 1. The worst performance on noise suppression was achieved by Frost 3x3 with an STM score of 0.684. In terms of NM quantitative measure, Boxcar and Lee sigma scored the highest value of 1 indicating the ability of those filters to effectively preserve the mean in homogeneous areas.

For the dataset in May 2016, Boxcar 5x5 and Lee sigma 7x7 achieved the best results scoring the lowest value in STM highlighted in light gray color. Also, in terms of SSI, Boxcar 7x7 and Lee sigma 5x5 have the lowest value among all filters indicating a better ability in suppressing the noise. Frost 3x3 had the worst performance amongst the all filters. In terms of NM, Boxcar and Lee sigma showed a great ability on preserving the mean achieving a score of 1.

After assessing all the filters visually and quantitatively, this suggests that Boxcar filter 5x5 and Lee sigma filter 5x5 performed the best. Both filters are capable of preserving the details of the image and sufficiently suppress the speckle noise. In this study, The Lee sigma filter was adopted as it has been widely used in suppressing the noise from SAR images.

8.2 GLCM interpretation results

As we have seen in the chapter 6, four GLCM parameters (displacement, orientation, quantization levels and window size) are used for creating the GLCM matrix. In this study, the role of the window size and gray levels quantization are tested, while the orientation and displacement parameters are not discussed since it is accepted by many authors that a displacement value of 1 or 2 and an average of the four orientations (N, S, E, W) yield better results. Hence, for this research, a displacement value of 1 and the average of four orientations was used. Mahotas (Coelho 2013) python library employed for texture analysis.

8.2.1 The effect of window size in GLCM calculation

The choice of the window size for GLCM calculation is of great importance. In order to achieve good class seperability on the SAR image, the appropriate window size should be chosen. All texture values were scaled to the same range (between 0 and 1) so that one texture measure will not dominate the other due to its greater range. Four window sizes (5x5, 7x7, 9x9 and 11x11) are tested and the Transformed Divergence (TD) distance is computed for two sea ice types.

TD is a measure of class seperability and its values ranges between 0 and 1. A values close to 1 indicate that the two classes are perfectly separated and a value close to 0 indicates that the two classes overlap. The TD distance between two classes (c and d) is given by:

$$TD = 2(1 - \exp(\frac{D_{cd}}{8})) \tag{8.4}$$

$$D_{cd} = \frac{1}{2}\, tr(V_c - V_d)(V_c^{-1} - V_d^{-1}) + \frac{1}{2} tr((V_c^{-1} - V_d^{-1})(M_c - M_d)(M_c - M_d{}^T)) \tag{8.5}$$

Where:

V_c, V_d = Covariance matrix of classes c and d

M_c, M_d = Mean values of classes c and d

tr = trace function

T = transpose

Figures 8.9 and 8.10 show the effect of window size in class seperability is illustrated.

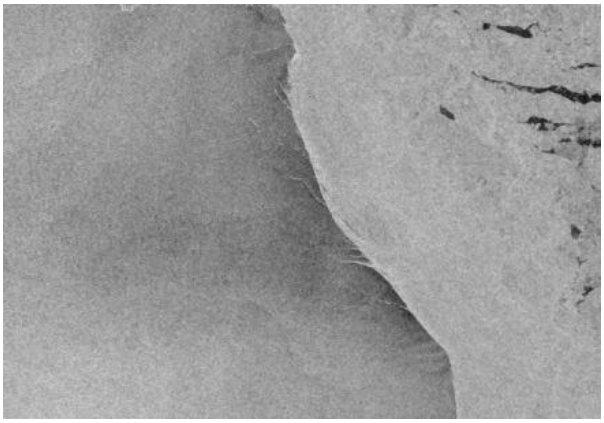

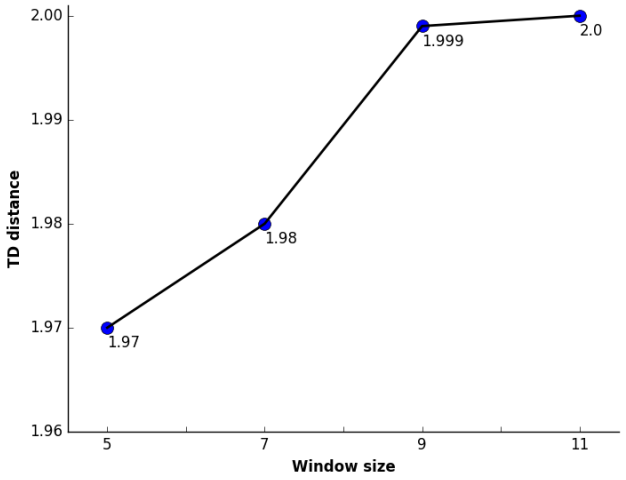

Figure 8.9. Seperability between rough waters and sea ice of various window sizes for the SAR image of February 2016

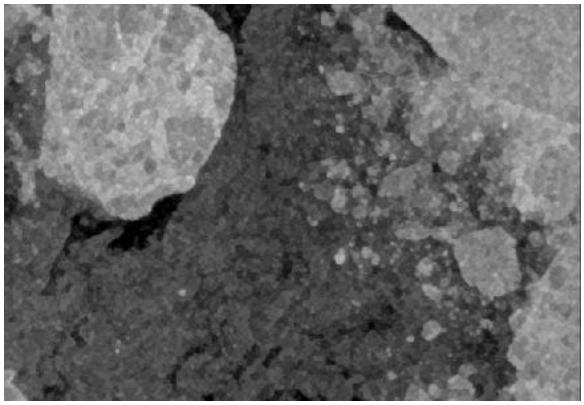

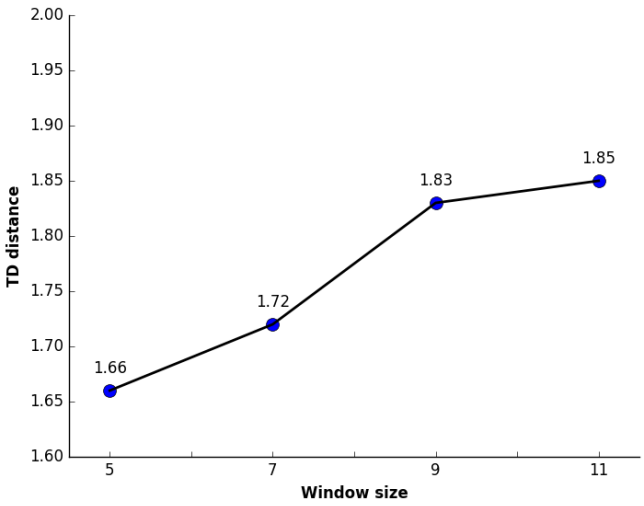

Figure 8.10. Seperability between new ice and first year ice of various window sizes for the SAR image of May 2016

By looking at both graphs, we see that the class seperability increases linearly with increasing the window size. The figure 8.9 shows two classes, rough waters and young ice. Normally, water can be easily be discriminated from sea ice due to it specular reflection while the backscatter from sea ice is stronger. When rough waters are present due to strong winds, its discrimination from sea ice is more challenging due to their similar backscatter coefficient. On the graph, it can be observed that by increasing the window size, the discrimination between the two classes improves where it reaches the value of 2 (complete separation) when a window size of 11x11 is selected.

In figure 8.10, first year ice and new ice are present. Using a window size 5x5, the seperability value for the two classes is 1.66. We can observe a linear increase on the seperability value when the window size increases reaching a maximum value of 1.85 for window size 11x11.

Hence, in this study, the 11x11 window size is adopted for calculating the GLCM matrix.

8.2.2 The effect of various grey level quantizations in the GLCM computation

In order to investigate the effect of grey level quantization in separating different sea ice classes, the SAR images have been reduced to 8, 32 and 64 levels. Smaller grey level values accelerate the computation of the GLCM matrix and reduce noise, but on the other hand, there is an information loss. It is expected that, a small number of quantization levels would reduce the classification accuracy and class seperability while a higher number of quantization levels is expected to improve both sperability and classification accuracy.

The goal of experimenting with various grey levels is to find the optimum quantization which produces the best separation between classes. In order to assess the effectiveness of the various grey levels, a spatial subset of both datasets (900 x 600 pixels) was segmented consisted of sea ice floes and linear features.

The results of the texture analysis using different quantization levels are described below.

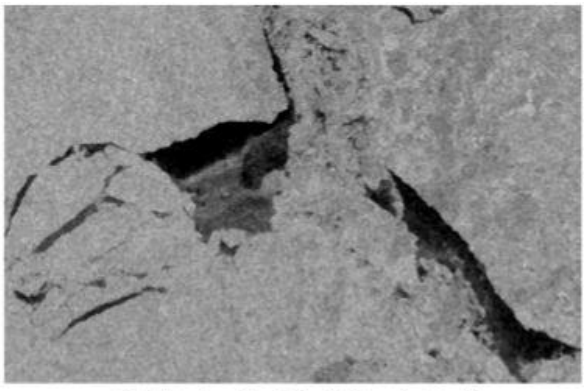

Original subset in HH polarization

ASM 8 gray levels

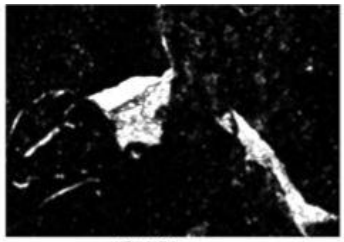

ASM 32 gray levels

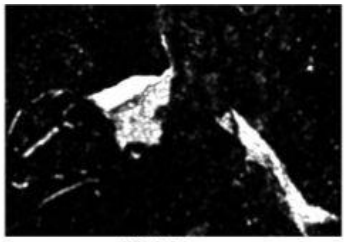

ASM 64 gray levels

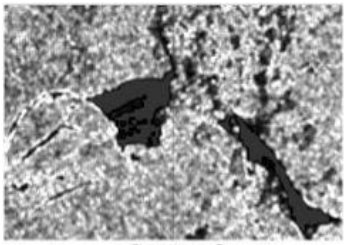

Contrast 8 gray levels

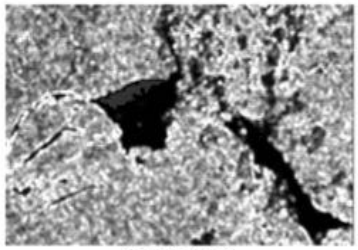

Contrast 32 gray levels

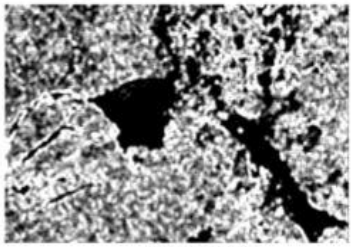

Contrast 64 gray levels

Correlation 8 gray levels

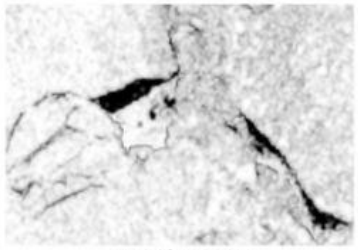

Correlation 32 gray levels

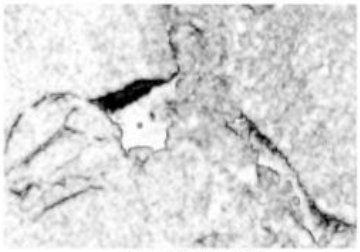

Correlation 64 gray levels

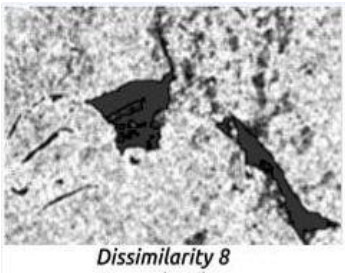

Dissimilarity 8 gray levels

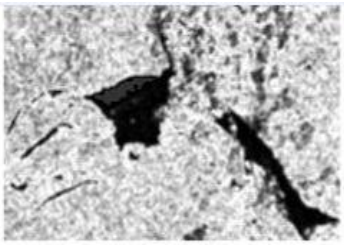

Dissimilarity 32 gray levels

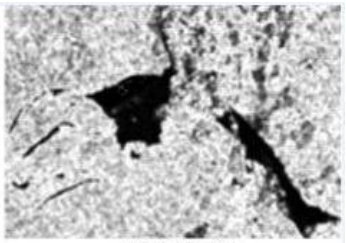

Dissimilarity 64 gray levels

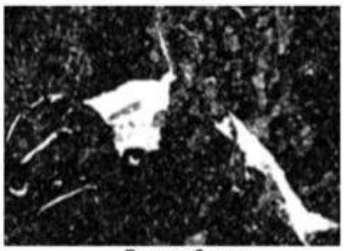

Energy 8 gray levels

Energy 32 gray levels

Energy 64 gray levels

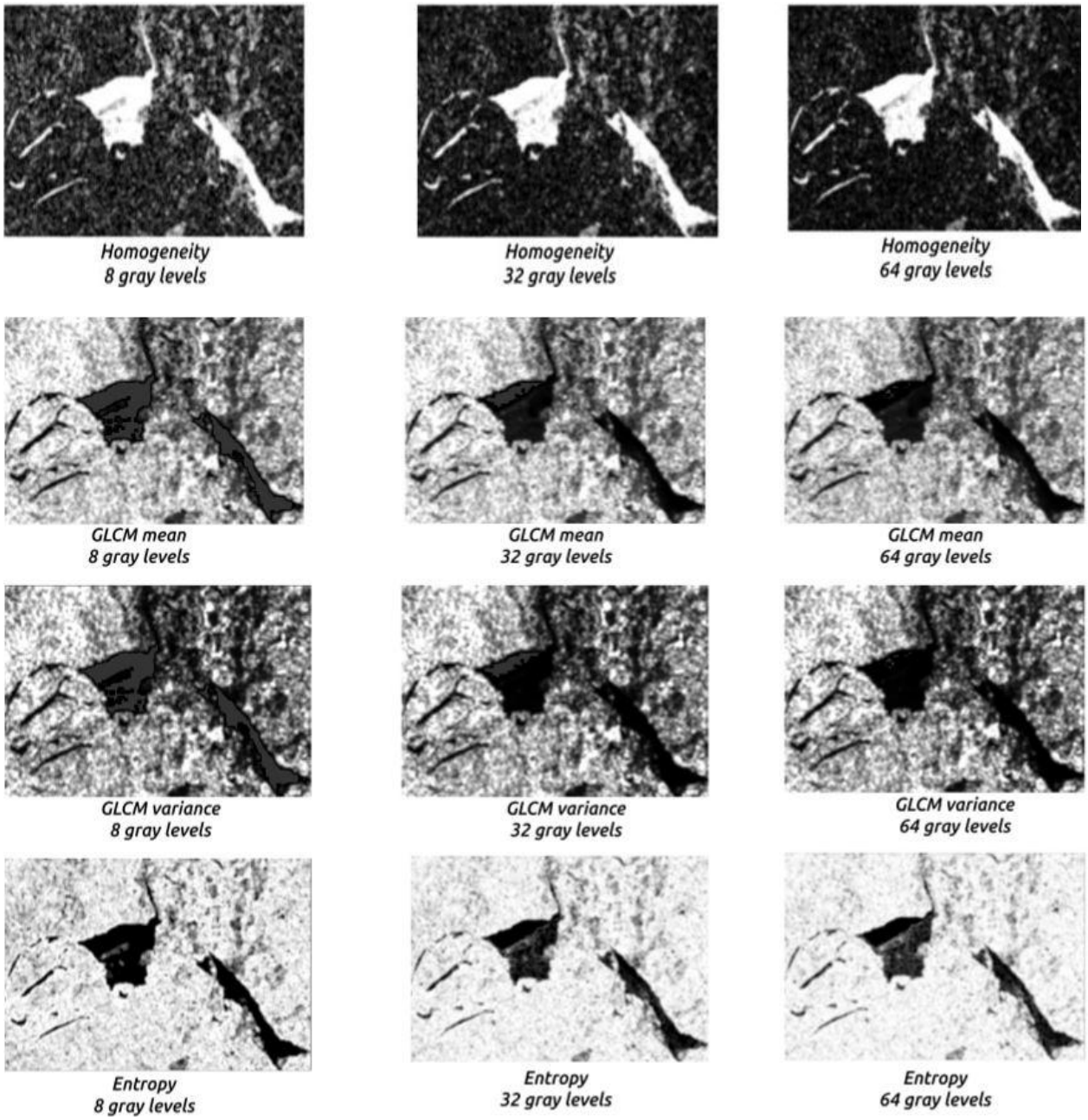

Figure 8.11. Texture measures (HH polarization) in various quantization levels for the SAR image of February 2016

ASM
8 arav levels

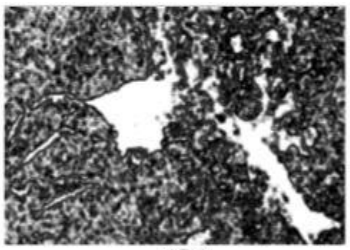

ASM
32 arav levels

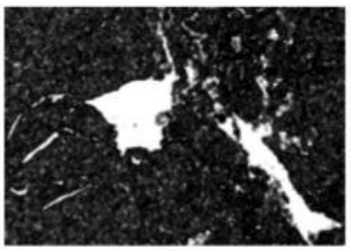

ASM
64 gray levels

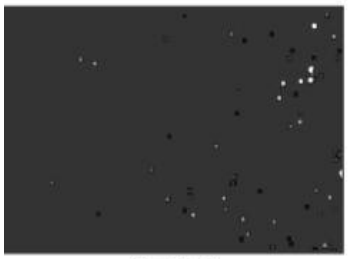

Contrast
8 arav levels

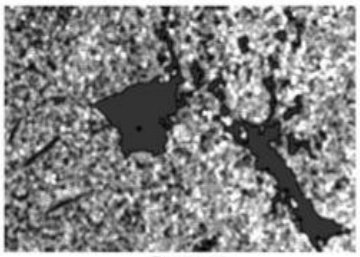

Contrast
32 gray levels

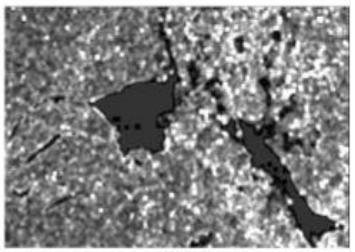

Contrast
64 gray levels

Correlation
8 arav levels

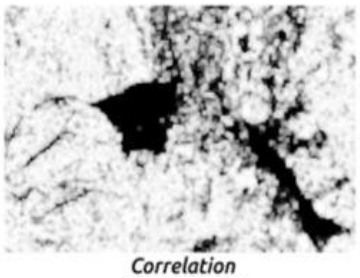

Correlation
64 gray levels

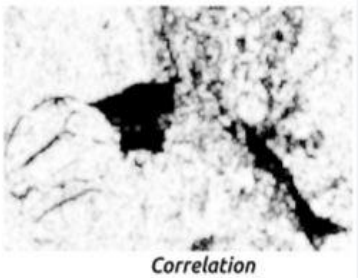

Correlation
64 gray levels

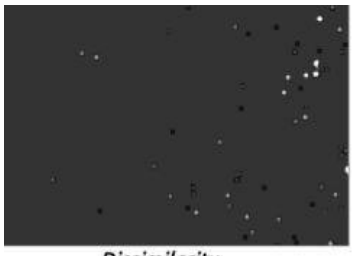

Dissimilarity
8 gray levels

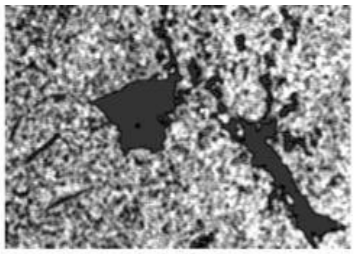

Dissimilarity
32 gray levels

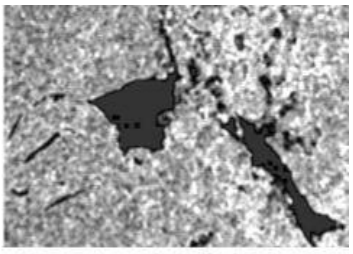

Dissimilarity
64 gray levels

Energy
8 gray levels

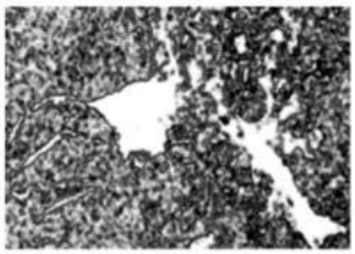

Energy
32 gray levels

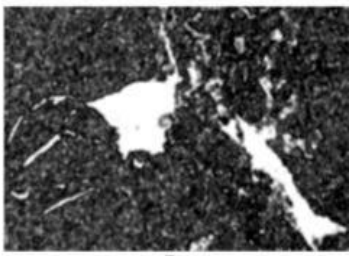

Energy
64 gray levels

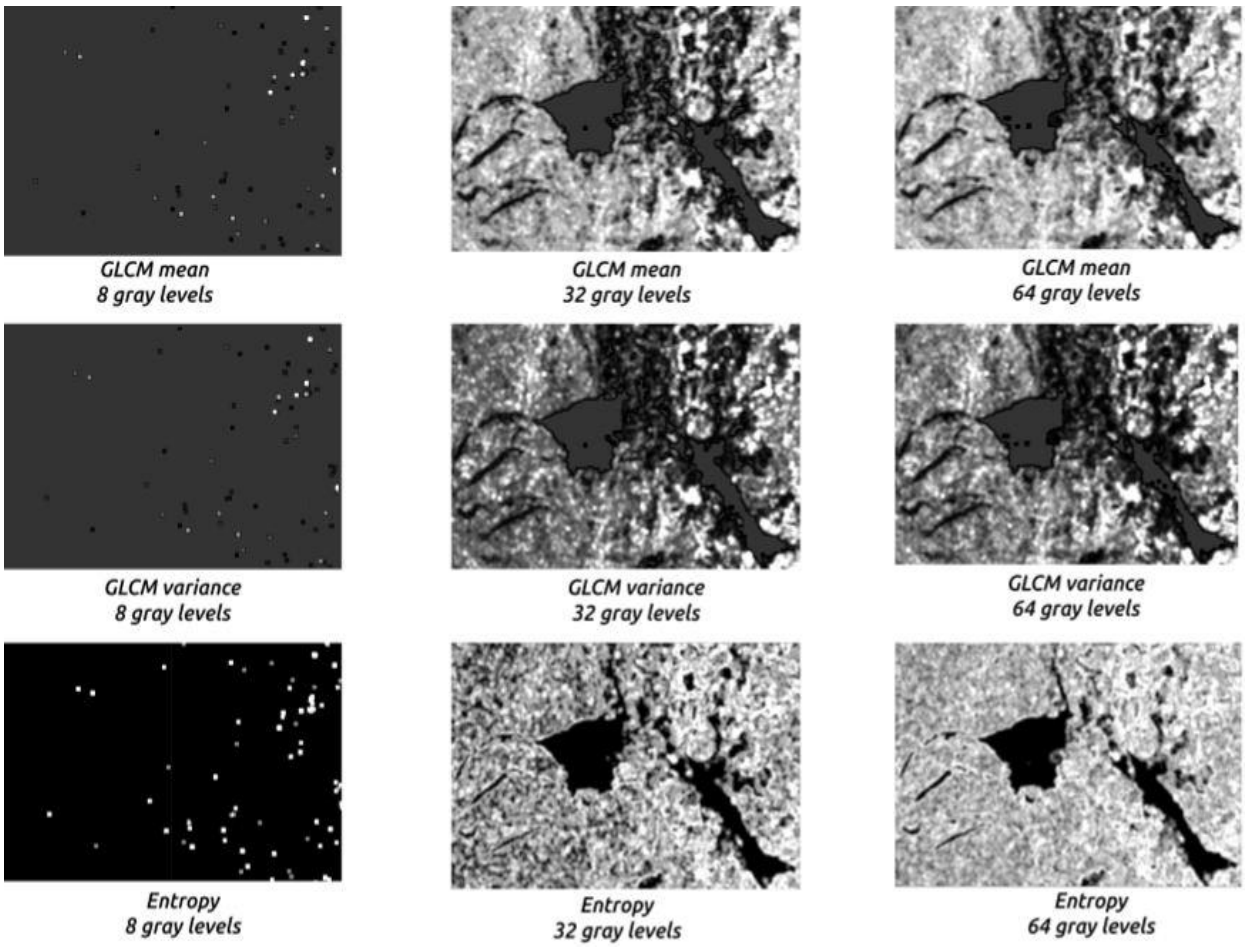

Figure 8.12. Texture measures (HV polarization) in various quantization levels for the SAR image of February 2016

Figure 8.11 shows the texture statistics that were calculated in HH polarization channel. ASM, homogeneity and energy produce almost identical results. These three measures express uniformity. Pixels with the same range of brightness levels appear smooth and high values are assigned to them. It can be observed that ASM, homogeneity and energy performed equally well in all three quantization levels. The leads (located on the left of the SAR image) have been successfully identified in the image with 8, 32 and 64 quantization levels. The open area in the center of the images is consisted of new ice and open water which failed to be identified (in all three texture measures) in the image with

8 grey levels, while the image of 64 grey levels contain more information and the two classes start to appear.

Contrast a dissimilarity are very similar. These measures show the local variation present in the image. In both coarse and higher quantization it is difficult to discriminate all three sea ice types present in the SAR image. Dissimilarity produces slightly better results than contrast as it successfully identify the leads. On the other hand, leads cannot be clearly identified in contrast.

The correlation measure has a strong increase in class separation with increasing quantization.

The last three texture measures (GLCM mean, GLCM variance and entropy) show an increase in classification accuracy with increasing quantization. Entropy and GLCM mean produce slightly better results in 64 grey levels compared to GLCM variance. Variance failed to identify the new ice class in the image. Surprisingly, better results achieved for variance in 32 grey levels.

Overall, all the texture measures presented above are capable of discriminating sea ice types. However, some features are statistically more significant than others. For example, ASM, energy and homogeneity are very similar measures with ASM to produce slightly better results. Also, contrast and dissimilarity are not the strongest candidates for class seperability compared to other texture measures.

In the figure 8.12, texture statistics for the HV polarization channel are shown. It can be clearly seen that the texture information of all measures have been completely lost in 8 quantization levels. The results in HV is compressed. In order to achieve a good class seperability in HV polarization, much higher quantization is needed. It is obvious that there is a very strong correlation between classification accuracy and grey levels. The discrimination of the sea ice classes increases with the increase of quantization.

In figure 8.13 and 8.14, the texture measures for the dataset of May 2016 are presented.

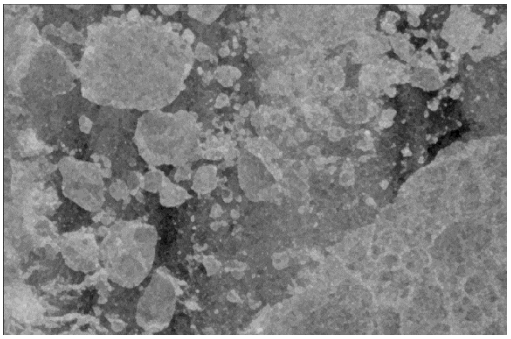

Original subset in HH polarization

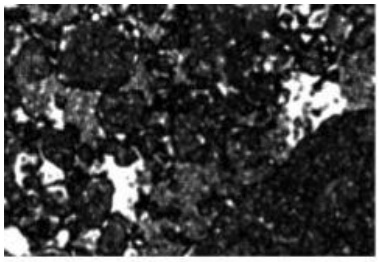

ASM 8 gray levels

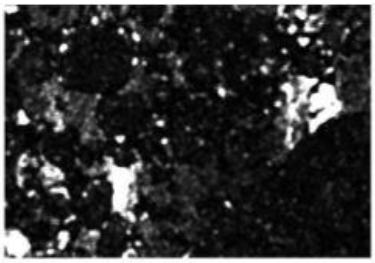

ASM 32 gray levels

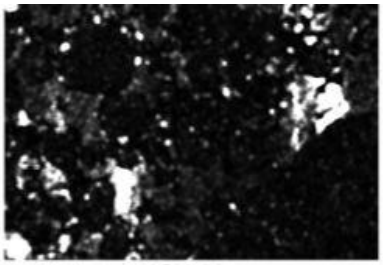

ASM 64 gray levels

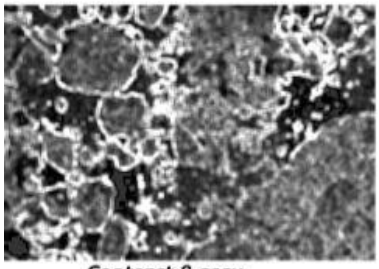

Contrast 8 gray levels

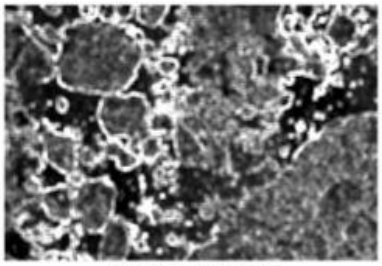

Contrast 32 gray levels

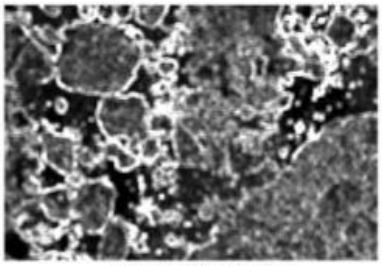

Contrast 64 gray levels

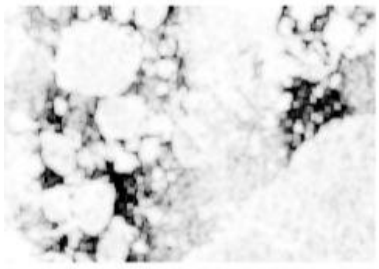

Correlation 8 gray levels

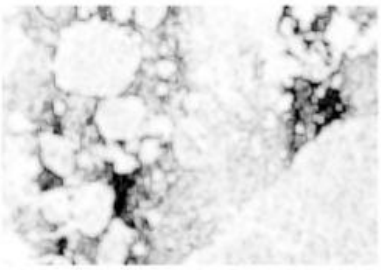

Correlation 32 gray levels

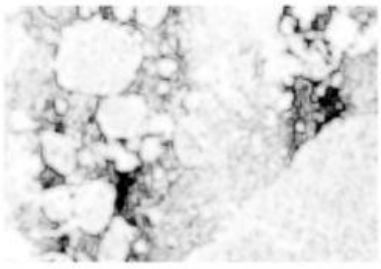

Correlation 64 gray levels

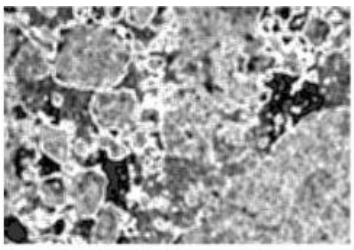

Dissimilarity 8 gray levels

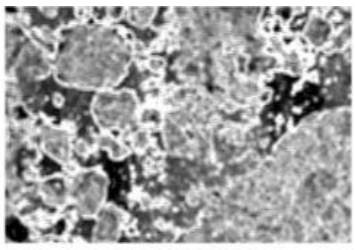

Dissimilarity 32 gray levels

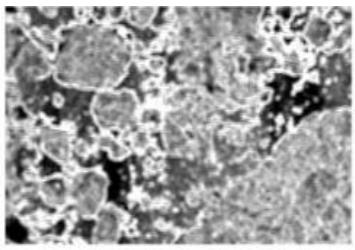

Dissimilarity 64 gray levels

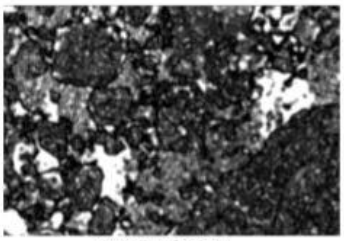

Energy 8 gray levels

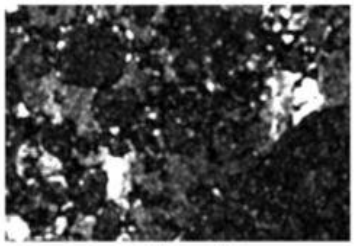

Energy 32 gray levels

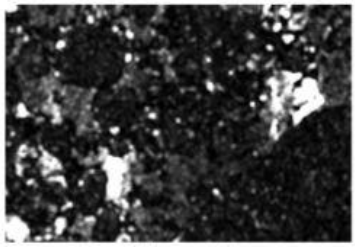

Energy 64 gray levels

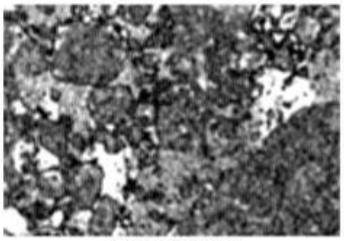

Homogeneity 8 gray levels

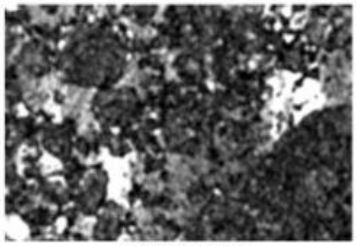

Homogeneity 32 gray

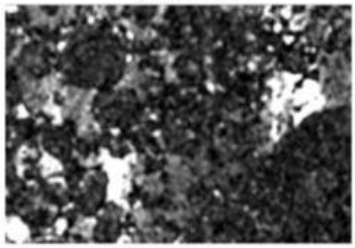

Homogeneity 64 gray

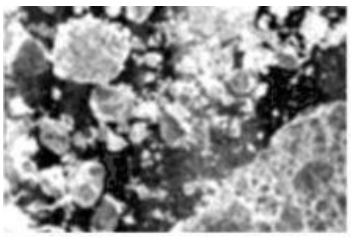

GLCM mean 8 gray levels

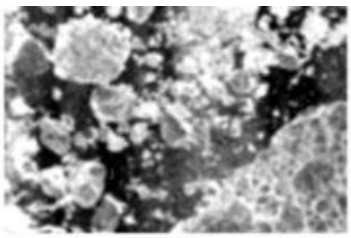

GLCM mean 32 gray levels

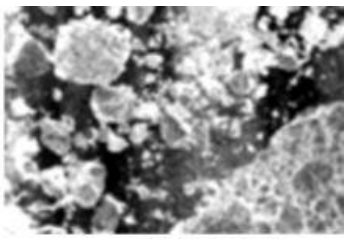

GLCM mean 64 gray levels

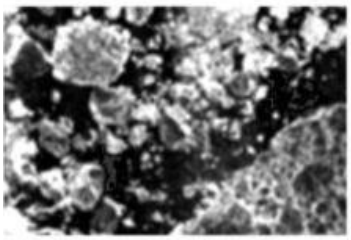

GLCM Variance 8 gray levels

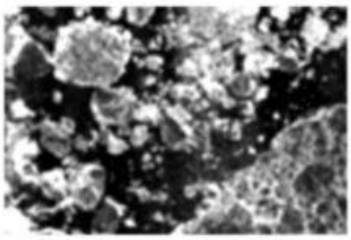

GLCM Variance 32 gray levels

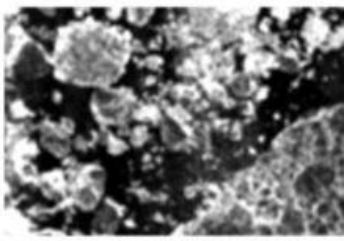

GLCM Variance 64 gray levels

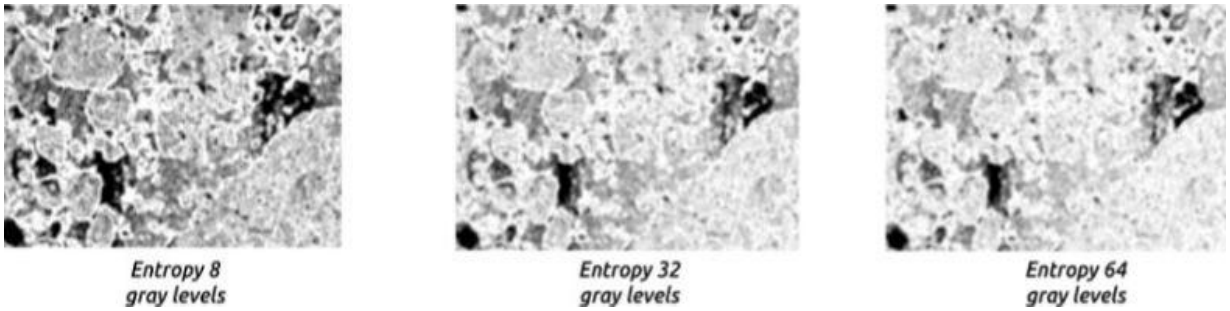

Figure 8.13. Texture measures (HH polarization) in various quantization levels for the SAR image of May 2016

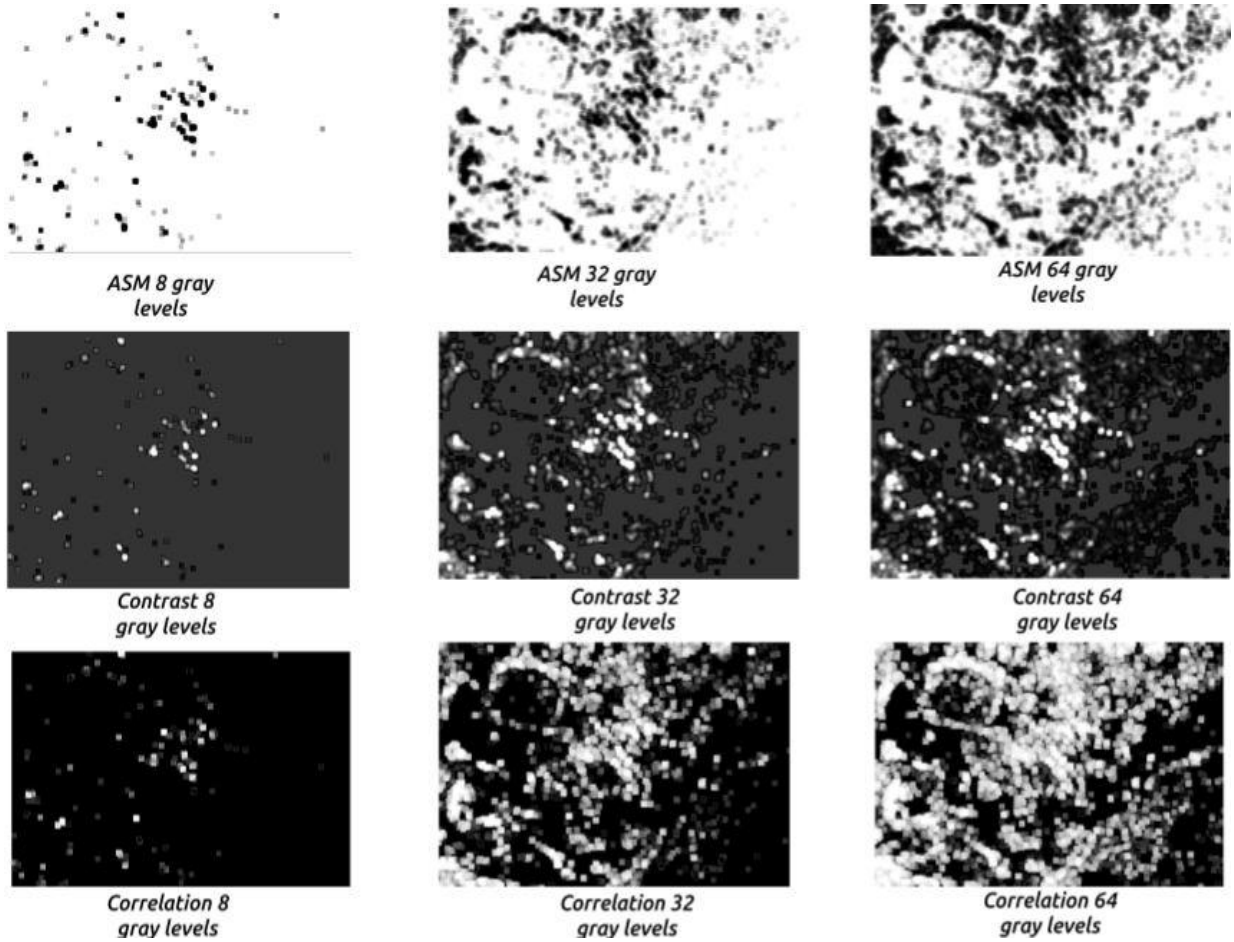

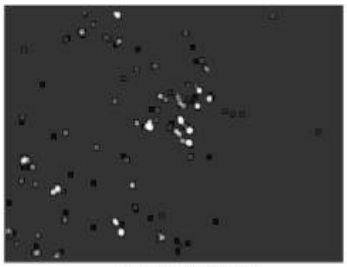

Dissimilarity 8 gray levels

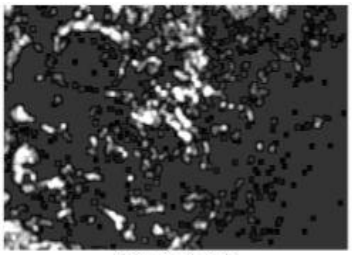

Dissimilarity 32 gray levels

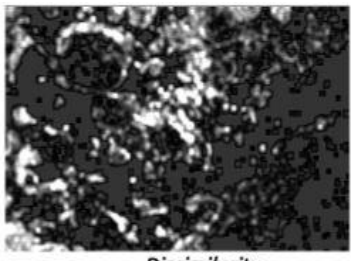

Dissimilarity 64 gray levels

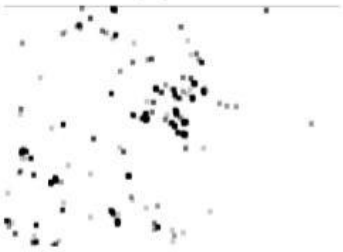

Energy 8 gray levels

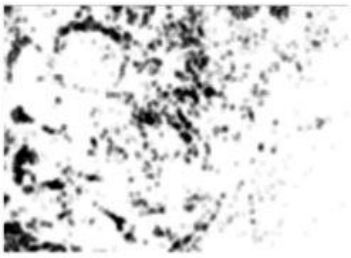

Energy 32 gray levels

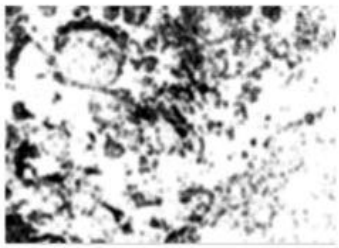

Energy 64 gray levels

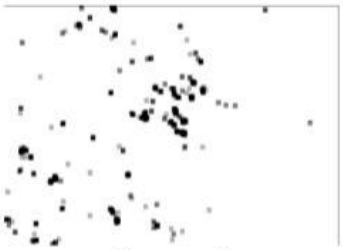

Homogeneity 8 gray levels

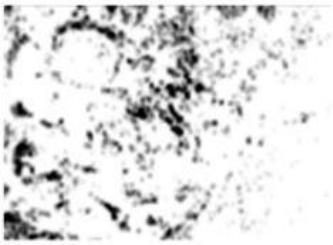

Homogeneity 32 gray levels

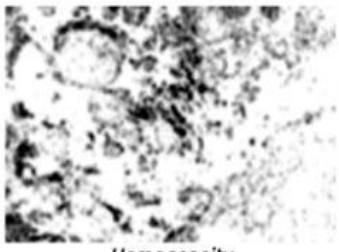

Homogeneity 64 gray levels

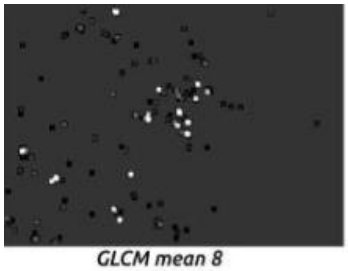

GLCM mean 8 gray levels

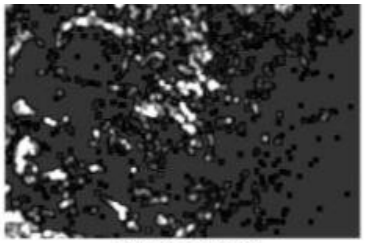

GLCM mean 32 gray levels

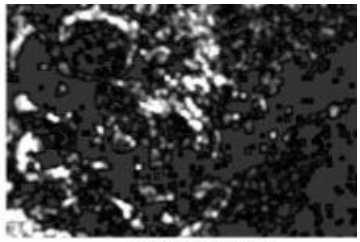

GLCM mean 64 gray levels

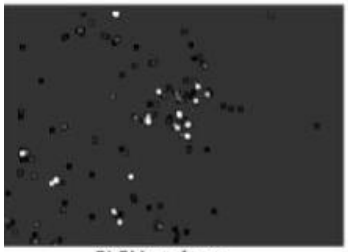

GLCM variance 8 gray levels

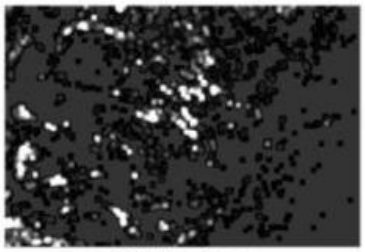

GLCM variance 32 gray levels

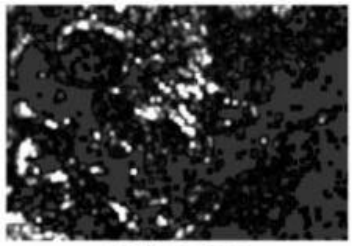

GLCM variance 64 gray levels

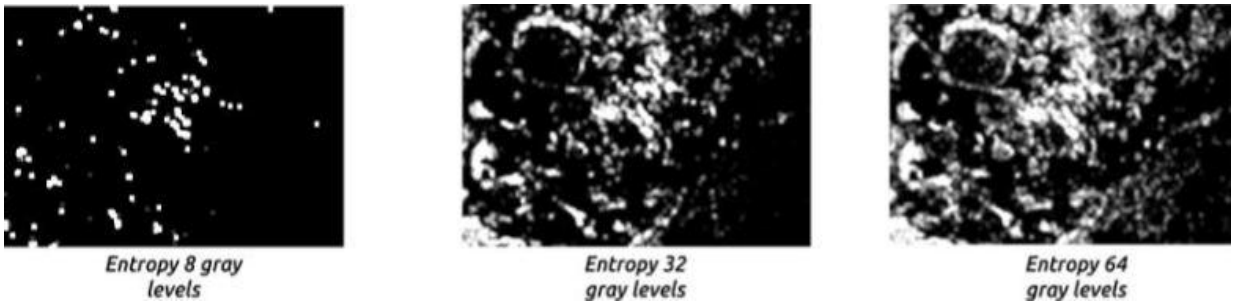

Figure 8.14. Texture measures (HV polarization) in various quantization levels for the SAR image of May 2016

In figure 8.13, the SAR images consisted of FYI floes, new ice and water. It can be observed that for ASM, energy and homogeneity, the increase of grey levels does not play a huge role in discriminating the different sea ice types. One would expect an image of 8 grey level value to perform much worse compared to the same image of 64 grey level values due to its much less dynamic range of values. We can see that uniform areas (water on the right of the image) have high values while less uniform areas (FYI) shown in darker color. Slightly better results (in terms of class seperability) can be observed in the SAR image with 64 quantization.

For dissimilarity and contrast, both texture measures have successfully captured the sea ice floes due to the high contrast between ice floes and new ice. The results are impressive even for image with the 8 quantization levels.

In correlation measure, we have very high values for the ice floes (which shows a linear relationship between the brightness levels of pixels in the radar image) which can be easily discriminated from the other sea ice types. We cannot observe a better performance in class seperability with increasing quantization.

The GLCM mean and GLCM variance can perfectly discriminate all sea ice types present in the image. These two statistics performed equally well in 8, 32 and 64 quantization levels and no major differences can be observed.

On the other hand, entropy, surprisingly performed better in 8 rather than in 64 grey levels. Hence, it is noticeable that 8 grey levels are sufficient to give information on sea ice types. The image in 64 levels is more difficult to interpret due to the higher noise introduced by the higher number of quantization levels.

In general, no big difference in sea ice discrimination can be observed for 8, 32 and 64 quantization levels. We have seen than an image of 64 grey levels might provide more information in terms of the image content, but it is not significantly different from an image of 32 or 8 grey levels.

On the other hand, texture statistics in HV polarization channel can be seen in figure 8.14. In 8 grey levels no information is retained and the image interpretation is impossible. Hence, there is a very strong correction between class seperability and increasing grey levels. Despite the fact the information in 64 quantization is much richer, still, the interpretation of the images is difficult.

After examining the texture statistics in different quantization levels, we can conclude that 64 grey levels contain more information in both HH and HV polarization which makes the interpretation easier and more accurate. Hence, in this study, quantization level of 64 was used for the calculation of GLCM matrix,

8.3 Classification training procedure

The training procedure of the SVM model was applied to both images. In this procedure, a set of data is selected from the SAR image into predefined classes (e.g. various sea ice types) and used to train the model in order to make accurate predictions. The two SAR scenes contain five sea ice classes and the only difference between the two scenes is that the image acquired in May of 2016 contains sea ice deformation to a greater extent.

The sea ice types for the first scene (2016-02-23) consists of, a) FYI, b) young ice, c) old ice, d) rough water and d) calm water. The selection of the training data was performed carefully through visual analysis of the SAR images and using previous classification results derived by Danish Meteorological Institute and Norwegian Sea Ice Service. The table 8.3 shows the number of the training data used for each sea ice class.

Type of the Sea Ice	**Number of training data (pixels)**
First Year Ice	10165
Young Ice	7972158
Old Ice	171607
Rough water	152356
Calm water	7381
Total	**831367**

Table 8.3: Number of training data for each sea ice type for the scene of February 23 of 2016

The two scenes were projected to polar stereographic map projection and the land was masked. This projection is mainly used for areas located at high latitudes. The polar stereographic projections is characterized as conformal which means that the shape of the features are accurately represented on the map.

The training data collected are shown in figures 8.15. Figure 8.16 shows the scatter plot produced for different ice types.

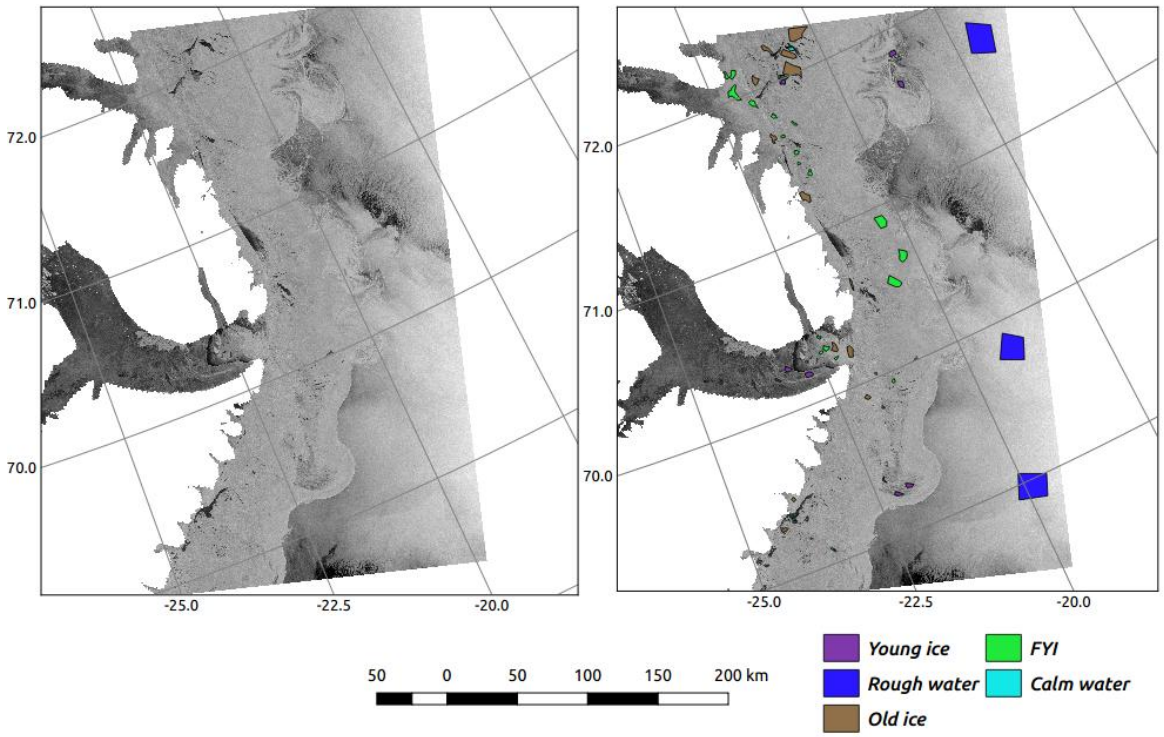

Figure 8.15: SAR image acquisition in February 23 of 2016 with training data. a) SAR image and b) SAR image with the training data overlaid

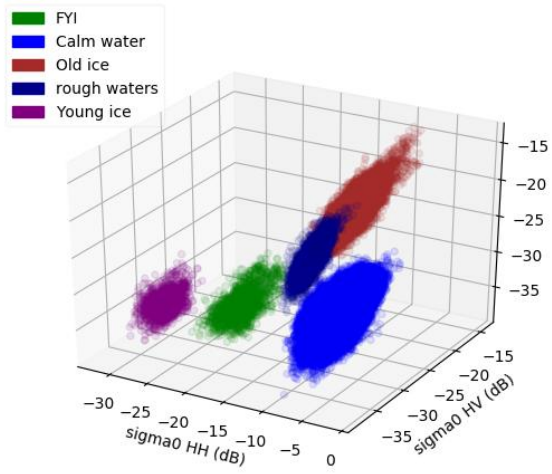

Figure 8.16. Scatter plot of sea ice types for the datasets of February 23 of 2016

The labeled dataset in figure 8.15 are distributed along the image after a careful examination of the different sea ice types contained in the scene. In the scatter plot, we can see the backscatter coefficient of each ice type. FYI, young ice and calm water are well separated, while there is some overlap between old ice and rough water. Due to the strong winds, waves formed in the sea produce a strong backscatter similar to that of the old ice.

The same training procedure and training data collection has been applied for the second scene captured in 2016-05-25 which is shown below. This scene consists of the following sea ice types, a) smooth FYI, b) rough FYI, c) young ice, d) old ice, e) rough water and f) calm water. Below, we can see the labeled datasets selected and the amount of training data which as shown in the table 8.4

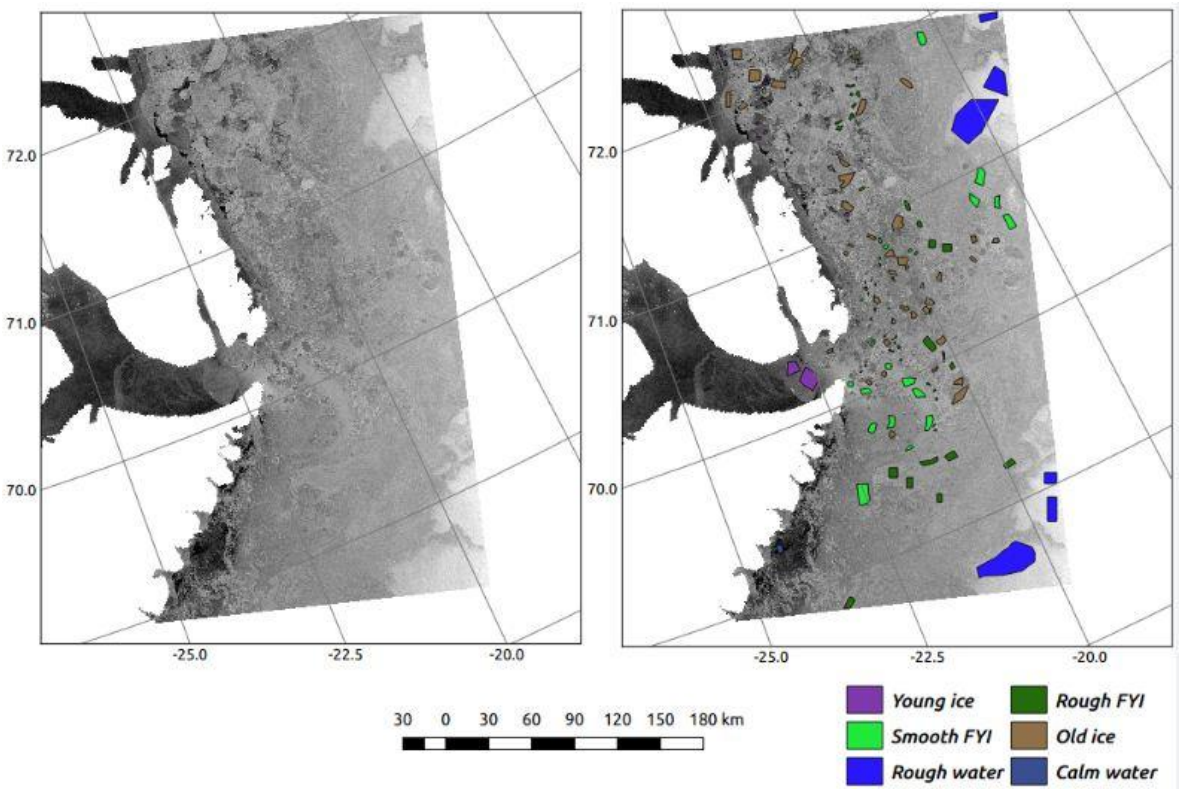

Figure 8.17: SAR image acquisition in May 25 2016 with training data. a) SAR image and b) SAR image with the training data overlaid

Type of the Sea Ice	Number of training data (pixels)
Rough First Year Ice	612207
Smooth First Year Ice	22112
Young Ice	151414
Old Ice	1765776
Rough water	301898
Calm water	301898
Total	**4245131**

Table 8.4: Number of training data for each sea ice type for the scene of May 25 of 2016

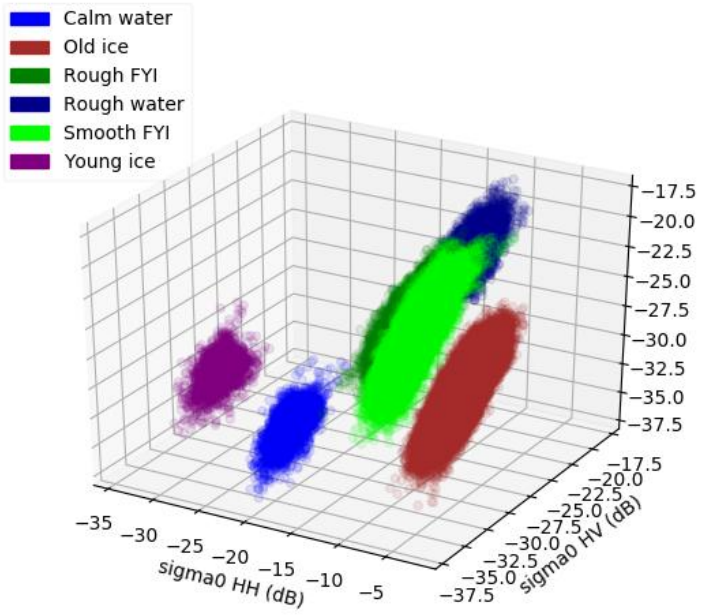

Figure 8.18. Scatter plot of sea ice types for the datasets of May 25 of 2016

For the dataset of May 2016, we can see that FYI contains two subclasses, a) rough FYI and b) smooth FYI. Due to the sea ice deformation occurred in the scene, FYI was broken down into pieces. These ice blokes have been piled up forming a rough surface. It is obvious from the figure 8.18 that young ice, old ice and calm water are perfectly separable. The confusion occurs between rough and smooth FYI where a considerable part of them overlaps. Hence, discriminating rough from the smooth FYI becomes challenging.

8.4 Parameters selection for SVM classifier

The selection of suitable parameter values when training the SVM model is crucial for improving the ability of the model to make accurate predictions. The effectiveness of SVM model depends on the selection of kernel and the parameters C and γ. The C parameter is the penalty term which controls the influence of each support vector and γ defines how constraint we want the model to be.

In order to find the optimum parameters, a method called grid search is implemented in this study. The scikit-learn (Pedregosa *et al, 2011*) open source python library is used to perform a grid search and find the optimum parameters to be used in the SVM model. To perform a complete grid search is not practical as it is very computationally expensive, hence, the parameter values are evaluated over a coarser grid. The parameter values that achieved the highest classification accuracy are chosen.

The figures below illustrates the results of grid search using radial basis function kernel. This type of kernel has been chosen as it is widely accepted that it is the most suitable kernel for mapping complex data. It can be observed from both graphs that by increasing the C and γ values, the accuracy of the classification increases. Choosing a C value 1 and the lowest γ value, the accuracy drops to 85% and 89% for the SAR image of February 2016 and May of 2016 respectively. When C value increases up to 100, the classification accuracy goes above 90% for both SAR datasets. An interesting characteristic that can be noted in the graphs is the rapid linear change in the classification accuracy with increasing of γ value.

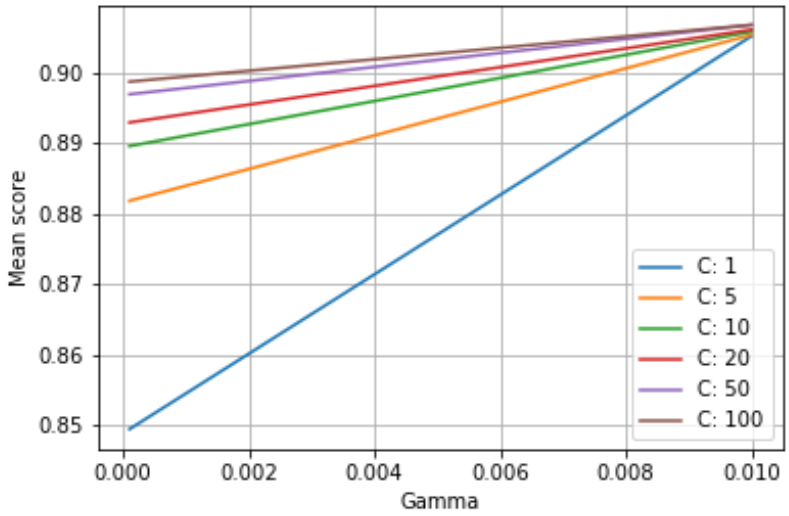

Figure 8.19: Parameters determination (for the SAR image of February 2016) for both C and γ using grid search method

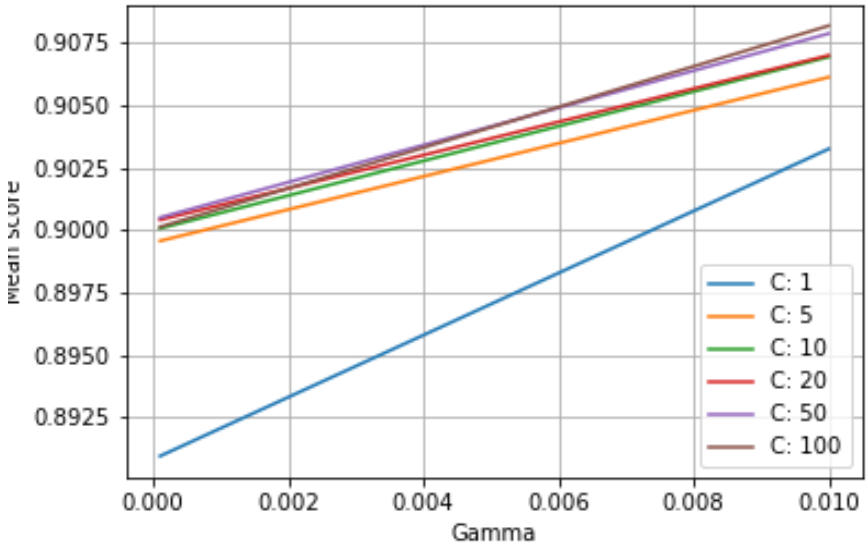

Figure 8.20: Parameters determination (for the SAR image of May 2016) for both C and γ using grid search method

It can be clearly seen that by adjusting the γ parameter appropriately a good classification accuracy can be achieved. Even if a small C value is selected, by increasing the value of γ, we observe a rapid increase in accuracy.

The grid search method has shown that the best classification accuracy for the dataset of February 2016 is achieved with any of the following C values: 20, 50 and 100 and with a γ value of 0.010. On the other hand, for the dataset of May 2016, the best parameter values are found to be between 50 and 100 for C and 0.01 for γ.

Hence, in this study, for the SAR image acquired in February 2016, the values 100 and 0.01 for C and γ parameters have been chosen reaching an accuracy above 90%. Similarly, the same values for C and γ parameters have been chosen for the SAR image acquired in May 2016 reaching an accuracy above 90%. These values that were produced from grid search analysis were used as inputs for the SVM model to perform the classification.

8.5 Texture features selection

In this study, nine texture features were calculated. Given that texture analysis were carried out in both polarization channels (HH and HV) the number of features grow up to 18 and some of them are strongly correlated. If all these features are used by the classifier, it will lead to a confusion, some classes will be overestimated and others will be underestimated and this may lead to higher classification error. On the other hand, including only a few features in the classifier it can lead to a poor classification. Hence, the problem that arises is which features should be included in our classifier for producing a higher accuracy in the classification.

Scikit-learn python library provides a tool where we can investigate which features contribute more than others. The selection procedure was carried out before performing the classification. A set of training regions were used to test which features produced the best results. The figure 8.21 shows the texture features that are the most important (for both datasets) for producing a classification with the smallest error.

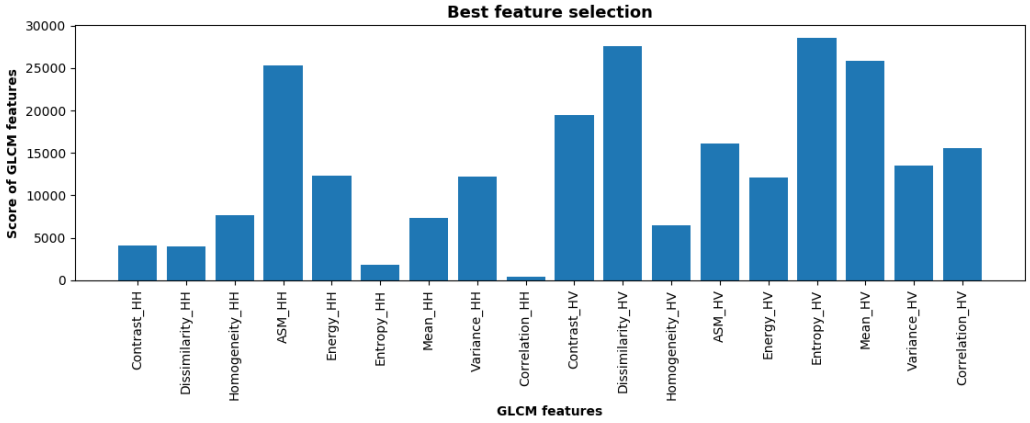

Figure 8.21: Texture features contribution. The GLCM features are plotted on the x-axis and the score they have achieve is plotted on the y-axis.

The GLCM features with the highest score are those that are more important than the others. By looking at the figure, we can immediately see which features scored the lowest and hence, are excluded. These features are the contrast, dissimilarity, entropy and correlation in HH polarization channel. GLCM features that achieve the highest score are dissimilarity, entropy and the mean in HV polarization channel.

For this research, eight features were selected for the classification. These features are the contrast dissimilarity, entropy, ASM and the mean from HV polarization and ASM, energy and variance from HH polarization.

8.6 Sea Ice classification results

The sea ice classification maps for both SAR scenes are shown in the figures below. The classification results are accompanied by classification report and confusion matrix. The results were compared with the sea ice charts of DMI which were produced exactly the same date with the acquisition of the SAR images. The SVM method one versus one was used to perform the sea ice classification. The colors for each ice class were selected according to World Meteorological Organization.

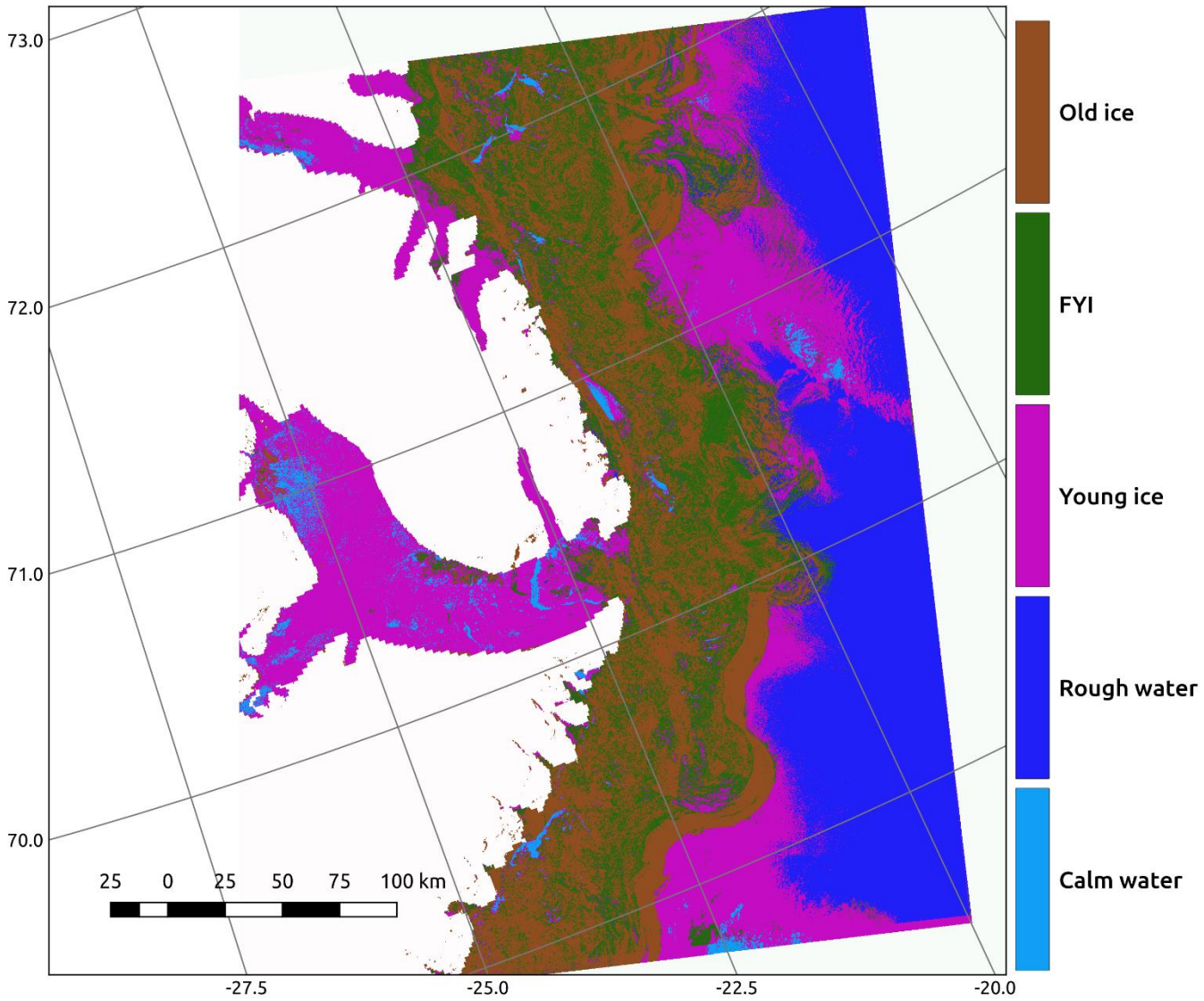

Figure 8.22: Sea ice classification map for February of 2016

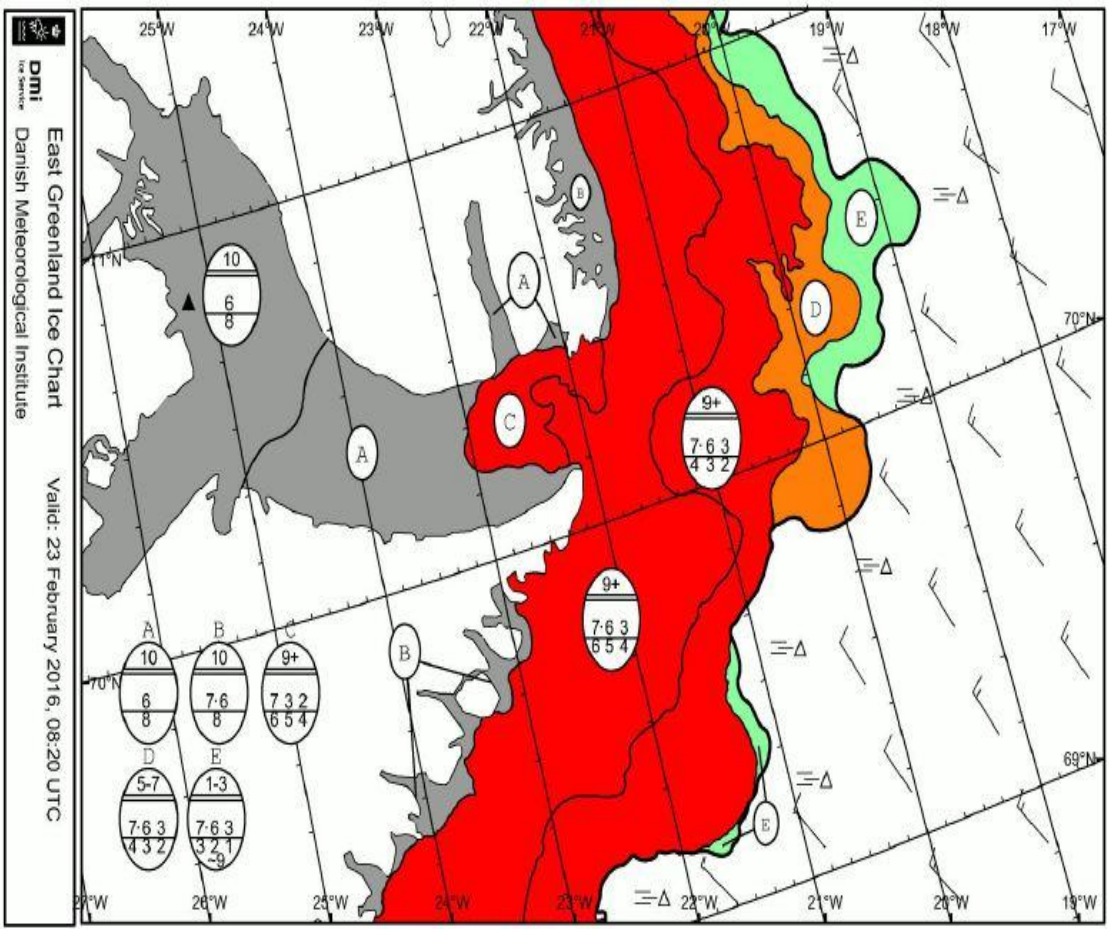

Figure 8.23: Validation data for February of 2016 by DMI

	Precision	Recall	F1-score	Support
Old ice	0.83	0.74	0.79	12655
FYI	0.65	0.72	0.69	185881
Young ice	0.80	0.89	0.84	63562
Rough water	1.00	1.00	1.00	451054
Calm water	0.96	1.00	0.98	12655
Avg / total	**0.91**	**0.91**	**0.91**	**1330524**

Table 8.5: Classification report for the classification map produced in February 23 of 2016

	Old ice	FYI	Young ice	Rough water	Calm water
Old ice	189819	64646	441	144	0
FYI	38390	134522	12641	223	105
Young ice	208	6219	56515	264	356
Rough water	32	662	1362	448998	0
Calm water	0	0	51	0	12604

Table 8.6: Confusion matrix for the classification map produced in February 23 of 2016

The classification map shown in figure 8.22 consists of five sea ice classes (Old ice, FYI, young ice, rough water and calm water). The class water was divided into two classes, calm and rough water. Due to strong winds, sea acquires high waves which produce a very strong backscatter signal. The young ice category which is 30cm thick does not significantly affect the navigation of the vessels, especially the big ships with ice breakers.

The greatest danger for ships is when navigating though old ice and FYI. These two sea ice types reduce the speed of icebreaker and reduce the sailing safety. The deformed FYI becomes even more dangerous and can cause a significant damage to any ship. Deformed FYI in February datasets is not present.

The validation data in figure 8.23 is displayed using the 'egg code' system to describe the sea ice types (detailed description about the egg code system is given in the appendices). The different colors displayed on the ice chart correspond to different sea ice concentration. The red color on the map suggests that the sea ice concentration is very high (above 90%). Also, the validation data suggests that there are three sea ice classes dominating this area which correspond to old ice (denoted with the number 7. in the egg code), FYI (denoted with the number 6 in the egg code) and young ice (denoted with the number 3 in the egg code).

Looking at the classification results, the area with the high sea ice concentration is dominated by old ice and FYI, while the young ice is present in areas of lower ice concentration. However, we can notice some openings in the sea ice shown in light blue color (these cracks / leads contain water). The backscatter magnitude of leads is lower than 19dB. The algorithm has identified all the cracks in sea ice with a precision of 96%. This indicates that the algorithm is more capable of indicating more details (compared to DMI ice chart) in the high concentration sea ice zone.

Some classification errors can be found at the ice - water boundary (upper right and bottom right) where young ice is present with a curved shape. Due to strong winds, newly formed sea ice (such as young ice) is moving around taking a curve shape as shown in the classification map. This part of young ice was misclassified as old ice. This misclassification can be explained by the appearance of frost flowers. Frost flowers are ice crystals that can be found on young ice during winter. They are formed when the air temperature is much lower than the underlying ice. The backscatter coefficient can be severely affected by the presence of frost flowers which can reach the backscatter coefficient of old ice. The backscatter magnitude of young ice covered by from flowers

by increase up to 8dB. The most significant classification errors occurs at the ice – water boundary zone due to the dynamic nature of sea ice and wind speeds.

A difference between DMI manual sea ice chart and the SVM classification can be detected at the elongated area on the left extended beyond 25 degrees. The DMI ice chart shows that this areas is covered by FYI compared to our classification algorithm that classified this zone as young ice. The thickness of young ice is below 30cm (a very low backscatter coefficient is produced) while the thickness of FYI (which can be divided in many sub-classes) varies between 30 and 120cm. The backscatter coefficient in this zone is between -23 and -17dB. Backscatter coefficient tables for C-band during winter were produced by Shokr and Sinha 2015 which show that the backscatter intensity for FYI lies between -13.5 and -11dB. Hence, with the SVM classifier and the aid of texture analysis, this zone was classified as young ice.

Classification report and confusion matrix have been calculated for each sea ice types. The overall classification accuracy was 91%. The rough water and calm water classes have been perfectly classified and discriminated from the other sea ice classes with a precision of 100% and 96% respectively as it can be seen at the classification report. Also, old ice and young ice have been successfully discriminated achieving an accuracy above 80%.

In the confusion matrix, we can see the number of misclassified pixels for each sea ice type. The diagonal shows the number of correct pixel classification for each sea ice type. The off diagonal values show the number of misclassified pixels.

Calm water has been classified almost perfectly with 51 pixels misclassified as young ice. The biggest confusion occurred between FYI and Old ice. For the old ice, 64646 pixels were misclassified as FYI. For the FYI, 38390 pixels were misclassified as old ice. The backscatter signature of these two sea ice types is of a few dBs different with a similar texture. Hence, this is the reason for having many misclassified pixels between old ice and FYI.

Below, the classification results for the datasets of May 2016 are displayed.

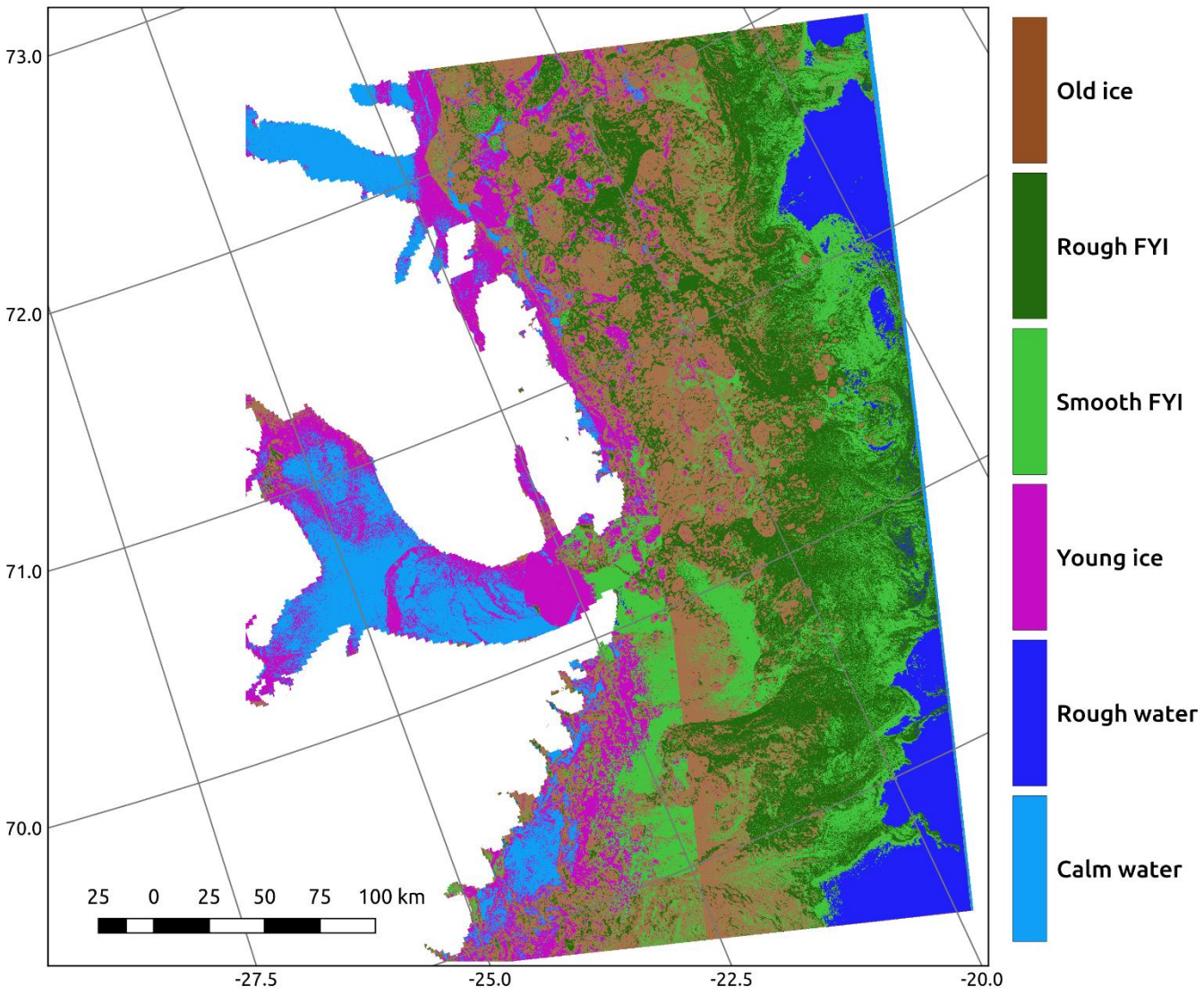

Figure 8.24: Sea ice classification map for May of 2016

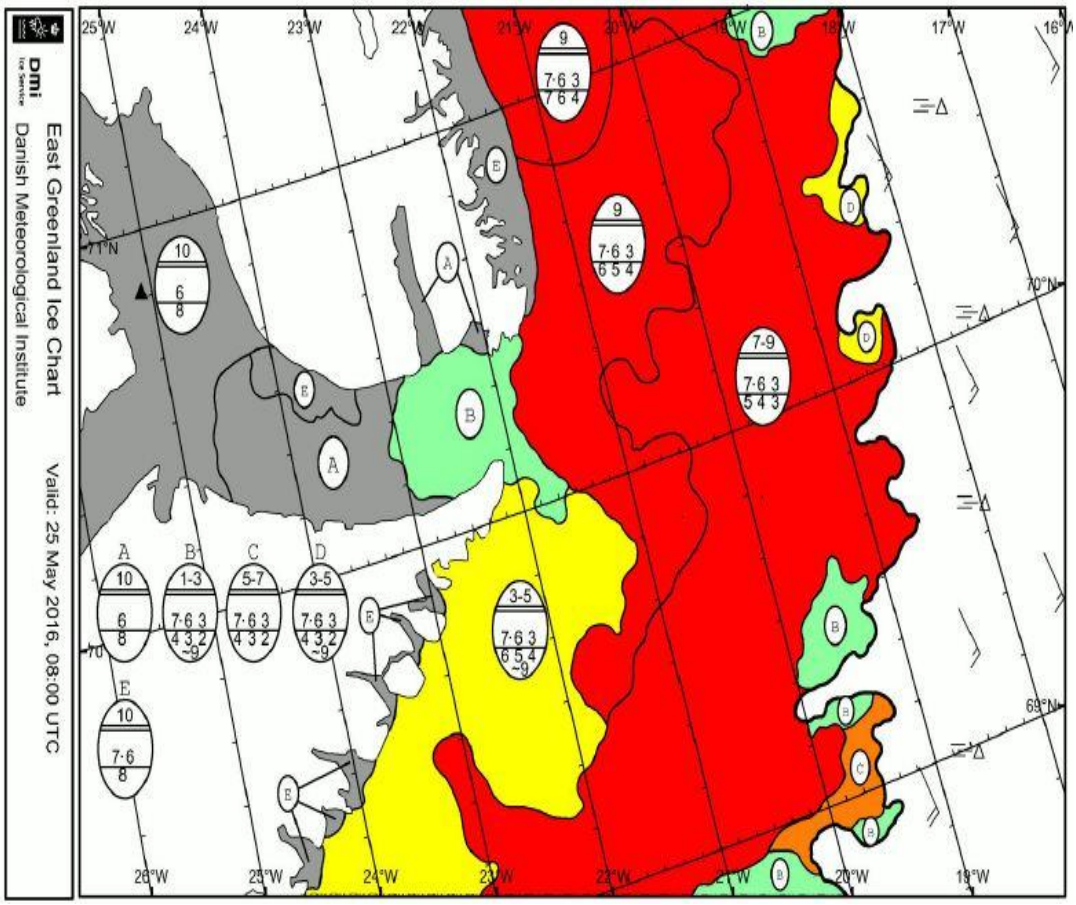

Figure 8.25: Validation data for May of 2016 by DMI

	Precision	Recall	F1 – score	Support
Old ice	0.82	0.70	0.76	612207
Rough FYI	0.60	0.79	0.68	301898
Smooth FYI	0.82	0.79	0.81	379252
Young ice	0.97	0.99	0.98	151414
Rough water	0.99	1.00	1.00	212021
Calm water	1.00	1.00	1.00	22112
Avg / total	**0.91**	**0.90**	**0.90**	**3372020**

Table 8.7: Classification report for the classification map produced in May 25 of 2016

	Old ice	Rough FYI	Smooth FYI	Young ice	Rough water	Calm water
Old ice	429299	127207	51220	3285	1196	0
Rough FYI	50411	238805	12665	0	17	0
Smooth FYI	42644	34554	300222	1522	310	0
Young ice	376	0	372	150633	0	33
Rough water	28	84	174	0	211735	174
Calm water	0	0	0	11	0	22101

Table 8.8: Confusion matrix for the classification map produced in May 25 of 2016

The classification results for the SAR scene acquired in May 2016 consists of six classes. The melting onset in May change the backscatter energy from the sea ice and the discrimination of sea ice types becomes more challenging. The water class was divided into calm and rough water. Rough weather conditions prevailed during when the image was acquired. Young ice is present on this scene. Old ice and FYI are the sea ice types that mostly cover the SAR scene. The FYI was divided into smooth and rough (deformed) FYI. Deformed FYI is the most dangerous ice type for ship navigation due to its rough texture. Navigating through deformed FYI is very challenging even for big ships with icebreakers.

The validation data is shown in figure 8.25. The sea ice concentration differs across the scene. Sea ice concentration is mainly high (above 90% shown in red) on the upper part while on the bottom the sea ice concentration decreases (60% shown in yellow). The sea ice types identified by DMI are the following. Old ice (denoted with the number 7· in the egg code), FYI (denoted with the number 6 in the egg code) and young ice (denoted with the number 3 in the egg code).

Old ice have been successfully identified. The old ice can be discriminated by its high backscatter signature and rounded shape. All the big sea ice floes were identified and successfully classified as old ice. The majority of the old ice is located at the upper part of the SAR image. Deformed FYI which is the most hazardous sea ice type was identified. Most of the deformed FYI occurred between old ice floes. Hence, navigating though the big ice floes where deformed FYI is present should be avoided. The most challenging part is the discrimination between old ice and deformed FYI due to the similar backscatter. Young ice is scarce and it is present mainly along the coast.

Residual noise effects in HV polarization (after thermal noise suppression) in the SAR image are still present. The residuals of the thermal noise can be seen at the classified image beam boundaries which affect the classification.

Classification report and confusion matrix have been calculated for each sea ice types. The overall classification accuracy was 91%. The classification report shows that rough

water and calm water classes have been precisely classified from the other sea ice classes with a precision of 99% and 100% respectively. Old ice floes were identified in the SAR scene with a precision of 82%. The rough texture and strong backscatter of old ice due to volume scattering helps in discriminating it from the other ice types. Difficulties in discrimination deformed FYI can be seen in classification report. The precision achieved for this ice type is 60%. On the other hand, the classification of smooth FYI was more successful reaching a precision of 82%.

The confusion matrix is more intuitive than classification report because we can see the number of pixels that were misclassified as a different ice type. Some pixels of the old ice were misclassified as FYI and young ice. The deformed FYI produces strong backscatter equivalent to the backscatter of old ice, hence the confusion. On the other hand, we can observe some confusion between old ice and young ice. Due to ice melting, a common feature that is observed in old ice is the appearance of a melt pond on top of the ice floe. The melt ponds consist of fresh water and due to their smooth surface, the backscatter intensity is as low as that of the young ice. This explains the misclassification. A confusion between deformed and smooth FYI is expected due to their similar backscatter coefficient. Also, due to the face that the backscatter coefficient of deformed FYI is bit higher than that of smooth ice, we observe some pixels of deformed ice were classified as old ice. The water classes were perfectly classified due to the very low backscatter coefficient of calm water (30-29 dB) and very high backscatter coefficient of rough water (11-9 dB).

Overall, there is a strong agreement between the classification results and the validation data. All the hazardous for ships sea ice types have been successfully identified and classified.

9 Conclusion and suggestions

9.1 Conclusion

In this study, an approach to sea ice classification combining both backscatter and texture analysis is presented. The SVM classifier and GLCM texture analysis with nine texture statistics are used.

Before performing sea ice classification, the SAR images are pre-processed. One of the most important steps is to remove the thermal noise from the SAR images. The HV polarization channel suffers from thermal noise which might affect the classification results. We need to note that despite the fact that the thermal noise removal was applied to the datasets, some residuals are still present.

GLCM texture analysis were performed with the appropriate parameters. The nine GLCM features that were calculated for both HH and HV polarizations are the GLCM mean, GLCM variance, correlation, homogeneity, entropy, energy, angular second moment, contrast and dissimilarity.

SVM classification with the help of texture analysis was performed. For better classification results, the SVM model was optimized using grid search analysis. Grid search analysis conducted for both datasets produced the optimum hyper-parameters for the SVM model. The value of 100 for C and 0.01 for γ were chosen for both datasets achieving an accuracy of 91%

In this study, we showed that the most hazardous for ships sea ice types such as deformed FYI and old ice were successfully discriminated in the SAR imageries. A precision of 83% and 65% was achieved in discriminating the old ice and FYI respectively for the SAR scene of February in 2016. On the other hand, a precision of 82% and 60% was achieved in discriminating the old ice and deformed FYI respectively for the SAR scene of May in 2016.

Comparing the two SAR scenes, we can see how the sea ice changes between winters and spring period. In freeze up period, the sea ice concentration is high and the discrimination between old ice and FYI is easier due to the high contrast between these two ice types. The SAR scene in February 2016 mainly consists of old ice and FYI with a few leads (that contain water) amongst the sea ice. On the other hand, the SAR scene acquired in May 2016, the ice concentration decreases and the old ice that does not melt completely acquires a rounded shape. Sea ice deformation amongst the old ice floes is observed. The discrimination between old ice and FYI is more challenging. As sea ice melts, a transition from FYI to young ice is happening. Hence, young ice can be seen amongst the old ice floes.

9.2 Suggestions

In this research, supervised classification algorithm was used which requires priori knowledge of sea ice classes. On the other hand, unsupervised classification has not been explored in the context of this study. Unsupervised classification methods classify each pixel based on based on spectral information without having priori knowledge of the sea ice classes. It was shown by Chapelle, et.all (2006) that combining both supervised and unsupervised classification methods, in many cases, it improve the classification results.

Another important factor that can potentially improve the classification accuracy is the sea ice concentration layer. Sea ice concentration is the percentage of sea ice in a given area. For instance, new ice has low sea ice concentration because it is usually composed of small ice floes scattered around which surrounded by open water. On the contrary, the sea ice concentration of old ice is very high. Therefore, sea ice concentration of new and old ice can assist in discriminating between these two sea ice types.

The wavelength of the microwave radiation plays an important role on sea ice observations. One of the datasets used in this study were captured in May of 2016 which is the early melt onset for sea ice. When the melt onset starts, the sea ice floes get flooded with sea water which results in an increase of the dielectric constant. As the dielectric

constant of sea ice increases, the penetration of the microwave decreases. Hence, in that case, C-band is not the ideal one for sea ice observations as its frequency is relatively high. On the other hand, longer wavelengths (such as L-band) are preferred in such cases. Long wavelength penetrate deeper to the material and interact with the sea ice to give a stronger backscatter.

The backscatter energy from the surface of the earth is proportional to the roughness of the material being observed. In case of SENNTINEL-1, the SAR image suffers from thermal noise especially in areas of low backscatter. These areas are of higher intensity values not because of the surface roughness but due to thermal noise. Hence, thermal noise removal is a very important step. If thermal noise is present, then it can severely affect the classification results. SNAP toolbox provides a method for minimizing the thermal noise but it does not remove it completely. After minimizing the thermal noise, some residuals are still present on the SAR image. Hence, a better methodology for removing the thermal noise is necessary.

References

Barber, D.G. and LeDrew, E.F. (1989). Multivariate analysis of texture statistics for SAR sea ice discrimination. In Geoscience and Remote Sensing Symposium, 1989. IGARSS'89. 12th Canadian Symposium on Remote Sensing. (2), pp. 759-762

Barber, D.G. and LeDrew, E.F. (1991). SAR sea ice discrimination using texture statistics: A multivariate approach. Photogrammetric Engineering and Remote Sensing, 57(4), pp.385-395.

Bobylev, L.P., Johannessen, O.M., Sandven, S. and Melentyev, V.V. (1996). Icewatch - Ice SAR Monitoring of the Northern Sea Route. In *The* Sixth International Offshore and Polar Engineering Conference. International Society of Offshore and Polar Engineers

Bredow, J. (1989). A laboratory investigation into microwave backscattering from sea ice, PhD thesis, Kansas University of Kansas. [Online] Available from: http://ntrs.nasa.gov/archive/nasa/casi.ntrs.nasa.gov/19900016074.pdf [Accessed 26 October 2015]

Buch, E. (1998). Oceanographic investigations in West Greenland Waters, 1981 - 1997. Sci. Counc. Res. Doc. NAFO, (98), p.18. [Online] Available from: http://archive.nafo.int/open/sc/1998/scr-98-024.pdf [Accessed 20 November 2015] Petersen, H. (1948). The Danish Meteorological Service in Greenland. ARCTIC, 1(1), p 27-33

Buch, E. (2000). Air-Sea-Ice Conditions off Southwest Greenland, 1981-97. Journal of Northwest Atlantic Fishery Science., 26, p.123-136.

Buch, E. (2000). A monograph on the physical oceanography of the Greenland waters. Scientific report, Danish Meteorological Institute.

Campbell, J. and Wynne, R.H. (1996). Introduction to remote sensing. New York: Guilford Press.

Chapelle, O., Bernhard, S and Alexander, Z (2006). Semi-Supervised Learning, Massachusetts: MIT press

Cheek, J. (2009). The emergence of Polar View as a major player in Earth observation services – Science Poles: polar science magazine. [Online] Sciencepoles.org. Available from: http://www.sciencepoles.org/interview/the-emergence-of-polar-view-as-a-major-player-in-earth-observation-services [Accessed 30 Oct. 2015].

Clausi, D. (2001). Comparison and fusion of co- occurrence, Gabor and MRF texture features for classification of SAR sea- ice imagery. Atmosphere-Ocean, 39(3), pp.183-194.

Clausi, D.A (1996). Texture segmentation of SAR Sea Ice Imagery, PhD thesis, University of Waterloo, Ontario. [Online] Available from: https://uwaterloo.ca/vision-image-processing-lab/sites/ca.vision-image-processing lab/files/uploads/files/texture_segmentation_of_sar_sea_ice_imagery.pdf [Accessed 2 February 2016]

Clausi, D.A. and Deng, H. (2003). Operational segmentation and classification of SAR Sea ice imagery. In Advances in Techniques for Analysis of Remotely Sensed Data, 2003 IEEE Workshop, pp. 268-275

Clausi, D.A. (2002). An analysis of co-occurrence texture statistics as a function of grey level quantization. Can. J. of remote sensing, 28(1), p.45-62.

Coelho, L.P. (2013). Mahotas: Open source software for scriptable computer vision. Journal of Open Research Software 1(1):e3, DOI: http://dx.doi.org/10.5334/jors.ac

Comiso, J. (2010). Polar Oceans from Space. New York: Springer.

Curlander, J. and McDonough, R. (1991). Synthetic aperture radar. New York: John Wiley & Sons.

De Leeuw, M.R. and de Carvalho, L.M.T (2009). Performance evaluation of several adaptive speckle filters for SAR imaging. Anais XIV Simpósio Brasileiro de Sensoriamento Remoto, pp.7299-7305

Dmi.dk. (2016). East Greenland: DMI. [Online] Available from: http://www.dmi.dk/en/hav/groenland-og-arktis/iskort/oestgroenland/ [Accessed 4 Feb. 2016].

Dmi.dk. (2015). Introduction to DMI: DMI. [Online] Available from: http://www.dmi.dk/en/about/ [Accessed 4 Feb. 2016].

Drinkwater, M.R., Perovich, D.K., Gow, A.J., Weeks, W.F. and Tucker, W.B. (1992). Physical properties of sea ice relevant to remote sensing. In. Carcey, F.D. ed. Microwave remote sensing of sea ice, Geophysical monograph 68, pp.9-28.

Dierking, W., Garrity, C. and Ramseier, R.O. (1994). Interpretation of radar signatures observed in SAR images of ice island T-3 by means of backscatter modelling. EARSeL Advances in Remote Sensing. 3(2), pp.31-43.

Drinkwater, M.R. and Carsey, F.D. (1991). Observations of the late-summer to fall sea ice transition with the 14.6 GHz SEASAT Scatterometer. Geoscience and Remote Sensing Symposium, 1991. IGARSS '91. Remote Sensing: Global Monitoring for Earth Management, International, pp 1597-1600

El-Darymli, K., McGuire, P., Gill, E., Power, D. and Moloney, C. (2014) Understanding the significance of radiometric calibration for synthetic aperture radar imagery. Electrical and Computer Engineering (CCECE), 2014 IEEE 27th Canadian Conference, IEEE, p. 1-6.

e-Krishi Shiksha. (2016). RS&GA: Lesson 15 Radar Systems. [Online] Available from: http://ecoursesonline.iasri.res.in/mod/page/view.php?id=2068 [Accessed 13 Dec. 2015].

Earth.esa.int. (2016). ICEWATCH – Real-time Sea Ice monitoring of the Northern sea route using satellite radar technology. [Online] Available from: https://earth.esa.int/workshops/ers97/papers/sandven2/index-2.html [Accessed 2 Nov. 2015]

Ezraty, R. (2002). Detection and monitoring of new-ice in the East Greenland Sea using the SeaWinds scatterometer. Journal of Ocean University of Qingdao, 1(2), pp.109-118.

Ferguson, J.R. (2007) Using the Grey level Co-Occurrence Matrix to Segment and Classify Radar Imagery, PhD thesis, University of Nevada, Reno. [Online] Available from:http://search.proquest.com.ezproxy.is.ed.ac.uk/docview/304843719/[Accessed 01November 2016]

Fetterer, F., Gineris, D. and Kwok, R. (1994). Sea ice type maps from Alaska Synthetic Aperture Radar Facility imagery: An assessment. Journal of Geophysics. Research, 99(C11), p.22443.

Geldsetzer, T. and Yackel, J. (2009). Sea ice type and open water discrimination using dual co-polarized C-band SAR. Canadian Journal of Remote Sensing, 35(1), pp.73-84.

Harrington, P. (2012). Machine learning in action (Vol. 5). Greenwich, CT: Manning.

Hallikainen, M. and Winebrenner, D. P. (1992). The Physical Basis for Sea Ice Remote Sensing. In Carsey, F.D., ed. Microwave Remote Sensing of Sea Ice. Washington, D. C: American Geophysical Union

Haralick, R.M. and Shanmugam, K. (1973). Textural features for image classification. IEEE Transactions on systems, man, and cybernetics. (6), pp.610-621.

Haskell, T., Mahoney, A., Langhorne, P., Williams, M. and Gough, A. (2012). Sea ice salinity and structure: A winter time series of salinity and its distribution. Journal of Geophysical Research, 117(C3), pp 1-12.

Herranz, M and Tita, J (2013). PyRadar: Open Source Scientific Tool for Python. http://pyradar-tools.readthedocs.io/en/latest/index.html

Hibler, W.D. (2001) Sea ice fracturing on the large scale. Engineering Fracture Mechanics, 68(17-18), p 2013-2043

Hinkler, J. (2005). From digital cameras to large scale sea-ice dynamics. PhD thesis. Denmark: University of Copenhagen

Holt, B., Kwok, R. and Rignot, E. (1989). Ice classification algorithm development and verification for the Alaska SAR Facility using aircraft imagery. Jet propulsion laboratory, California Institute of Technology, IEEE, pp 751-754

International Marine Organization (2009). Precautions in using navigational charts in Greenland waters. [Online] Available from: http://www.soefartsstyrelsen.dk/SikkerhedTilSoes/Arktis/SejladsGroenland/Documents/6Precutions%20in%20using%20%20navigational%20charts%20in%20Greenland%20waters.pdf [Accessed 10 Feb. 2016].

Joshi, R. and Garg, R.D. (2012). Pre-processing of terrasar-x data for speckle removal: an approach for performance evaluation. Journal of the Indian Society of Remote Sensing, 40(3), pp.371-377.

James, G., Witten, D., Hastie, T. and Tibshirani, R. (2013). An introduction to statistical learning (Vol. 6). New York: springer.

Jackson, C.R and McCandless, S.W. (2004). Principles of Synthetic Aperture Radar. SAR Marines User's manual, pp 1-23

Japan Association of Remote Sensing. (1999). Remote sensing note. [Online] Available from: http://wtlab.iis.u-tokyo.ac.jp/~wataru/lecture/rsgis/rsnote/contents.htm [Accessed 13 Aug. 2016]

Johannessen, O. and Johannessen, O. (2007). Remote sensing of Sea Ice in the Northern Sea Route. Berlin: Springer.

Karvonen, J. (2006). Compaction of C-Band Synthetic Aperture Radar based Sea Ice information of navigation in the Baltic Sea, PhD thesis, Helsinki University of technology. [Online] Available from: http://lib.tkk.fi/Diss/2006/isbn9512284723/isbn9512284723.pdf [accessed 26 October 2015]

Knippers, R (2009) Geographic aspect of mapping: Map projections. [Online] Available from: http://kartoweb.itc.nl/geometrics/map%20projections/mappro.html

Kwok, R., Nghiem, S. and Thomsen, B. (1998). Polarimetric C-Band SAR Observations of Sea Ice in the Greenland Sea. IEEE International Geoscience and Remote Sensing Symposium. p.2502 – 2504. [Online]. Available from: http://orbit.dtu.dk/files/4364874/Thomsen.pdf [Accessed 15 Nov. 2015].

Kwok, R. and Cunningham, G.F. (1994). Backscatter characteristics of the winter ice cover in the Beaufort Sea. Journal of Geophysical Research, 99, pp.7787-7787.

Lee, J.S. (1981). Speckle analysis and smoothing of synthetic aperture radar images. Computer graphics and image processing, 17(1), pp.24-32.

Lee, J.S., Wen, J.H., Ainsworth, T.L., Chen, K.S. and Chen, A.J. (2009). Improved sigma filter for speckle filtering of SAR imagery. IEEE Transactions on Geoscience and Remote Sensing, 47(1), pp.202-213.

Li, J. and Yang, X. (2015). Monitoring and modeling of global changes. Netherlands: Springer remote sensing/Photogrammetry.

Lundhaug, M. (2002). Sea ice studies in the Northen Sea route by use of Synthetic Aperture Radar. PhD. Telemark. University of Telemark. [Online] Available from: http://www.divaportal.org/smash/get/diva2:125934/FULLTEXT01.pdf [accessed 26 October 2015]

Lusch, D.P. (1999). Introduction to microwave remote sensing. Center for remote sensing and geographic information science, Michigan University

Makynen, M. (2007). Investigation of the microwave signatures of the Baltic Sea ice. Ph.D. Helsinki University of Technology. [Online] Available from: http://lib.tkk.fi/Diss/2007/isbn9789512287413/isbn9789512287413.pdf [Accessed 10 March 2016]

Mascarenhas, N.D. (1997). An overview of speckle noise filtering in SAR images. Image Processing Techniques, First Latino-American Seminar on Radar Remote Sensing, p 71-79

Massom, R. and Lubin, D. (2006). Polar remote sensing (Vol. 2). Chichester: Springer.

Melita, K (2000) Understanding map projections. New York, Redlands: Environmental System Research Institute. [Online] Available: http://kartoweb.itc.nl/geometrics/map%20projections/mappro.html

Miranda, N. and Meadows, P.J. (2015) Radiometric Calibration of S-1 Level-1 Products Generated by the S-1 IPF. Technical note. [Online] Available from: https://sentinel.esa.int/documents/247904/685163/S1-Radiometric-Calibration-V1.0.pdf

Onstott, R. G. (1992) SAR and Scatterometer Signatures of Sea Ice, in Carsey, F.D., ed. Microwave Remote Sensing of Sea Ice. Washington, D. C: American Geophysical Union

Otukei, J.R., Blaschke, T. and Collins, M. (2012) A Decision Tree Approach for Identifying the Optimum Window Size for Extracting Texture Features from TerraSAR-X Data, Herbert Wichmann Verlag, pp 466-474

Pathak, V. and Dikshit, O. (2010). A new approach for finding an appropriate combination of texture parameters for classification. *Geocarto International, 25*(4), pp.295-313.

Pedregosa, F., Varoquaux, G., Gramfort, A., Michel, V., Thirion, B., Grisel, O., Blondel, M., Prettenhofer, P., Weiss, R., Dubourg, V., Vanderplas, J., Passos, A., Cournapeau,

D., Brucher, M., Perrot, M., Duchesnay, E (2011). Scikit-learn: Machine Learning in Python, Journal of Machine Learning Research, pp. 2825-2830

Pedersen, L.T and Skrirer, H. (1995). Polarimetric signatures of Sea Ice in the Greenland Sea. International Geoscience and Remote Sensing Symposium Proceeding, 3, pp1792 – 1794

Pedersen, L.T., Saldo, R. and Fenger-Nielsen, R. (2015). Sentinel-1 results: Sea ice operational monitoring. Proceedings of Igarss 2015.

Pedeersen, S.A., Madsen, J and Dyhr-Nielsen, M. (2004). Arctic Greenland East Greenland Shelf West Greenland Shelf: GIWA Regional assessments 1b, 15 and 16. Sweden. University of Kalman. [Online] Available from: http://www.unep.org/dewa/giwa/areas/reports/1b_15_16/giwa_regional_assessment_1b_15_16.pdf

Piantanida,R., Hajduch,G., Poullaouec,J. (2016) SENTINEL 1 level 1 detailed algorithm definition, ESA-MDA. [Online] Available from: https://sentinel.esa.int/documents/247904/1877131/Sentinel-1-Level-1-Detailed-Algorithm-Definition

Polar view. (2010). Polar view 2005 – 2009: Final report. [Online] Available from: http://www.polarview.org/wp-content/uploads/2015/02/polar-view-2005-2009-final-report.pdf

Pratola, C. (2013). Automatic characterization of sub-urban environments by using VHR X-band COSMO-SkyMed images. PhD thesis, University of Roma. [Online] Available from: https://pdfs.semanticscholar.org/41c2/d0fd6c6a7d3826c67a322cd689ae24fe8056.pdf [Accessed 10 March 2017]

Qiu, F., Berglund, J., Jensen, J.R., Thakkar, P. and Ren, D (2004). Speckle noise reduction in SAR imagery using a local adaptive median filter. GIScience & Remote Sensing, 41(3), pp.244-266.

Rees, G. (2006). *Remote sensing of snow and ice*. Boca Raton: Taylor & Francis.

Robert, M., Haralick, R., Shanmugam, K. and Dinstein, I. (1973). Textural Features for Image Classification. IEEE Transactions on Systems, Man and Cybernetics, 3(6), pp.610-621.

Sandven, S., Dierking, W., Le Bras, J.Y., Heygster, G., Wadhams, P. and Dinesen, F. (2011). Sea Ice Downstream Services for Arctic and Antarctic Users and Stakeholders. SIDARUS summary paper. [Online] Available from: https://sidarus.nersc.no/sites/sidarus.nersc.no/files/SIDARUS-paper.pdf [Accessed 01 Feb. 2016].

Satyanarayana, C.H. and Anuradha, S. (2013). A Review of Recent Texture Classification: Methods. IOSR Journal of Computer engineering, 14(1), p.54-60.

Satyanarayana, C.H. and Anuradha, S. (2013). A Review of Recent Texture Classification: Methods. IOSR-JCE, 14(1), p.54-60.

Schmith, T. and Hansen, C. (2003). Fram Strait ice export during the nineteenth and twentieth centuries reconstructed from a multiyear sea ice index from southwestern Greenland. Journal of Climate, 16(16), p.2782-2791.

Scheuchi, B., Caves, R., Flett, D., De Abreu, R., Arkett, M. and Cumming, I. (2005). The potential of cross-polarization information for operational sea ice monitoring. In Envisat & ERS Symposium (Vol. 572).

Shokr, M.E. (1989) Texture measures for sea-ice classification from radar images. In Geoscience and Remote Sensing Symposium IGARSS'89. 12th Canadian Symposium on Remote Sensing. 1989 International IEEE. (2), pp. 763-768.

Shokr, M. and Sinha, N. (1994). Arctic Sea Ice Microstructure Observations Relevant to Microwave Scattering. ARCTIC, 47(3).

Shokr, M. and Sinha, N. (2015). Sea ice: Physics and remote sensing. Hoboken. NJ: John Wiley & Sons.

Shuchman, R.A., Wackerman, C.C., Maffett, A.L., Onstott, R.G. and Sutherland, L.L. (1989). The discrimination of sea ice types using SAR backscatter statistics, radar science laboratory.
pp. 381-385

Shokr, M.E., (1991). Evaluation of second-order texture parameters for sea ice classification from radar images. Journal of Geophysical Research: Oceans, 96(C6), pp.10625-10640.

Soh, L.K. and Tsatsoulis, C. (1999). Texture analysis of SAR sea ice imagery using gray level co-occurrence matrices. IEEE Transactions on geoscience and remote sensing, 37(2), pp.780-795.

Skou, N. and Pedersen, L. (1984). Microwave signatures of the sea ice in the east Greenland current. IEEE Journal of Oceanic Engineering, 9(5), pp.339-343.

Stoffels, M.M. and Wackerbauer, R. (2012). Albedo parametrization and reversibility of sea ice decay. Nonlin. Processes Geophys., 19(1), pp.81-94.

SNAP - ESA Sentinel Application Platform v5.0, http://step.esa.int

Tonboe, R. and Toudal, L. (2005). Classification of new-ice in the Greenland Sea using Satellite SSM/I radiometer and SeaWinds scatterometer data and comparison with ice model. Remote Sensing of Environment, 97(3), pp.277-287.

Tonboe, R. and Ezraty, R.E. (2002). Monitoring of new-ice in Greenland waters. In Geoscience and Remote Sensing Symposium, 2002. IGARSS'02. 2002 International IEEE (3), pp. 1932-1934).

Topouzelis, K., Singha, S and Kitsiou, D (2016). Incidence angle normalization of Widw Swath SAR data for oceanographic applications, Open Geoscience, 8(1), pp 450-464

Van der Sanden, J. (2004). Anticipated applications potential of RADARSAT-2 data. *Canadian Journal of Remote Sensing*, 30(3), pp.369-379.

Vanzyl, J and Kim, Y. (2010). Synthetic Aperture Radar polarimetry. California Institute of Technology. Jet Propulsion Laboratory

Witten, I.H., Frank, E., Hall, M.A. and Pal, C.J. (2016). *Data Mining: Practical machine learning tools and techniques*. Morgan Kaufmann

Wolff, C. (2014). Radar basics – Side looking airborne radar. [Online] Available from: http://www.radartutorial.eu/20.airborne/ab06.en.html

Woodhouse, I.H. (2006) Introduction to Microwave Remote Sensing, New York, CRC press

World Meteorological Organization. (1970). Sea-Ice Nomenclature. [Online] Available from:http://www.jcomm.info/index.php?option=com_oe&task=viewDocumentRecord&docID=14598 [Accessed 21 Nov. 2015]

Xue, X and Wang, Z. (2014). Multi-class Support Vector Machine. In Guo, G and Ma, Y. ed. *Support vector machines applications,* pp. 166. New York: Springer.

Zakhvatkina, N., Alexandrov, V., Johannessen, O., Sandven, S. and Frolov, I. (2013). Classification of Sea Ice Types in ENVISAT Synthetic Aperture Radar Images. IEEE Transaction on Geoscience and Remote Sensing, 51(5), pp.2587-2600.

Appendices

Appendix A: Explanation of the symbols in the oval form

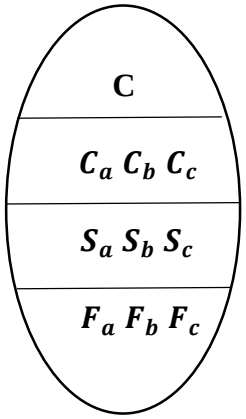

Fig A1: Definition of the symbols in the oval shape

Concentration (C)

C – On the top, we have the total concentration of sea ice in tenths

$\boldsymbol{C_a\ C_b\ C_c}$ **–** Partial concentration of thickest ($\boldsymbol{C_a}$) ice, partial concentration of second thickest ($\boldsymbol{C_b}$) ice and partial concentration of third thickest ($\boldsymbol{C_c}$) ice.

Stage of development (S)

$\boldsymbol{S_a\ S_b\ S_c}$ **–** Stage of development of thickest ($\boldsymbol{S_a}$) ice, Stage of development of second thickest ($\boldsymbol{S_b}$) ice and Stage of development of third thickest ($\boldsymbol{S_c}$) ice.

Form of ice (F)

$\boldsymbol{F_a\ F_b\ F_c}$ **-** Size of ice floe corresponding to $S_a\ S_b\ S_c$ respectively

Concentration	Symbol
Ice free	
Less than one tenth	0
1/10	1
2/10	2
3/10	3
4/10	4
5/10	5
6/10	6
7/10	7
8/10	8
9/10	9
More than 9/10	9+
10/10	10

Table A1: Total concentration of sea ice

Element	Floe size	Symbol
Pancake ice	-	0
Brash ice	<2 m	1
Ice cake	2 – 20 m	2
Small floe	20 – 100 m	3
Medium floe	100 -500 m	4
Big floe	500 m – 2 km	5
Vast floe	2 – 10 km	6
Giant floe	>10 km	7
Fast ice	-	8
Icebergs	-	9

Table A2: Form of sea ice

Element	Thickness	Symbol
No stage of development	-	0
New ice	-	1
Nilas	<10 cm	2
Young ice	10 – 30 cm	3
Grey ice	10 -15 cm	4
Grey-white ice	15 – 30 cm	5
First year ice	30 – 200 cm	6
Thin-first year ice	30 – 70 cm	7
Thin-first year ice, first stage	30 – 50 cm	8
Thin-first year ice, second stage	50 – 70 cm	9
Medium first-year ice	70 -120 cm	1·
Thick first-year ice	>120 cm	4·
Old ice	>200 cm	7·
Second-year ice	>200 cm	8
Multi-year ice	>200 cm	9·

Table A3: Stage of development

Appendix B: SVM and texture analysis code

```
import os
import numpy as np
from osgeo import gdal, gdal_array, gdalconst
from osgeo import ogr
import pandas as pd
import image_slicer

from sklearn.decomposition import PCA

from sklearn.svm import SVC
from sklearn.preprocessing import MinMaxScaler
from sklearn.model_selection import train_test_split
from sklearn.metrics import confusion_matrix
from sklearn.metrics import classification_report
from sklearn.metrics import accuracy_score
from sklearn.model_selection import cross_val_score,
StratifiedKFold, StratifiedShuffleSplit
from sklearn.model_selection import validation_curve,
GridSearchCV
from sklearn import preprocessing
from sklearn.feature_selection import SelectKBest
from sklearn.feature_selection import chi2
from sklearn.feature_selection import RFE
from sklearn.pipeline import Pipeline

from mlxtend.plotting import plot_decision_regions
from matplotlib.pylab import *
import matplotlib.patches as mpatches

from multiprocessing import Pool
from functools import partial
import time


#load the data for texture analysis and SVM classification
train_data_path =
'/home/io/ASTROSAT/SVM_seaIce_types/2016_05/TRAINING_data_thesis
'
sea_ice =
'/home/io/ASTROSAT/SVM_seaIce_types/2016_05/S1A_EW_polar_stereog
raphic201605_Ice_masked.tif'
glcm =
'/home/io/ASTROSAT/SVM_seaIce_types/subset_of_subset_calibration
_201605_Polar_stereographic_ALL_glcm.tif'

#Perform texture analysis using GLCM method
def haralick_features(img, win, d):
```

```
    win_sz = 2*win + 1
    window_shape = (win_sz, win_sz)
    arr = np.pad(img, win, mode='reflect')
    windows = util.view_as_windows(arr, window_shape)
    Nd = len(d)
    feats = np.zeros(shape=windows.shape[:2] + (Nd, 4, 13),
dtype=np.float64)
    for m in xrange(windows.shape[0]):
        for n in xrange(windows.shape[1]):
            for i, di in enumerate(d):
                w = windows[m, n, :, :]
                feats[m, n, i, :, :] = mht.haralick(w,
distance=di)
    return feats.reshape(feats.shape[:2] + (-1,))



#Choose the best features for SVM
test = SelectKBest(chi2, k=8)
fit_test = test.fit(X_train_minmax, y_train)
feats = fit_test.transform(X_train_minmax)

#print the scores
this_scores = cross_val_score(svm, X_test_minmax, y_test,
n_jobs=1)
scores = fit_test.scores_ #the features with the highest values
are the most important
print (scores)

values = [1,2,3,4,5,6,7,8,9,10,11,12,13,14,15,16,17,18,19]
features =
['Contrast_HH','Dissimilarity_HH','Homogeneity_HH','ASM_HH','Ene
rgy_HH','MAX_HH','Entropy_HH','Mean_HH','Variance_HH','Correlati
on_HH',

'Contrast_HV','Dissimilarity_HV','Homogeneity_HV','ASM_HV','Ener
gy_HV','MAX_HV','Entropy_HV','Mean_HV','Variance_HV','Correlatio
n_HV']

#plot the features
fig = plt.figure()
ax = fig.add_subplot(111)
plt.title(' Score of GLCM features', fontsize=13,
fontweight='bold')
ax.bar(values, scores, align = 'center')
ax.set_xticks(values)
ax.set_xticklabels(features, rotation='vertical', fontsize=10)
ax.set_xlabel('GLCM features', fontweight='bold')
ax.set_ylabel('Score of GLCM features', fontweight='bold')
```

```
plt.show()



#The two functions below rasterize the training datasets
def create_mask_from_vector(vector_data_path, cols, rows,
geo_transform,
                            projection, target_value=1):
    """Rasterize the given vector (wrapper for
gdal.RasterizeLayer)."""
    data_source = gdal.OpenEx(vector_data_path, gdal.OF_VECTOR)
    layer = data_source.GetLayer(0)
    driver = gdal.GetDriverByName('MEM')
    target_ds = driver.Create('', cols, rows, 1,
gdal.GDT_UInt16)# create new layer to save our results
    target_ds.SetGeoTransform(geo_transform)# set the
geoinformations for each vector layer
    target_ds.SetProjection(projection)# set the projection
    gdal.RasterizeLayer(target_ds, [1], layer,
burn_values=[target_value])# resterize each vector file
    return target_ds


def vectors_to_raster(file_paths, rows, cols, geo_transform,
projection):
    """Rasterize all vectors in a single image."""
    labeled_pixels = np.zeros((rows, cols))
    for i, path in enumerate(file_paths):
        label = i+1
        # rasterize all the vector file by calling the function
created above
        ds = create_mask_from_vector(path, cols, rows,
geo_transform,
                                     projection,
target_value=label)
        band = ds.GetRasterBand(1)
        labeled_pixels += band.ReadAsArray()
        ds = None
    return labeled_pixels

raster_dataset = gdal.Open(sea_ice, gdal.GA_ReadOnly)
geo_transform = raster_dataset.GetGeoTransform()
proj = raster_dataset.GetProjectionRef()
bands_data = []
for b in range(1, raster_dataset.RasterCount+1):
    band = raster_dataset.GetRasterBand(b)
    bands_data.append(band.ReadAsArray())
```

```
bands_data = np.dstack(bands_data)
row, col, n_bands = bands_data.shape

#Go to the folder where the training data are located and list
them all
files = [f for f in os.listdir(train_data_path) if
f.endswith('.shp')]
classes = [f.split('.')[0] for f in files]
shapefile = [os.path.join(train_data_path, f)
             for f in files if f.endswith('.shp')]

#Convert training data into raster format
labeled_pixels = vectors_to_raster(shapefile, row, col,
geo_transform,
                                   proj)

is_train = np.nonzero(labeled_pixels)#returns the non-zero
values
training_labels = labeled_pixels[is_train]#class labels
training_samples = bands_data[is_train]#pixels to be used for
training


# Tell GDAL to throw Python exceptions, and register all drivers
gdal.UseExceptions()
gdal.AllRegister()

img = bands_data #Image we want to classify
roi = labeled_pixels #training data
roi_int = roi.astype(int32)

#Read the PCA file
PCA = gdal.Open(pca, gdal.GA_ReadOnly)
bands_num = PCA.RasterCount
PCA_arr = PCA.ReadAsArray()
PCA_band3 = PCA_arr[0,:,:]

#read intensity values of SAR data
img_sigma = img[:,:,2:]
stack = [img_sigma, PCA_band3]
pca_img = np.dstack(stack)

pca_img[np.isnan(pca_img)]=999 #replace NaN values


roi = labeled_pixels #training data
roi_int = roi.astype(int32)

# check how many samples we have
```

```
n_samples = (roi>0).sum()
print('There are {n} samples'.format(n=n_samples))

labels = np.unique(roi_int[roi_int>0])
print('The training data include {n} classes:
{classes}'.format(n=labels.size, classes=labels))

Xx = pca_img[roi_int > 0] #X is the matrix containing our
features
yy = roi[roi>0]#y contains the values of our training data
print('The X matrix size is: {sz}'.format(sz=Xx.shape))
print('The y array size is: {sz}'.format(sz=yy.shape))
```

#Perform classification using multiprocessing to speed up the process

```
split_test_data = 0.30
X_train, X_test, y_train, y_test = train_test_split(Xx, yy,
test_size=split_test_data, stratify = yy)

#use pipeline to do all the steps automatically
pip = Pipeline([('scale', preprocessing.StandardScaler()),
                ('svm', SVC(kernel='rbf', C=10, gamma=0.065,
decision_function_shape='ovo', class_weight='balanced'))])
pip.fit(X_train, y_train)


def predict(input_data):
    img_predict = pip.predict(input_data)
    return img_predict


start = time.time()

tfs_shape = (pca_img.shape[0] * pca_img.shape[1],
pca_img.shape[2])
tfs_2D = pca_img.reshape(tfs_shape)

# split good data into chunks for parallel processing
tfsChunks = np.copy(tfs_2D)
split = np.array_split(tfsChunks, 4)

# run parallel processing of all data with SVM
pool = Pool(4)
svmLablesGood = pool.map(predict, split)

# join results back from the queue and insert into full matrix
```

```
svmLabelsGood = np.hstack(svmLablesGood)

# reshape labels from vector into 2D raster map
svm_reshape = svmLabelsGood.reshape(img.shape[0], img.shape[1])
plt.imshow(svm_reshape)
plt.show()


end = time.time()
print 'the processing time is:', end - start, '\n'


# Compute classification report and confusion matrix
target_names = ['class %s' % s for s in classes]
verification_pixels = vectors_to_raster(shapefile, row, col,
geo_transform,
                                    proj)

for_verification = np.nonzero(verification_pixels)
verification_labels = verification_pixels[for_verification]
predicted_labels = svm_reshape[for_verification]


print ('confusion matrix: \n %s' %
        confusion_matrix(verification_labels,
predicted_labels)), '\n'

print ('classification report: \n %s' %
        classification_report(verification_labels,
predicted_labels, target_names=target_names))
```

#Grid search analysis for finding the appropriate parameters for SVM

```
start = time.time()

X_copy = img[roi_int > 0] #X is the matrix containing our
features
X_float = X_copy.astype('float')
X_2bands = X_float[:,[2,3]]#plot decision boundary accepts array
with <=2 bands only. So, we keep 2nd,3rd bands from the array
y_int = y.astype(int)# y(our labels) should be integer to be
used in 'plot_desicon_boundary'

split_test1 = 0.30
X_train, X_test, y_train, y_test = train_test_split(X_2bands,
y_int, test_size=split_test1)
clf = SVC(kernel='rbf')
```

```
Cs = [1, 5, 10, 20, 50, 100]
Gammas = [1e-2, 1e-4]

clf = GridSearchCV(clf,
            dict(C=Cs,
                 gamma=Gammas),
                 cv=2,
                 pre_dispatch='1*n_jobs',
                 n_jobs=4)

clf.fit(X_train, y_train)

scores = [x[1] for x in clf.grid_scores_]
scores = np.array(scores).reshape(len(Cs), len(Gammas))

for ind, i in enumerate(Cs):
    plt.plot(Gammas, scores[ind], label='C: ' + str(i))


plt.legend()
plt.grid()
plt.xscale('linear')
plt.xlabel('Gamma')
plt.ylabel('Mean score')
plt.savefig('parameters_selection201602.tif')
plt.show()

end = time.time()
print 'the processing time is:', end - start
```